

10-1-2009

Development of Three Dimensional Fluid-Structure Interaction Models for the Design of Surface Acoustic Wave Devices: Application to Biosensing and Microfluidic Actuation

Reetu Singh
University of South Florida

Follow this and additional works at: <https://digitalcommons.usf.edu/etd>



Part of the [American Studies Commons](#)

Scholar Commons Citation

Singh, Reetu, "Development of Three Dimensional Fluid-Structure Interaction Models for the Design of Surface Acoustic Wave Devices: Application to Biosensing and Microfluidic Actuation" (2009). *USF Tampa Graduate Theses and Dissertations*.
<https://digitalcommons.usf.edu/etd/3677>

This Dissertation is brought to you for free and open access by the USF Graduate Theses and Dissertations at Digital Commons @ University of South Florida. It has been accepted for inclusion in USF Tampa Graduate Theses and Dissertations by an authorized administrator of Digital Commons @ University of South Florida. For more information, please contact digitalcommons@usf.edu.

Development of Three Dimensional Fluid-Structure Interaction Models for the Design of
Surface Acoustic Wave Devices: Application to Biosensing and Microfluidic Actuation

by

Reetu Singh

A dissertation submitted in partial fulfillment
of the requirements for the degree of
Doctor of Philosophy
Department of Chemical and Biomedical Engineering
College of Engineering
University of South Florida

Major Professor: Venkat R. Bhethanabotla, Ph.D.
John T. Wolan, Ph.D.
Vinay K. Gupta, Ph.D.
Patricia Kruk, Ph.D.
Rajan Sen, Ph.D.

Date of Approval:
October 1, 2009

Keywords: Acoustic Streaming, Device Design, Biofouling Elimination, Focused SAW,
Orthogonal SAW, Micro-Cavities

© Copyright 2009, Reetu Singh

Note to the reader

The original of this document contains color that is necessary for understanding the data. The original dissertation is on file with the USF library in Tampa, FL.

Dedication

Dedicated to my husband Subramanian K.R.S. Sankaranarayanan and my parents for their selfless love, support, and understanding when it was most needed.

Acknowledgments

I would like to take this valuable opportunity to sincerely thank and express my gratitude towards my advisor, Prof. Venkat R. Bhethanabotla, for his mentoring, advice, and support during my doctoral research at the University of South Florida. This dissertation would not have been possible without the kind support, advice, and constant encouragement of my advisor Prof. Venkat R. Bhethanabotla and my committee members: Drs. John T. Wolan, Vinay K. Gupta, Patricia Kruk, and Rajan Sen. I would like to express my thankfulness to my labmates Stefan Cular for stimulating discussions and his help, Sanchari Chowdhury and Pabitra Choudhury for their willingness to help whenever the need arose. I would like to acknowledge Academic Computing and Engineering Computing, at USF, for providing the computational support during the course of my studies at USF. I thank the National Science Foundation for providing the necessary financial support towards conducting the research presented in this dissertation (NSF grants CHE-0722887, ECCS-0801929, and IIP-07122360). Finally, I would like to express heartfelt gratitude and indebtedness towards my husband, Subramanian K.R.S. Sankaranarayanan, whose understanding nature, patience, support, and constant encouragement have gone a long way in making this dissertation possible.

Table of Contents

List of Tables.....	vi
List of Figures	vii
Abstract	xii
Chapter 1 Introduction	1
1.1 Motivation and Objectives	1
1.2 Choice of Substrate Material for SAW Biosensor for the Current Work.....	5
1.3 Organization of the Dissertation.....	6
Chapter 2 Acoustic Wave and Surface Acoustic Wave Devices: Applications to Biosensing and Microfluidics.....	9
2.1 Acoustic Wave Sensors	9
2.2 Acoustic Wave Propagation in Piezoelectric Substrates	12
2.3 Surface Acoustic Wave and Shear Horizontal Surface Acoustic Wave Devices.....	12
2.4 SAW Devices in Biosensing Applications.....	14
2.5 Acoustic Streaming in SAW Devices.....	15
2.6 Current Issues in SAW Biosensing	17
2.7 Computational Modeling of Fluid-Device Interaction	19
2.8 Finite Element Method.....	21
2.9 Current Work - Development of Three Dimensional Fluid-Structure Interaction Models to Design SAW Devices for Biosensing and Microfluidic Applications	22

Chapter 3	A Novel Three Dimensional Fluid-Structure Interaction Finite Element Model of Wave Propagation in SAW Device: Application to Biosensing & Microfluidics	23
3.1	Introduction	24
3.2	Computational and Model Details.....	27
3.2.1	Solid/Piezoelectric Domain.....	27
3.2.2	Fluid Domain	29
3.2.3	Fluid-Solid Interaction	29
3.2.4	Acoustic Streaming	31
3.2.5	Finite Element Model.....	32
3.3	Results and Discussion.....	34
3.3.1	Device Displacement and Fluid Velocities	34
3.3.2	Acoustic Streaming and Non-Specific Protein Removal	39
3.4	Conclusion.....	43
Chapter 4	Orthogonal Surface Acoustic Wave Device based on Langasite for Simultaneous Biosensing and Bio-fouling Removal.....	44
4.1	Introduction	44
4.2	Computational and Model Details.....	46
4.2.1	Fluid Domain	46
4.2.2	Piezoelectric Domain	46
4.2.3	Fluid-Solid Interaction	48
4.2.4	Finite Element Model.....	49
4.3	Results and Discussion.....	51
4.3.1	Frequency Response.....	51

4.3.2 AC Analysis: Wave Propagation Characteristics and Device Sensitivity.....	52
4.3.3 Acoustic Streaming Velocity	55
4.3.4 Adhesive And Removal Forces.....	58
4.4 Conclusion.....	60
Chapter 5 Enhanced SAW Biosensor Performance <i>via</i> Integrated Transducer and Delay Path Modifications: A Computational Study.....	61
5.1 Introduction	61
5.2 Computational Details.....	64
5.2.1 Structural Model.....	64
5.2.2 Fluid Structure Interaction Model	65
5.2.3 Best Case Micro-Cavities.....	66
5.3 Results and Discussion.....	66
5.3.1 Best Case Micro-Cavities.....	66
5.3.2 Device Displacements and Transmission Losses.....	67
5.3.3 Fluid Streaming and Biofouling Elimination	72
5.3.4 Device Sensitivity	77
5.4 Conclusion.....	79
Chapter 6 Enhancement of Acoustic Streaming Induced Flow on a Focused SAW Device: Implications for Biosensing and Micro-fluidics	80
6.1 Introduction	81
6.2 Computational Details.....	84
6.2.1 Theory	84
6.2.2 Model Details.....	87

6.3	Results and Discussion.....	90
6.3.1	SAW Fluid Interaction.....	91
6.3.2	Fluid Flow Fields and Substrate Displacement Profiles	93
6.3.3	Acoustic Streaming Velocity and Force	98
6.3.4	Non-Specifically Bound Protein Removal (Focussed vs. Conventional SAW).....	103
6.4	Conclusion.....	110
Chapter 7	Design of Mutually Interacting Multi-Directional Transducer Configurations on a Surface Acoustic Wave Device for Enhanced Biosensing.....	112
7.1	Introduction.....	113
7.2	Computational and Model Details.....	115
7.2.1	Fluid Domain	115
7.2.2	Piezoelectric Domain	115
7.2.3	Fluid-Solid Interaction	117
7.2.4	Finite Element Model.....	118
7.3	Results and Discussion.....	120
7.3.1	Device Displacements and Device Sensitivity.....	120
7.3.2	Fluid Velocities and Streaming Forces	125
7.4	Conclusion.....	130
Chapter 8	Conclusions and Future Work.....	131
8.1	Contributions.....	132
8.2	Future Work	136
8.2.1	Newtonian vs. Non-Newtonian Fluid Loading	137
8.2.2	SAW Induced Ultrasonic Mixing and Micropumping	138

8.2.3 Droplet Generation.....	139
8.2.4 Multilayered SAW devices Based on Nanocrystalline Diamond.....	140
List of References.....	142
About the Author.....	End Page

List of Tables

Table 3.1:	Density (ρ , kg/m ³), Elastic Stiffness Constants (C_{ij} , GPa), and Piezoelectric Constants (e_{ij} , C/m ²) for LiNbO ₃	34
Table 4.1:	Density (ρ , kg/m ³), Elastic Stiffness Constants (C_{ij} , GPa), and Piezoelectric Constants (e_{ij} , C/m ²) for Langasite	50
Table 4.2:	Comparison of Non-Specific Adhesive and Removal Forces for Particles on a 70 MHz SAW Device Based on Langasite for Propagation Along the Off-Axis (0, 22, 0) Direction.	59
Table 4.3:	Calculations of Removal Force for Different Number of IDT Pairs and Comparison With Non-Specific Adhesive Force	60
Table 6.1:	Summary of Various F-SAW Designs Simulated	91
Table 6.2:	Comparison of Adhesive and Removal Forces Corresponding to Three Different Particle Sizes for Focused SAW (F-SAW) vs. Conventional SAW (C-SAW) Devices.....	105

List of Figures

Figure 1.1: Examples of Different Transducer Configurations	3
Figure 1.2: Device Surface Modifications in the Delay Path for Improving SAW Device Performance	3
Figure 2.1: A Schematic Showing Acoustic Wave Devices	11
Figure 2.2: A Surface Acoustic Wave Biosensor Functionalized Using an Antibody Linked to the Device <i>via</i> a Coupling Agent (eg. Organosilane), Showing a Specifically Bound Antigen.	15
Figure 2.3: Schematic Showing Acoustic Streaming Induced by a Surface Acoustic Wave Device.	17
Figure 3.1: Meshed Structure of a Surface Acoustic Wave Device.....	33
Figure 3.2: Displacement Contours on the Piezoelectric Device Surface at Various Time Instants	35
Figure 3.3: Instantaneous Fluid Velocity Profiles at Various Time Instants	37
Figure 3.4: Fluid Velocity Contours on a Section Cut Through the Center of the Delay Path Along the Propagation Length at 70 ns.....	39
Figure 3.5: Time Averaged Acoustic Streaming Velocity Profiles	41

Figure 4.1: Schematic Diagram of an Orthogonal Surface Acoustic Wave Device simulated in the Current Work	49
Figure 4.2: Meshed Fluid-Structure Interaction Model of the SAW Device With Fluid Loading.	51
Figure 4.3: Calculated Frequency Response Along (0, 22, 0) and (0, 22, 90) Euler Directions in the Simulated Orthogonal SAW Device.....	52
Figure 4.4: Contour Plot Showing Shear Horizontal Wave Propagation Along the (0, 22, 90) Direction on Langasite Substrate.....	53
Figure 4.5: Contour Plot Showing Mixed Mode Wave Propagation Along the (0, 22, 0) Direction on Langasite Substrate.....	54
Figure 4.6: Comparison of Sensitivities for the Langasite Substrate for Propagation Along the (0, 22, 90) Euler Direction and a Comparable 36° YX-LiTaO ₃ Substrate.....	55
Figure 4.7: Simulated Fluid Velocity Vector Profile for a Peak Input AC Voltage of 2.5V Applied to the Langasite SAW Device Operating at 68 Mhz.	57
Figure 4.8: Streaming Velocity Profiles Along the Fluid Film Thickness Computed by Time Averaging, for a Peak Input AC Voltage of 2.5V Applied to the Langasite SAW Device Operating at 68 Mhz.	57
Figure 5.1: Schematic Diagram of a Mutually Interacting Orthogonal IDT Device With Micro-Cavities Etched Along the Delay-Path of the SAW Device.....	64

Figure 5.2: Comparison of Transmitted Energies for Empty and PS-Filled Micro-Cavities Having $\lambda/2$ Square Cross Section and Depths of $\lambda/4$, $\lambda/4$ and $\lambda/2$ With Standard LGS SAW Delay-Line Device and an Optimized LW Device.....	67
Figure 5.3: Snapshots of Displacement Contours Taken at Various Time Instants Showing Surface Acoustic Wave Propagation in the LGS Orthogonal SAW Device With Micro-Cavities ($\lambda/2 \times \lambda/2 \times \lambda/2$) in the Delay Path.	68
Figure 5.4: Comparison of Transmitted Energies for Different Device Configurations.	71
Figure 5.5: Comparison of Streaming Forces.	73
Figure 5.6: Instantaneous Fluid Velocity Contours at Various Time Instants in the Orthogonal SAW Device Having Micro-Cavities ($\lambda/2 \times \lambda/2 \times \lambda/2$) Etched in the Delay Path	74
Figure 5.7: Fluid Velocity Vector for Orthogonal SAW Device With Micro-Cavities in Delay Path.	76
Figure 5.8: Comparison of Time Averaged Streaming Velocity Profiles in the Three Principal Directions Across the Fluid Film Thickness	77
Figure 5.9: Comparison of Mass Sensitivities.	78
Figure 6.1: (a) Meshed Fluid-Structure Interaction Model of the Surface Acoustic Wave Device in Contact With the Fluid Domain. (b) Schematic Showing Focused Interdigital Transducers in a Focused SAW Device.	87
Figure 6.2: Meshed Structures of the Simulated SAW Devices With IDTs.....	89

Figure 6.3: AC Voltage for Structure Excitation Applied to Input IDTs.....	90
Figure 6.4: (a) Simulated Fluid Displacement Profile for the Conventional SAW Device (b) Simulated Fluid Displacement on a Section Cut Through the Device Center Across the Fluid Film Thickness Along the Propagation Length in the Conventional Saw Device.....	92
Figure 6.5: Simulated Fluid Velocity Vectors for the Conventional and Focused SAW Device.....	94
Figure 6.6: Simulated Piezoelectric Device Displacement Contours	96
Figure 6.7: Comparison of Particle Displacement on the Device Surface Along the Propagation Length for Focused SAW (F-SAW) vs. Conventional SAW (C-SAW) Device Having Uniform IDTs for a Peak Input AC Voltage of 2.5 V.....	97
Figure 6.8: Simulated Fluid Velocity Profiles.....	98
Figure 6.9: Comparison of Streaming Forces (FSAW) for Focused SAW (F-SAW) vs. Conventional SAW (C-SAW) Device Having Uniform IDTs Corresponding to a Peak Applied Input AC voltage of 2.5 V	99
Figure 6.10: Comparison of Variation in Fluid Streaming Velocity Along the Fluid Film Thickness in Focused SAW vs. Conventional SAW Device for a Peak Input AC Voltage of 2.5 V	101
Figure 6.11: Illustration of the Interplay of Various Adhesive and Removal Forces on the Non-Specific Proteins Bound to the SAW Surface.	106

Figure 6.12: Comparison of Radius of the Smallest Particle (R_{min}) That Can Be Removed, in a Conventional SAW (C-SAW) vs. Focused SAW (F-SAW) device.....	109
Figure 7.1: Meshed Model Showing Mutually Interacting Inter-Digital Transducers Along Different Euler Directions.....	119
Figure 7.2: Displacement Contours at Various Time Instants on the Surface of the SAW Device With Mutually Interacting Orthogonally Oriented Uniform and Focused IDTs.....	121
Figure 7.3: Biosensor Sensitivity on a Langasite Substrate Calculated Along the (0, 22, 90) Direction.	124
Figure 7.4: Velocity Profiles of the Fluid in Contact With the Surface of the SAW Device at Various Time Instants	126
Figure 7.5: Streaming Forces on a Langasite Substrate Calculated Along the (0, 22, 0) Direction.	129

Development of Three Dimensional Fluid-Structure Interaction Models for the Design of
Surface Acoustic Wave Devices: Application to Biosensing and Microfluidic Actuation

Reetu Singh

ABSTRACT

Surface acoustic wave (SAW) devices find uses in a plethora of applications including but not limited to chemical, biological sensing, and microfluidic actuation. The primary aim of this dissertation is to develop a SAW biosensor, capable of simultaneous detection of target biomarkers in fluid media at concentrations of picogram/ml to nanogram/ml levels and removal of non-specific proteins from sensor surface using the process of acoustic streaming, for potential chemical sensing, medical, and clinical diagnostic applications. The focus is on the development of three dimensional finite element structural and fluid-structure interaction models to study wave propagation and acoustic actuation of fluids in a SAW biosensor. This work represents a significant improvement in understanding fluid flow over SAW devices, over the currently available continuum model of Nyborg. The developed methodology includes use of a novel substrate, namely, Langasite coupled with various combinations of novel multidirectional interdigital transducer (IDT) configurations such as orthogonal, focused IDTs as well as sensor surface modifications, such as micro-cavities. The current approach exploits the capability of the anisotropic piezoelectric crystal to launch waves of different characteristics in different directions, which can be put to the multiple uses including but not limited to sensing *via* shear horizontal waves and biofouling elimination *via* Rayleigh wave induced acoustic streaming.

Orthogonal IDTs gives rise to constructive interference, thereby enhancing the magnitudes of device displacements and fluid velocities. The net effect is an increase in device sensitivity and acoustic streaming intensity. The use of micro-cavities in the delay path provides a synergistic effect, thereby further enhancing the device sensitivity and streaming intensity. Focused IDTs are found to enhance the device displacements and fluid velocities, while focusing the device displacements and fluid motion at the device focal point, thereby enhancing the SAW device biosensing performance. The work presented in this dissertation has widespread and immediate use for enhancing sensor sensitivity and analyte discrimination capabilities as well as biofouling removal in medical diagnostic applications of SAW sensors. This work also has a broad relevance to the sensing of multiple biomarkers in medical applications as well as other technologies utilizing these devices such as microfluidic actuation.

Chapter 1

Introduction

1.1 Motivation and Objectives

Acoustic wave (AW) devices are based on piezoelectric crystals, which allow the transduction of electrical energy to acoustic energy and vice versa. Surface acoustic wave (SAW) devices are characterized by an acoustic wave whose propagation is restricted to the surface of the piezoelectric substrate and find use in a multitude of applications including but not limited to microfluidics, chemical, and biological sensing. In the current era, miniaturization and integration of multiple functionalities on a single SAW device will revolutionize the microelectronics industry, especially for their utility in various biological and chemical processes such as highly integrated lab-on-a-chip systems that combine multiple functions on a single chip. Microfluidics lies at the core of such technology, miniaturizing various processes on micrometer – nanometer length scale for various life sciences, biological, defense, and pharmaceutical applications, such as lab-on-a-chip systems. One of the approaches towards development of microfluidic technologies relies on SAW pumping units fabricated by patterning interdigital transducers (IDTs) on suitable substrates such as Lithium Niobate (LiNbO_3) and Lithium Tantalate (LiTaO_3) [1, 2]. Some applications of microfluidics include gene expression analysis using DNA chips, DNA hybridization, lab-on-chip systems, immuno-assays, micro-arrays, biosensing, drug screening, single cell handling and manipulation, drug delivery, ultrasonic mixing, actuation, flow cytometry, and microliter-picoliter droplet generation, colloidal patterning, and jet atomization to name a few [3-13].

The current work focuses on the incorporation of multiple functionalities on a single SAW device for biosensing and microfluidic actuation applications. The use of the SAW devices in biosensing applications relies on the ability of these devices to produce an output signal in response to an input quantity, through the process of transduction. Further, biosensing requires the transduction of picogram to nanogram level of biomarkers, present in small volumes of biological fluids, into a readable signal without interference from other proteins thereby necessitating high device sensitivity, selectivity, capability of manipulating small fluid volumes, and minimizing dead volumes. Advances in the device fabrication techniques and the integration of multiple functionalities on a single SAW device can result in improved device performance, such as enhanced sensitivity, selectivity and speed of response as well as actuation capabilities.

The key issues related to biosensor technology include: (1) biofouling resulting from the binding of undesirable moieties such as non-specific proteins to the sensor surface (2) selectivity (3) sensitivity (4) response and recovery times (5) detection limit (6) cost and (7) size. The most severe limitation of current biosensors technology is the inability to obtain a repeatable, fast, selective response to a target analyte at low concentrations. Modifications in device delay path, novel transducer configurations and proper choice of piezoelectric material and orientation hold the promise of addressing these issues. The current research aims at addressing the above issues by employing novel SAW device designs involving transducer and device surface modifications, such as those shown in Figs. 1.1 and 1.2, in light of the advances being made in microelectronic fabrication techniques, such as nano-imprint lithography. Development of a device that is capable of simultaneously detecting the desired biomarkers at levels of tens of picograms to nanogram/ml while achieving the removal of other non-specifically bound proteins to avoid interference with the sensing phenomenon is the main focus of this research.

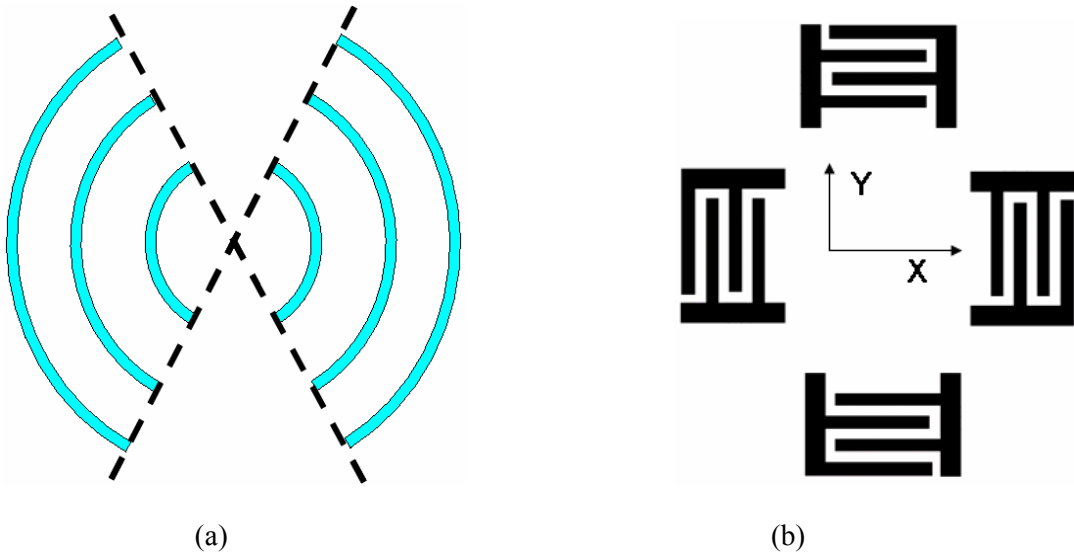


Figure 1.1: Examples of Different Transducer Configurations (a) Focused IDTs (b) Orthogonal IDTs

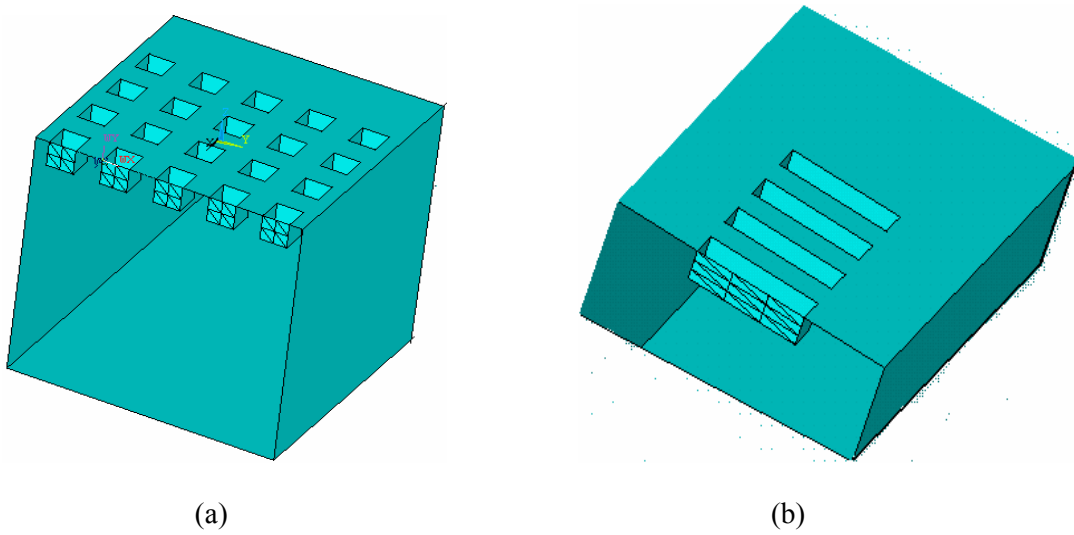


Figure 1.2: Device Surface Modifications in the Delay Path for Improving SAW Device Performance (a) Micro-cavities (b) Grooves

Computational methods such as finite element (FE) are an efficient tool to study the influence of various IDT configurations and surface modifications on the wave propagation, fluid

flow and velocity fields in SAW devices [14, 15]. The fluid device coupling leads to transfer of energy from the piezoelectric device to the fluid medium, which when exploited efficiently, can be used for microfluidic manipulations. In biosensing applications, this interaction can be exploited to achieve the removal of non-specifically bound (NSB) proteins from sensor surface to allow sensor reuse while minimizing the effect of this fluid-device interaction on biosensing and the adhesion of specific proteins to the device surface. Understanding the interaction of the fluid field with the SAW sensor and the effects of various IDT configurations (such as multidirectional IDTs) on wave propagation in the crystal requires the development of coupled field structural and fluid-structural (FSI) FE models which provide an alternative to experiments and can provide more detailed information about the nature of propagating waves, flow field, and the interaction of propagating waves with the liquid media.

The present work focuses on the development of three dimensional finite element structural and fluid-structure interaction models of SAW devices to investigate the wave propagation characteristics and interaction with the fluid media. In particular, the emphasis is on the development of coupled field structural and FSI models to study the effect of wave propagation characteristics on sensor response in multi-frequency SAW device. Using the framework of the developed FE structural and FSI models, the IDT configurations and surface modifications that allow for enhanced device performance, are identified. Specifically, this research aims at designing SAW sensors interacting with a liquid loading with improved selectivity, sensitivity and speed of response for enhanced biosensing and actuation. This work is based on the approach that piezoelectric crystal anisotropy allows for the propagation of fundamentally different modes of acoustic waves of different frequencies in different directions. The current research has manifold aims, which include (1) Identifying a piezoelectric substrate, for use in SAW device, that can be used in biosensing applications and can achieve the dual objective of biosensing and non-specific biofouling protein elimination (2) investigation of

acoustic wave propagation characteristics along various cut and propagation direction for the SAW device (3) identifying multidirectional IDT designs capable of launching different modes of acoustic waves in the same piezoelectric substrate in order to simultaneously achieve sensing and non-specific biofouling protein removal in the same device (4) delay path modifications to include micro-cavities and grooved structures for increased energy entrapment at the surface acoustic wave surface (5) understanding the fluid-SAW interaction which can be exploited to remove weakly and non-specifically bound proteins from device surface. The overall goal is to obtain a SAW device that would allow multiple functionalities of biosensing and NSB removal in the same device, although the results are generally applicable to various microfluidic actuation applications of SAW devices.

1.2 Choice of Substrate Material for SAW Biosensor for the Current Work

In this section, the choice of Langasite as a suitable substrate for use in a SAW biosensor in the current work, is justified. A Langasite ($\text{La}_3\text{Ga}_5\text{SiO}_{14}$) crystal is a trigonal piezoelectric material [16-18] similar to α -quartz. To achieve good SAW device characteristics, good temperature characteristics of group delay time and small temperature related characteristic variations are desired in the piezoelectric substrate. Langasite offers considerable advantages for use in SAW sensors, which include temperature coefficient of zero, low sensitivity to process parameters, low phase velocity, low diffraction [19], high dielectric permittivity [20] and low level of bulk excitation waves [19] which would lead to smaller insertion loss [21]. In addition, Langasite does not undergo phase transition upto 1400 deg C [22-24], making it suitable for high temperature treatment during the manufacturing process and for high temperature sensing applications [25-30]. In addition, Langasite has a stronger electromechanical coupling coefficient compared to α -quartz, which is desirable especially in applications where a Rayleigh wave is excited in the SAW device [22]. Therefore, Langasite is a promising material for biosensing

applications and hence the current work utilizes this material as the piezoelectric substrate for biosensing applications.

1.3 Organization of the Dissertation

This dissertation is organized as follows

Chapter 2 provides a brief introduction to sensors. The principles and uses of surface acoustic wave (SAW) and shear horizontal SAW (SH-SAW) sensors are discussed. This chapter also brings out the main issues related to biosensor technology and highlights the importance and need of computational finite element (FE) models as an alternative to experiments to model the fluid-device interaction. The advantages of the three dimensional computational FE fluid-structure interaction (FSI) models, over the available analytical and simpler computational models, are discussed.

Chapter 3 discusses the development of a fully coupled three dimensional transient FE FSI model of the SAW device subject to liquid loading to investigate the streaming velocity fields and forces induced by SAW device. The dynamics of the fluid domain in contact with the piezoelectric domain is investigated and discussed. The results broadly apply to microfluidic actuation applications of the SAW device.

Chapter 4 discusses the design and development of a novel SAW biosensor based on a Langasite (LGS) substrate for simultaneous biosensing and bio-fouling removal by employing multidirectional interdigital transducers (IDTs). The crystallographic directions, allowing the propagation of waves of fundamentally different characteristics, are identified. 3-D structural and FSI FE models, of LGS based SAW sensor, are developed. A multidirectional orthogonal transducer configuration is employed along two different crystallographic orientations in LGS substrate and the nature of propagating waves along both directions is obtained and investigated to analyze the suitability of the device for integrating the dual functionality of biosensing and

NSB protein elimination, on a single device. The fluid field and the various hydrodynamic forces are computed and analyzed. The applicability of the device for the dual functionality of simultaneous biosensing and biofouling elimination is investigated and discussed. The results have significance in understanding biosensing and microfluidic actuation mechanisms in the respective applications of the SAW devices.

Chapter 5 discusses integrated multi-directional IDTs and delay path modifications in SAW devices based on a LGS substrate. The simulated devices have mutually interacting orthogonal IDTs and micro-cavities of square cross-sections and different depths located in the middle of the delay path. 3-D structural and FSI FE models are developed for the devices with combined mutually interacting orthogonal IDTs and micro-cavities in the delay path; the fluid velocity profiles as well as the acoustic streaming force and device sensitivity are compared for the device designs. The effects arising from mutually interacting transducers and delay path modifications in the form of micro-cavities in SAW sensors on LGS are investigated. The improved SAW device design has tremendous significance and implications in the areas of biosensing and microfluidic applications.

Chapter 6 investigates and discusses the fluid motion induced in a focused surface acoustic wave (F-SAW) device with concentric inter-digital transducers (IDTs). 3-D bi-directionally coupled FSI FE models of a F-SAW device are developed and various features in the flow field and wave propagation characteristics are derived from the developed models. Acoustic streaming flow fields are investigated to evaluate the enhancement in the intensity of acoustic streaming brought about by the F-SAW device in comparison to a conventional SAW device. The results from the study detailed in this chapter are generally applicable and significant of microfluidic actuation applications of SAW devices.

Chapter 7 deals with the design of a Langasite based biosensor with a mutually interacting multidirectional IDT configuration, along different Euler directions for enhanced

biosensor performance. The main focus is to achieve the dual objective of biosensing and efficient biofouling removal via the combined use of uniform IDTs (U-IDTs) and focused IDTs (F-IDTs). U-IDTs are employed along the crystallographic orientation that allows for propagation of shear horizontal waves while F-IDTs are used along the direction that allows for the propagation of waves with surface normal component. Three dimensional (3D) coupled field FE models are developed to investigate the second order effects arising from these mutually interacting IDTs and biosensor performance is analyzed in terms of device sensitivity and acoustic streaming force which is a measure of the biofouling removal efficiency.

Chapter 8 discusses the major contributions of the current work and recommendations for future work that is possible using the framework provided in this dissertation, to advance the field of SAW microfluidics.

Chapter 2

Acoustic Wave and Surface Acoustic Wave Devices: Applications to Biosensing and Microfluidics

2.1 Acoustic Wave Sensors

A sensor is a device that produces an output signal in response to an input quantity, through the process of transduction. The input signal can be a physical, chemical, or biological quantity which may include properties of films, concentrations of analytes or biological species whereas the output signal is usually an oscillatory voltage or frequency, whose value can be related to the change in sensing layer properties. Acoustic wave (AW) devices, which were primarily used in the telecommunications industry as acoustic wave filters, have gained increasing importance as sensors in the recent years due to their small size, high reliability, cost effectiveness, and high sensitivity. In addition, these devices can be used in passive wireless mode [31-33], without the need of a power supply, which makes them excellent candidates for remote monitoring and for use in situations where use of conventional sensors can be hazardous, such as under strong radioactive exposure. The use of acoustic waves in sensing applications can be attributed to the discovery of a phenomenon known as piezoelectricity, which refers to the ability of certain materials to generate an electric potential in response to mechanical strain and vice versa. These materials, which are generally crystals, lack a center of inversion symmetry. Some of the most commonly used piezoelectric substrates include quartz, lithium niobate (LiNbO_3), lithium tantalite (LiTaO_3), Langasite (LGS), lead zirconium titanate (PZT), zinc oxide (ZnO), and silicon carbide (SiC) to name a few. Acoustic wave (AW) sensors exploit the

capability of piezoelectric materials to generate a mechanical strain in response to the application of an electric potential at the input interdigital transducers (IDTs), which in turn creates a mechanical wave that propagates through the piezoelectric medium. These devices can be classified into single port and two port devices. In single port devices such as quartz crystal microbalances, the same port serves as the input and output port; however the input and output ports are distinct and separate in two port devices which include surface acoustic wave (SAW), acoustic plate mode (APM), and flexural plate mode (FPW) devices. The acoustic mode interaction with the species being detected leads to changes in the characteristics of these propagating waves, which forms the basis of sensing in AW sensors. Typically, chemical sensitivity is imparted to an AW sensor by depositing a thin film in the acoustically active region, between the input and the output IDTs. In biological sensing applications, this film is typically coupled to antibodies which can bind the target biomolecules. The film acts as a chemical/biological to physical transducer whose properties change in response to the species being detected; the most common being change in the mass of the film due to the accumulation/deposition of the chemical species. However changes in other film characteristics like electrical or elastic properties can also be utilized. The change in the film properties induces a change in the propagated acoustic wave which can be detected at the output IDTs. AW sensors exploit the changes in acoustic wave propagation characteristics, such as amplitude and/or velocity, in piezoelectric media for detecting chemical and biological species of interest.

Based on the methods of signal transduction, a sensor can be broadly classified into thermal, mass, electrochemical, and optical. AW sensors belong to the class of mass sensors and detect changes in the mass loading of an analyte on the sensor surface by monitoring the propagation of acoustic waves in a piezoelectric substrate.

Based on the acoustic mode of operation, the acoustic wave sensors can be classified into [34]

- (1) Devices that generate shearing motion like the Thickness shear mode (TSM) resonator (also referred to as Quartz Crystal Microbalance or QCM)
- (2) Devices with predominantly surface displacement (eg. Surface Acoustic Wave (SAW) sensors based on Rayleigh waves and shear horizontal waves)
- (3) Devices using a shear horizontal acoustic plate mode (APM)
- (4) Devices utilizing waves propagating at velocity lower than that of sound (Flexural plate wave (FPW) devices)

Schematics of one port TSM and two port SAW devices are shown in Fig. 2.1 (a, b). In this chapter, surface acoustic wave devices based on Rayleigh and shear horizontal wave modes are discussed in detail.

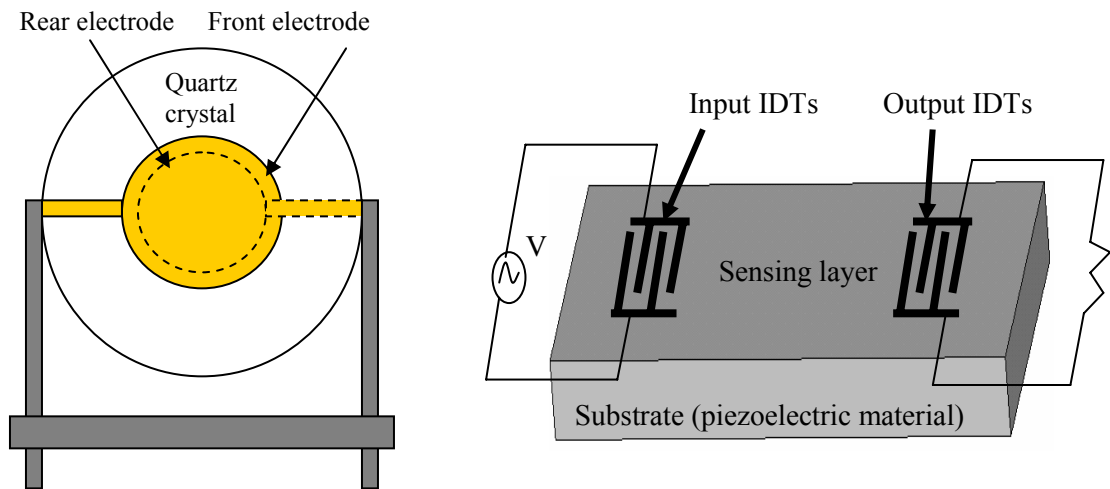


Figure 2.1: A Schematic Showing Acoustic Wave Devices (a) TSM (Quartz Crystal Microbalance) device (b) Surface acoustic wave device used for chemical and biological species detection. V denotes input voltage.

2.2 Acoustic Wave Propagation in Piezoelectric Substrates

Application of alternating voltage to the input IDTs results in the generation of mechanical strain in the piezoelectric crystals. Deformation of a solid leads to the displacement of the constituent particles from their original position, represented by $u(x, y, z, t)$, resulting in the propagation of a wave through the medium. The propagating waves can be compressional or shearing in nature. The local deformations of the medium are represented by the second order displacement gradient tensor, given by

$$\nabla u = \begin{bmatrix} \frac{\partial u_1}{\partial x} & \frac{\partial u_1}{\partial y} & \frac{\partial u_1}{\partial z} \\ \frac{\partial u_2}{\partial x} & \frac{\partial u_2}{\partial y} & \frac{\partial u_2}{\partial z} \\ \frac{\partial u_3}{\partial x} & \frac{\partial u_3}{\partial y} & \frac{\partial u_3}{\partial z} \end{bmatrix} \quad (2-1)$$

u_i ($i=1, 2, 3$) represents the displacements along the three principal directions. The displacement gradient represents the translations as well as local rotations caused by particle displacements. The results of rotations are ignored and the local stretching of the solid is obtained by adding the displacement gradient to its transpose, which gives the strain matrix S

$$S_{ij} = \frac{1}{2} \left(\frac{\partial u_i}{\partial x_j} + \frac{\partial u_j}{\partial x_i} \right) \quad (2-2)$$

The diagonal terms of the strain matrix represent compressional strains whereas the off diagonal terms are representative of shear strains.

2.3 Surface Acoustic Wave and Shear Horizontal Surface Acoustic Wave Devices

A surface acoustic wave (SAW) device consists of two sets of interdigital transducers (IDTs) patterned on a piezoelectric crystal, namely the input and the output IDTs. The application of an alternating voltage on the alternately connected input IDTs causes a mechanical deformation in the piezoelectric crystal, which in turn leads to the generation of a standing

acoustic wave. This wave launches propagating waves in both directions [34]. SAW sensors are characterized by an acoustic wave whose propagation is restricted to the surface due to the stress free boundary condition on the crystal surface, thereby making the wave highly sensitive to surface perturbations [35]. The output IDTs receive these acoustic waves and convert them back to an electric signal. A comparison of magnitudes and the phase difference between the input and output electrical signals constitutes the SAW sensor response. Figure 2.1(b) depicts a SAW sensor with a sensing layer in the delay line path.

In SAW devices, the acoustic wave propagation is confined near the surface, which allows for these waves to be generated by surface electrodes and possess extreme sensitivity to surface perturbations. To satisfy the stress free boundary condition of the crystal, the surface traction forces are zero, i.e.

$$T \cdot \hat{z} = 0 \quad (2-3)$$

T denotes stress tensor, \hat{z} denotes unit normal to the surface.

In an isotropic medium or along a pure mode direction in the crystal, the propagating acoustic wave reduces to a Rayleigh wave whose transverse component is negligible [36, 37]. The surface normal and longitudinal components being 90° out of phase, the particles move in an elliptical orbit in the sagittal plane. The wave amplitude along the surface normal direction decay rapidly away from the surface, with most of the wave energy confined within one wavelength of the surface. As the frequency of the device increases, the wavelength decreases, thereby confining the wave energy closer to the device surface and increasing the sensitivity of the device to surface perturbations. Owing to the presence of prominent surface normal wave component, compressional waves are generated in liquid medium, when it is in contact with the SAW device. This leads to significant dissipation of the wave energy and SAW attenuation, thereby rendering the SAW mode unsuitable for sensing in liquid media [38-40]. The Rayleigh wave SAW mode is, however, suited for gas phase sensing applications.

Shear horizontal surface acoustic wave (SH-SAW) devices are characterized by surface particle displacements having components parallel to the device surface (longitudinal direction) as well as normal to the propagation [41] direction (transverse direction) but a negligible surface normal component. The absence of the surface normal component allows the shear horizontal (SH) wave to propagate without any coupling with the liquid domain in contact with the device. This prevents energy dissipation and wave attenuation, thus making the SH-SAW device very well suited for liquid sensing [42-45] such as biosensing in bodily fluids.

2.4 SAW Devices in Biosensing Applications

SAW sensors find intensive applications in chemical and biological sensing owing to their portability, cost effectiveness, high sensitivity, and reliability [43, 46-53]. Biosensors find use in a wide array of applications including detection of pathogens, biological warfare agents, analysis of drug composition, biomarker detection for various pathologies such as cancer, glucose monitoring and other health related markers, sensing of micro organisms, determining biological activities of new compounds, detection of toxic compounds, food analysis, various security applications and many other biological assays. SAW biosensors use a biosensing element which interacts with the biological species being detected, leading to a surface perturbation in the device which is converted into a measurable signal which is collected at the output transducer. Typically, biosensing applications require the detection and measurement of biomarkers in fluid media [54]; an example being the measurement of certain proteins in bodily fluids for the detection of ovarian cancer. Thus, biosensors are often subject to liquid loading. The biosensing elements used in SAW biosensors refer to proteins, antibodies or nucleic acids which have an affinity for the target biological species to be detected [55-58]. Thus, a SAW biosensor surface requires functionalization with proteins and antibodies that can bind specifically to the target biomolecules (Fig. 2.2), at concentrations as low as a single molecule. The use of SAW sensors in biosensing

applications requires the detection of small quantities of biomarkers in small volumes of biological fluids thereby necessitating the integration of SAW devices with microfluidics [7, 59-63], which is the science of designing systems that can confine the processes to length scales typically in the micrometer range, such that the volumes of fluids handled are of the order of picoliters to nanoliters thereby reducing the dead volume in the system .

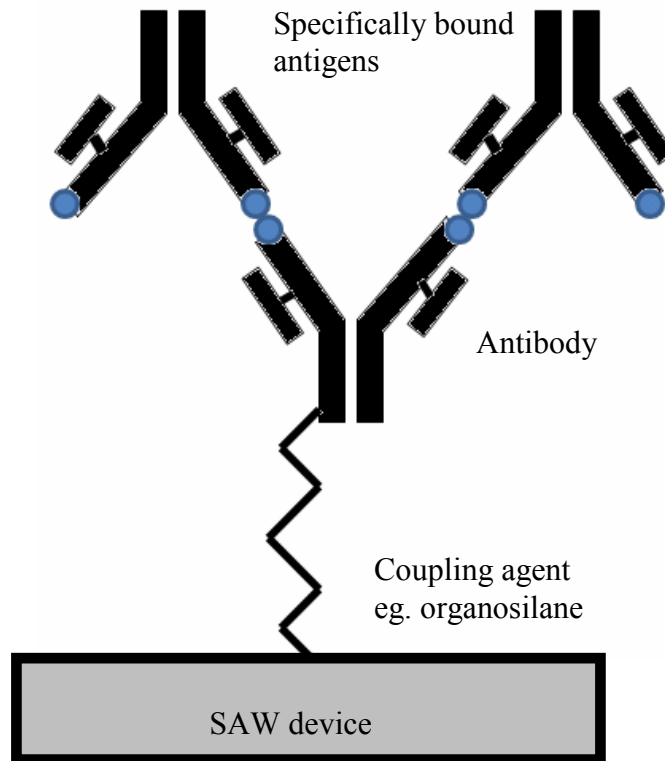


Figure 2.2: A Surface Acoustic Wave Biosensor Functionalized Using an Antibody Linked to the Device *via* a Coupling Agent (eg. Organosilane), Showing a Specifically Bound Antigen.

2.5 Acoustic Streaming in SAW Devices

Acoustic streaming, a phenomenon first discovered by Lord Rayleigh in 1884, results from the interaction of SAWs with liquid film covering a piezoelectric substrate and represents a challenging phenomenon that has led to several inventions over the last few years [64-68]. When

SAWs with a prominent surface normal component interact with fluid media in contact with the SAW device, they couple strongly with the fluid [69]. If the velocity of the acoustic wave in the fluid (v_f) is smaller than that on the device surface (v_R), energy transfer takes place from the SAWs to the fluid which launches compression waves in the fluid at a characteristic angle known as Rayleigh angle given by [70]

$$\theta = \sin^{-1}\left(\frac{v_L}{v_R}\right) \quad (2-4)$$

This strong fluid-device interaction leads to mode conversion from Rayleigh to leaky SAW which leaks energy into the fluid medium and undergoes attenuation leading to decay in the amplitude [71-73]. This leakage of energy to the fluid domain results in the transfer of momentum from the SAW to fluid domain, resulting in the propagation of longitudinal waves in the fluid domain (Fig. 2.3). This SAW-fluid interaction creates a pressure gradient in the direction of acoustic wave propagation in the fluid, inducing fluid flow and leading to an acoustically driven streaming phenomenon known as SAW streaming [74-76]. In microfluidic channels, boundary induced acoustic streaming becomes the dominant transport phenomenon owing the fact that the streaming propulsion forces and velocities are localized in the vicinity of the channel walls and the flow is primarily laminar at such small length scales.

A large number of applications can be envisaged for the acoustic streaming phenomenon, including pumping of fluids in microfluidic channels, fluid property measurement, droplet formation, liquid droplet propulsion, droplet positioning, enhanced reactant transport in applications like detection using surface Plasmon resonance which otherwise would be mass transport controlled, droplet detachment from free surfaces, ultrasonic mixing and microtransport in microfluidic channels, biosensing, droplet atomization, thin film deposition to name a few [8, 11, 77-85]. One of the most critical developments utilizing acoustic streaming is ‘lab on a chip’ devices which integrates multiple laboratory functionalities on a single micron sized device for use in diagnostic applications such as immunoassays. One such example is a microfluidic device

that integrates nanoliter droplet manipulation, propulsion, and mixing on a single piezoelectric substrate [80, 86-89]. In such a device, directed movements of the droplets allow them to merge, leading to reactant contact and subsequently reaction. At low SAW amplitudes, the acoustic micro streaming leads to internal mixing of the reactants, which in turn induces chemical and biochemical reactions in the droplet acting as a microreactor. At high SAW amplitudes, bulk streaming leads to the advective transport of the droplets. Such devices find use in biological applications such as DNA hybridization, to accelerate the mass transport limited reactions in such processes by enhancing the rate of transport *via* streaming induced advection.

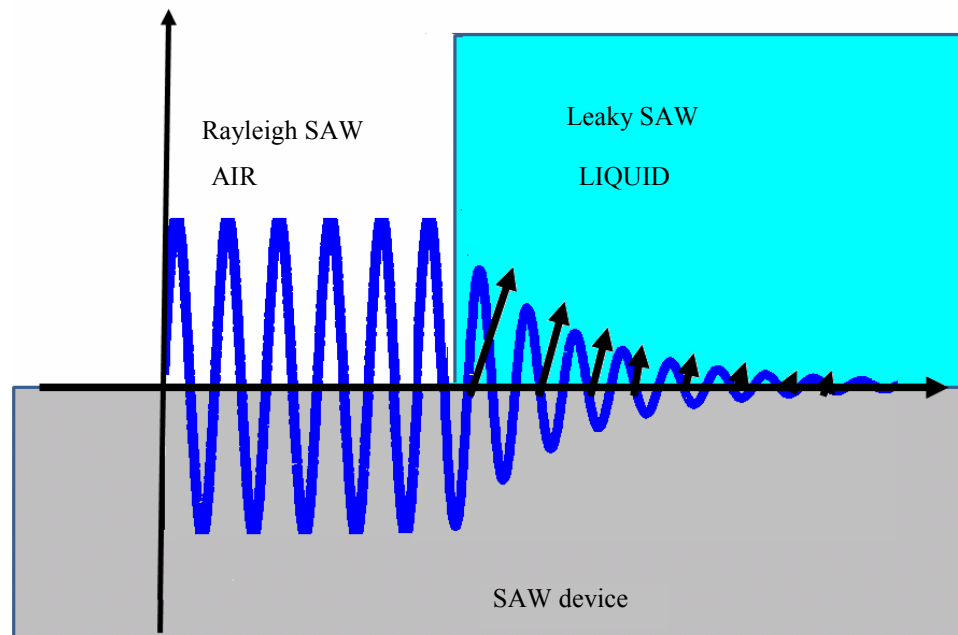


Figure 2.3: Schematic Showing Acoustic Streaming Induced by a Surface Acoustic Wave Device.

2.6 Current Issues in SAW Biosensing

Most of the clinical and medical diagnostic applications of SAW microfluidic devices require transduction of picogram to nanogram level of biomarkers into a readable signal without

interference from other proteins and biomarkers, thereby requiring high device sensitivity and selectivity. However, most of the biosensors are plagued with the issue of binding of non-specific fouling proteins to the device surface, which reduces the available surface area for binding of specific proteins, thereby preventing specific interactions between the target analytes and the functionalized sensor device surface. This phenomenon of non-specific protein binding, thus reduces device sensitivity, selectivity, as well as analyte discrimination capabilities [90]. As the sample volumes decrease, such as in biosensing applications where rare and expensive bodily fluids are used in very small volumes, non-specific protein binding becomes a critical issue affecting the repeatability and reproducibility of the data. Thus, simultaneous sensing and non-specifically bound (NSB) protein removal is desirable feature that remains a challenge in biosensing applications. There have been considerable efforts to devise methods that can potentially reduce the non-specific interactions, which include addition of detergents such as Tween 20 and non-reactive proteins such as albumin, gelatin or low fat milk [91-96]. Addition of detergents and nonreactive proteins reduces the background signal that results from the nonspecific protein adsorption resulting from hydrophobic interactions in the assays. However, these nonreactive proteins can potentially terminate the active surface groups and obscure target biomolecules by blocking them from binding to the desired sites. A potential technique, that forms the basis of the current work, is overcoming the nonspecific adhesive forces via microfluidic actuation of SAW devices. The current work explores the feasibility and role of the hemodynamic removal forces, induced by the fluid motion resulting from acoustic streaming in SAW devices, in overcoming the nonspecific adhesive forces while simultaneously allowing for biosensing.

Whereas the shear horizontal (SH) mode is suitable for sensing [97, 98], the removal of NSB fouling proteins is favored by Rayleigh waves which have a prominent surface normal component. Thus, different wave propagation modes are needed for the two purposes of sensing

and NSB removal. In addition, high device sensitivity is required so as to detect small enough concentrations of the analyte. The current work exploits the piezoelectric crystal anisotropy that allows for the propagation of fundamentally different modes of acoustic waves of different frequencies along different crystallographic orientations.

The choice of the piezoelectric substrate, piezoelectric crystal orientation, the IDT geometry/configuration, and crystal thickness determine the mode of the propagating waves. IDT designs and configurations must be identified which can allow the utilization of different waves for the purposes of sensing and cleaning. Recent experimental and computational studies have shown that the SAW induced acoustic streaming phenomenon can be used to knock off the NSB proteins from the device surface [99-101]. The efficient utilization of streaming in SAW devices requires the understanding of fluid dynamics in these systems. Further, owing to the fact that biosensors typically operate in a fluid media, understanding the acoustic wave propagation, fluid dynamics, and the sensing mechanism in SAW biosensors involving fluid interactions with complex multi-directional transducers and surface modifications represents a significant challenge.

2.7 Computational Modeling of Fluid-Device Interaction

Till date, attempts to model the fluid device interaction and investigate propagation of acoustic waves at the surface of a fluid-piezoelectric boundary have relied on simplified analytical models that solve the complex characteristic equation to obtain the complex leaky wave phase velocities and attenuation of the propagating waves [102-107]. Perturbation approaches, that treat the leaky wave as a first-order perturbation on the non-leaky wave associated with surface-wave propagation, have been developed [102, 103] to study fluid-device interaction and investigate the wave propagation characteristics. However, these analytical models are based on the assumption of simplified geometries, and ignore the effect of

fluid loading which is critical in determining the fluid dynamics, wave propagation characteristics, and affects the viscous drag forces that act on the fluid-structure boundary as a result of fluid motion induced by acoustic streaming. These factors necessitate the consideration and inclusion of fluid mechanical properties while modeling the interaction of the fluid domain with the SAW device.

Attempts to account fluid structure coupling while accounting for fluid mechanical properties have led to the development of FE unidirectionally coupled FSI models, that solve for the fluid domain with the solid domain motion applied as boundary conditions [107, 108]. Models involving fluid solid coupling while using acoustic elements for modeling the fluid region, have also been developed [109]. However, these models have a limitation as they involve the solution of the simplified Navier-Stokes equation for the pressure field in the fluid region while ignoring the viscous dissipation arising from the effects of fluid viscosity and are limited to investigations of wave damping.

The complex nature of the fluid-SAW interaction requires the solution of the generalized Navier-Stokes equation in conjunction with the acoustoelectric equations for solid motion, while establishing bidirectional coupling by maintaining stress and displacement continuity at the interface. Two dimensional (2-D) FE FSI models, developed previously [110] to model acoustic streaming in a SAW device based on YZ Lithium Niobate, are limited in scope. For example, 2-D FE FSI models cannot be used to model devices in which the wave propagation is mixed mode, with significant transverse and longitudinal components in addition to a surface normal component of wave displacement. Similarly, these models cannot be used to model devices with complex transducer geometries such as mutually interacting IDTs. This necessitates the development of a fully coupled three dimensional FSI model of a SAW device in contact with the fluid loading and forms the focus of the current work. The models are used to understand the complex device fluid interaction and the role of this interaction in determining the effectiveness

of acoustic streaming induced microfluidic actuation. Such a model is also instrumental in investigating the effectiveness of complex transducer geometries such as hexagonal IDTs in biofouling removal which require the inclusion of the transverse direction to provide a complete representation.

2.8 Finite Element Method

The basis of the finite element (FE) method is the discretization of the domain of interest (fluid and/or solid) into elements of characteristic length or mesh described as a product of shape functions that are functions of space and are independent of time [111]. The elements are connected by nodes. The FE representation of the fluid and structural domains involves a complex mathematical function of the node shape factors and the equation of the motion for the respective domains. The fluid and solid equations of motion are solved at the nodes to obtain the respective degrees of freedom for the two domains. For transient analysis, time integration techniques like forward Eulerian, backward Eulerian, or Newmark's methods are used to obtain a time-varying nodal solution. The structural models constitute solution of the piezoelectric equations while the FSI model involves the sequential solution of the piezoelectric and fluid domains and transfer of loads between the two domains until convergence is achieved.

The coupled finite element model for a piezoelectric substrate takes the form [112]

$$\begin{bmatrix} M & 0 \\ 0 & 0 \end{bmatrix} \begin{bmatrix} \ddot{\underline{u}} \\ \ddot{\underline{v}} \end{bmatrix} + \begin{bmatrix} C^s & 0 \\ 0 & C^d \end{bmatrix} \begin{bmatrix} \dot{\underline{u}} \\ \dot{\underline{v}} \end{bmatrix} + \begin{bmatrix} K^E & K^p \\ [K^p]^T & -K^d \end{bmatrix} \begin{bmatrix} \underline{u} \\ \underline{v} \end{bmatrix} = \begin{bmatrix} \underline{F} \\ \underline{L} \end{bmatrix} \quad (2-5)$$

M , C^s , and C^d are structural mass, structural damping, and element dielectric damping matrices, respectively. \underline{u} and \underline{v} are structural nodal displacement and nodal electric potential vectors, respectively. K^E , K^p , K^d are element stiffness, piezoelectric coupling, and element dielectric permittivity matrices, respectively. \underline{F} denotes nodal and surface force vector; \underline{L} denotes nodal, surface, and body charge vector.

2.9 Current Work - Development of Three Dimensional Fluid-Structure Interaction Models to Design SAW Devices for Biosensing and Microfluidic Applications

This dissertation is focused on the development of three dimensional structural as well as bidirectionally coupled FE FSI models of SAW devices in contact with fluid domain, to investigate the propagating wave characteristics, fluid dynamics and techniques to improve the streaming phenomenon thereby successfully eliminating weakly bound fouling proteins. Based on the fluid fields computed using the developed FE FSI models, the various forces that act on particles in the system, such as the non-specific and specific proteins, are computed to give an estimate of the various removal and adhesive forces on the particles. Such estimates are employed to establish design parameters for devices that can address elimination of biofouling NSB proteins while minimizing the influence on specifically bound proteins, thereby minimizing the effect on the sensing phenomenon and achieving the dual objective of biosensing and biofouling removal, simultaneously. Using the framework of the developed models, transducer and device surface modifications are designed to obtain biosensors that allow for simultaneous biosensing and biofouling elimination, while exhibiting high device sensitivity and biofouling elimination efficiency. Significant improvements in the sensor performance are expected from this new combination of transducer configurations and sensor surface modifications, as demonstrated in biosensing applications, within the scope of this dissertation. Although the results are discussed with reference to acoustic streaming applied to biofouling elimination and biosensing, the work presented herein broadly applies to various microfluidic and sensing applications of SAW devices and is expected to provide significant insights into microfluidic phenomenon in these devices.

Chapter 3

A Novel Three Dimensional Fluid-Structure Interaction Finite Element Model of Wave Propagation in SAW Device: Application to Biosensing & Microfluidics

The key issues related to biosensor technology include selectivity, sensitivity, response and recovery times, and detection limit; most of these limitations stem from biofouling resulting from the binding of undesirable moieties such as non-specific proteins to the sensor surface. Thus, removal of non-specifically bound (NSB) proteins remains a significant challenge in biosensing applications. Operation of biosensors in liquid media necessitates an investigation of the fluid-piezoelectric device interaction to understand the mechanisms of biofouling elimination as well as wave propagation in such devices. This chapter reports on the first three dimensional, fully coupled transient finite element fluid-solid interaction (FSI) model of the SAW device subject to liquid loading to investigate the streaming velocity fields and forces induced by SAW device. The simulation results suggest that the SAW-fluid interaction creates a pressure gradient in the direction of acoustic wave propagation in the fluid, leading to an acoustically driven streaming phenomenon known as SAW streaming which can be used for removal of non-specifically bound (NSB) proteins. Computed velocity fields indicate that the normal component of fluid velocity is smaller than the tangential component along the propagation direction. Thus, the SAW induced drag force, arising from the tangential component of fluid velocity and leading to particle advection is an important mechanism in biofouling removal from the SAW device surface and the normal component would prevent the reattachment of the particles to the device surface. Apart from microfluidic applications, this work broadly applies to all transducers used for biological

species sensing that suffer from fouling and non-specific binding of protein molecules to the device surface.

3.1 Introduction

The key issues related to biosensor technology include selectivity, sensitivity, response and recovery times, and detection limit; most of these limitations stem from biofouling resulting from the binding of undesirable moieties such as non-specific proteins to the sensor surface[99, 110]. Thus, removal of non-specifically bound (NSB) proteins remains a challenge in biosensing applications. When Rayleigh waves propagate in the piezoelectric device in contact with fluid, the transfer of momentum into the fluid domain leads to longitudinal wave propagation in the fluid domain, giving rise to an acoustically driven phenomenon known as acoustic streaming [113]. The SAW induced acoustic streaming has the potential to detach and remove the non-specifically bound (NSB) proteins from the device surface, as has been shown experimentally [99]. Computational methods can be used to investigate the acoustic streaming phenomenon in SAW devices.

Till date, attempts to model the fluid device interaction and investigate propagation of acoustic waves at the surface of a fluid-piezoelectric boundary have relied on simplified analytical models that solve the complex characteristic equation to obtain the complex leaky wave phase velocities and attenuation of the propagating waves [102-106, 114]. Perturbation approaches, which treat the leaky wave as a first-order perturbation on the non-leaky wave associated with surface-wave propagation, have been developed [102, 103] to model wave propagation and investigate wave propagation characteristics. However, these analytical models are based on simplifying assumptions and ignore the effect of fluid mechanical properties which poses a limitation since the fluid viscosity leads to viscous dissipation of energy, increases the leaky wave attenuation losses, and lower the phase velocities. Further, the fluid-SAW device

interaction leads to an acoustically drive streaming phenomenon that generates fluid motion at the interface boundaries. This fluid motion exerts viscous shear stresses on the interface boundary, which aid the detachment of loosely bound non-specific fouling proteins from the device surface. The effect of boundary layer thickness, which depends on the fluid viscosity, cannot be ruled out as well. Additionally, the simplified analytical models as discussed above do not take into account the influence of complex device geometries, such as the use of complex and mutually interacting IDTs. These factors necessitate the consideration and inclusion of fluid mechanical properties while modeling the interaction of the fluid domain with the SAW device. Computational methods such as finite element (FE) are an efficient tool to study the wave propagation, fluid flow and velocity fields in SAW devices.

In the past, FE models have been developed that solve for the fluid domain while the piezoelectric device motion, which is assumed to be an analytical function of a known time varying form, is superimposed as a boundary condition on the fluid-device interface [107, 115]. The grid positions and the velocity boundary conditions for the fluid are, thus, obtained from the analytical equation for solid motion. However, such models allow only for unidirectional coupling between the fluid and the device and the solid motion is not representative of the fluid dynamics in the system. To capture the dynamics of fluid-solid interaction, the fluid dynamical equations of motion must be solved in conjunction with the acoustoelectric equations describing the motion of the piezoelectric solid. FE models involving coupling of fluid and solid domains have been constructed using acoustic elements for modeling the fluid region. However, these models have a limitation as they involve the solution of the simplified Navier-Stokes equation for the pressure field in the fluid region while ignoring the viscous dissipation arising from the effects of fluid viscosity [109]. In addition, uniform mean density and mean pressures are assumed with the pressure solution in the model [109] being obtained as the deviation from the mean pressure instead of solving for the absolute pressure. Therefore, such studies can only

provide qualitative estimates of the fluid motion resulting from fluid-SAW interaction, and are limited to investigations of wave damping.

For SAW biosensing applications in liquid media, the complex nature of the fluid-device interaction requires one to model fluid motion which can be accomplished using fluid elements which allow for the solution of the generalized Navier-Stokes equation. Further, the understanding the interaction of the fluid field with the SAW sensor and the effects of various design parameters such as IDT configurations as well as device surface modifications on wave propagation in the crystal requires the development of coupled field structural and FSI FE models which would enable investigation of methods to increase the acoustic streaming velocity for NSB removal while minimizing the influence of the streaming force on the sensing layer, thereby increasing the sensitivity and selectivity. A two dimensional coupled field fluid structure interaction model has been developed [110] to investigate acoustic streaming in a SAW device based on YZ Lithium Niobate, in which fluid was modeled using Navier Stokes equation. Whereas such a model is appropriate for a pure Rayleigh wave such as in YZ Lithium Niobate, it does not provide a complete representation when the wave propagation is mixed mode having the surface normal, transverse, and longitudinal components. This necessitates the development of a fully coupled three dimensional FSI model of a SAW device in contact with the fluid domain. Such a model is also instrumental in investigating the effectiveness of complex transducer geometries such as orthogonal IDTs in biofouling removal which require the inclusion of the transverse direction to provide a complete representation. The current chapter focuses on the development of 3-D. fully and bidirectionally coupled FE FSI model of a piezoelectric device in contact with fluid domain. Although this model is developed for a YZ Lithium Niobate substrate in this chapter, the same model is extended to Langasite, which is the substrate of choice for biosensing applications in the current work.

3.2 Computational and Model Details

The FSI model involves sequential solution of the piezoelectric domain constitutive equations and Navier-Stokes equation in conjunction with the continuity equation with load transfer between the domains.

3.2.1 Solid/Piezoelectric Domain

The interaction between the electric field and mechanical strain is studied by coupling the elastic and electromagnetic constitutive equations through a piezoelectric matrix [34, 116-119].

$$\underline{T} = [c] \underline{S} - [e] \underline{E} \quad (3-1)$$

$$\underline{D} = [e]^T \underline{S} + [\varepsilon] \underline{E} \quad (3-2)$$

The resulting equations, known as the piezoelectric constitutive equations, describe the interaction between elastic strain, stress, and electric field in the piezoelectric substrate.

Here, \underline{T} and \underline{D} denote stress tensor and electric flux density vector, respectively. \underline{S} , \underline{E} denote structural strain and electric field intensity vectors, respectively. c , e , and ε represent structural elasticity matrix at constant electric field, piezoelectric stress matrix, and dielectric matrix at constant mechanical strain, respectively.

In the absence of body force, the equation of motion is given by

$$\nabla \cdot \underline{T} = \rho \ddot{\underline{u}} \quad (3-3)$$

where ρ is the density and \underline{u} represents displacement.

The electric field intensity is given by the gradient of the electric potential (φ)

$$\underline{E} = -\nabla \varphi \quad (3-4)$$

The strain tensor is symmetric, therefore

$$S_{ij} = \frac{1}{2} \left(\frac{\partial u_i}{\partial x_j} + \frac{\partial u_j}{\partial x_i} \right) \quad (3-5)$$

In tensor notation,

$$T_{ij} = \sum_{k,l=1}^3 c_{ijkl} \frac{\partial u_l}{\partial x_k} + \sum_{k=1}^3 e_{ijk} \frac{\partial \varphi}{\partial x_k} \quad (3-6)$$

In a system with no free charges,

$$\nabla \cdot D = 0 \quad (3-7)$$

Substituting and rearranging the above set of equations leads to a system of four coupled wave equations for the electric potential and the three component of displacement in piezoelectric materials which are solved for the piezoelectric substrate or the solid domain:

Combining Eqns (3-3) through (3-6), we get

$$\sum_{k,l=1}^3 c_{ijkl} \frac{\partial^2 u_l}{\partial x_j \partial x_k} + \sum_{k=1}^3 e_{ijk} \frac{\partial^2 \varphi}{\partial x_j \partial x_k} = \rho \frac{\partial^2 u_i}{\partial t^2} \quad (3-8)$$

Equation (3-8) represents three equations in four unknowns, namely the three displacements and the voltage (φ). The fourth equation is obtained by combining Eqns (3-2) and (3-7),

$$\sum_{j,k,l=1}^3 e_{jkl} \frac{\partial^2 u_l}{\partial x_j \partial x_k} - \sum_{j,k=1}^3 \varepsilon_{jk} \frac{\partial^2 \varphi}{\partial x_j \partial x_k} = 0 \quad (3-9)$$

Equations (3-8) and (3-9) form a complete set of coupled wave equations which can be solved for the four unknowns. These equations are discretized in space and time, and solved at the nodes in the finite element domain to obtain a transient solution.

The coupled finite element model for a piezoelectric substrate takes the form [112]

$$\begin{bmatrix} M & 0 \\ 0 & 0 \end{bmatrix} \begin{bmatrix} \ddot{\underline{u}} \\ \ddot{\underline{v}} \end{bmatrix} + \begin{bmatrix} C^s & 0 \\ 0 & C^d \end{bmatrix} \begin{bmatrix} \dot{\underline{u}} \\ \dot{\underline{v}} \end{bmatrix} + \begin{bmatrix} K^E & K^p \\ [K^p]^T & -K^d \end{bmatrix} \begin{bmatrix} \underline{u} \\ \underline{v} \end{bmatrix} = \begin{bmatrix} \underline{F} \\ \underline{L} \end{bmatrix} \quad (3-10)$$

M , C^s , and C^d are structural mass, structural damping, and element dielectric damping matrices, respectively. \underline{u} and \underline{v} are structural nodal displacement and nodal electric potential vectors, respectively. K^E , K^p , K^d are element stiffness, piezoelectric coupling, and element dielectric

permittivity matrices, respectively. \underline{F} denotes nodal and surface force vector; \underline{L} denotes nodal, surface, and body charge vector.

3.2.2 Fluid Domain

Fluid is modeled as an incompressible, viscous, Newtonian fluid using the Navier-Stokes and continuity equation in the Eulerian frame of reference. The generalized Navier-Stokes equation is written as

$$\rho \left(\frac{\partial v_f}{\partial t} + v_f \cdot \nabla v_f \right) + \nabla P - 2\eta \nabla \cdot D = 0 \quad (3-11)$$

The continuity equation takes the form

$$\frac{\partial \rho}{\partial t} + \nabla \cdot \rho v_f = 0 \quad (3-12)$$

Here, v_f , P , ρ and η denote the fluid velocity, pressure, density, and viscosity, respectively. D is the rate of deformation tensor given by

$$D = \frac{1}{2} \left(\nabla v_f + (\nabla v_f)^t \right) \quad (3-13)$$

3.2.3 Fluid-Solid Interaction

The solution of fluid and solid fields in the finite-element domain requires the use of either the Lagrangian or Eulerian frame of reference. The Eulerian frame refers to the fixed frame of reference whereas Lagrangian frame is a moving frame of reference. In the Lagrangian frame, the grid deforms as the region of interest deforms. Whereas the structural phase (piezoelectric substrate) is best described using the Lagrangian frame, either frame of reference can be used for the fluid domain. In the Lagrangian frame, the mesh embedded in the fluid domain moves with the velocity of the fluid while in the Eulerian frame, the mesh, through which the fluid moves, is

fixed. A purely Lagrangian frame is not suitable for dealing with strong distortions of the fluid mesh arising from the non-cohesive nature of fluid particles which causes them to travel independently and diverge in space. A purely Eulerian frame for the fluid domain introduces complexity in fluid-solid coupling as it is unable to track the path of the elements. Therefore, Arbitrary-Lagrangian-Eulerian (ALE) methods, which combine the best of the both frames of reference, are used for kinematical description of the fluid domain in such problems. In ALE, the Lagrangian frame is used for ‘almost contained’ flows and Eulerian description is used for regions where the mesh would be highly distorted if required to follow fluid motion. The theory for ALE has been developed by Hughes et al. for viscous, incompressible flows [120]. In the ALE framework, the fluid equation of motion can be written as [121]

$$\rho \left(\frac{\partial v_f}{\partial t} \right) + (v_f - w) \cdot \nabla v_f + \nabla P - 2\eta \nabla \cdot D = 0 \quad (3-14)$$

where w is the grid velocity such that $w \neq v_f \neq 0$.

To achieve fluid-solid coupling, an interface is defined across which displacements are transferred from solid to fluid and pressure from fluid to solid. These conditions translate to no-slip for the fluid domain (velocity continuity) and stress continuity for solid domain. The fluid mesh is continuously updated as the piezoelectric substrate undergoes deformation.

$$v_f = v_s = \frac{\partial u}{\partial t} \quad (3-15)$$

$$\sigma_{ij}^s n_j^s + \sigma_{ij}^f n_j^f = 0 \quad (3-16)$$

n_j is the outward normal at the solid-liquid interface in the deformed configuration, i denotes longitudinal direction. Superscripts f and s denote fluid and structural domain, respectively.

Fluid structure coupling is established by transferring displacements from solid to fluid and stress from fluid to solid across the fluid structure interface; this translates to displacement and stress continuity at the interface. The acoustic streaming velocity is obtained as the time

average of the first order fluid velocity v_f over a time period and contains contributions only from the time-invariant “dc” components.

3.2.4 Acoustic Streaming

The equations governing acoustic streaming are based the general Navier-Stoke’s equation for fluid flow and have been derived by Nyborg [122]. The generalized Navier Stoke’s equation is written as

$$\rho \left(\frac{\partial v_f}{\partial t} + v_f \cdot \nabla v_f \right) = -\nabla P + \nabla \cdot T + f_1 \quad (3-17)$$

Where ρ is the fluid density, f_1 denotes other body forces such as gravitational, v_f denotes acoustic streaming velocity, P is the pressure, and T is the deviatoric stress tensor.

The continuity equation takes the form

$$\frac{\partial \rho}{\partial t} + \nabla \cdot \rho v_f = 0 \quad (3-18)$$

Also,

$$\frac{\partial(\rho v_f)}{\partial t} = \rho \frac{\partial v_f}{\partial t} + v_f \frac{\partial \rho}{\partial t} \quad (3-19)$$

Combining Eqs (3-17) through (3-19),

$$\frac{\partial(\rho v_f)}{\partial t} + F = -\nabla P + \nabla \cdot T + f_1 \quad (3-20)$$

$$\text{Where } F = \left\langle \rho v_f \cdot \nabla v_f + v_f \nabla \cdot \rho v_f \right\rangle \quad (3-21)$$

F is the non linear driving force, which acts as the source for acoustic streaming and is related to the Reynold’s stresses. $\langle Q \rangle$ represents the time average of Q to obtain a time independent quantity [113, 123, 124]. The first order velocity, required to compute the SAW induced acoustic streaming force, is calculated using the particle displacement fields generated during the

propagation of a leaky SAW when the surface is in contact with a liquid [110, 124]. The force calculated using the first order velocity acts as a body force near the SAW-fluid interface. This force can be further used to compute the second order velocity, known as the acoustic streaming velocity induced by the SAW streaming force [125-127].

The velocity v calculated from Equations (3-11) through (3-16) contains harmonically varying terms and a “dc” term. The latter induces acoustic-streaming. When averaged over a relatively long time, the effect of the harmonically varying terms disappears and only the contributions from the dc part appear in the solution, producing a time invariant mean flow. The acoustic-streaming velocity ($\bar{v}_{a,i}; i = x, y, z$) is therefore obtained by averaging v over a time period as follows:

$$\bar{v}_{a,i} = \frac{1}{T} \int_0^T v_i dt \quad (3-22)$$

Where $i=x, y$ and z ; T is the time period of the wave propagation.

3.2.5 Finite Element Model

A coupled field FSI model of a YZ-LiNbO₃ based SAW device in contact with fluid loading, was developed (Fig. 3.1). The properties for the LiNbO₃ substrate are summarized in Table 3.1 [34]. Rotation of the matrices was carried out to obtain the stiffness and piezoelectric constants for the YZ-LiNbO₃ configuration. A substrate with dimensions 400 μm width x 800 μm propagation length x 200 μm depth in contact with a 50 μm thick fluid film was modeled. Two interdigital transducer (IDT) finger pairs in each port were defined at the surface. The fingers were defined with periodicity of 40 μm and aperture width of 200 μm. The IDT fingers were coupled by voltage degree of freedom. The model was meshed using twenty node coupled field solid elements with four degrees of freedom (DOF), three of them being the translations and the fourth being the voltage. The three dimensional coupled field solid element used to mesh the

piezoelectric is a 20 node element and exhibits large deflection, stress stiffening effects, and prestress effects. The governing equations for the piezoelectric domain were solved to obtain the displacements and voltage at each node. The fluid domain was meshed using an eight node fluid element. The fluid velocities were computed using the conservation of momentum principle and the pressure was computed using the conservation of mass principle. Millions of nodes and elements (2, 218, 399 nodes and 2, 085, 877 elements) were generated to ensure sufficiently high mesh densities. Further, the mesh was refined near the interface and coarser away from it, to capture the interfacial dynamics accurately. The fluid was modeled as incompressible and Newtonian, using the Navier-Stokes equation. The piezoelectric domain was discretized using the Lagrangian frame while arbitrary Lagrangian Eulerian (ALE) was used for the fluid domain. In the ALE description, the mesh is moved independent of the fluid particles, to track the motion of the boundary while minimizing the mesh distortion at the same time. The piezoelectric domain was excited using an ac voltage on the IDTs with a peak value of 2.5 V and frequency of 100 MHz, which is equal to the frequency of the device. The structure was simulated for 100 ns using a time step of 1 ns.

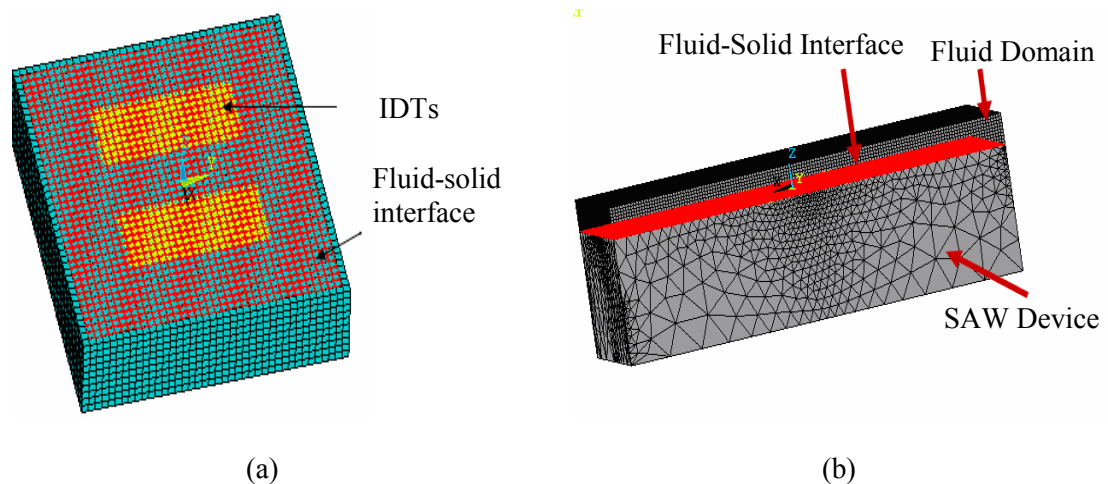


Figure 3.1: Meshed Structure of a Surface Acoustic Wave Device (a) Meshed structure with IDTs (b) Fluid loading.

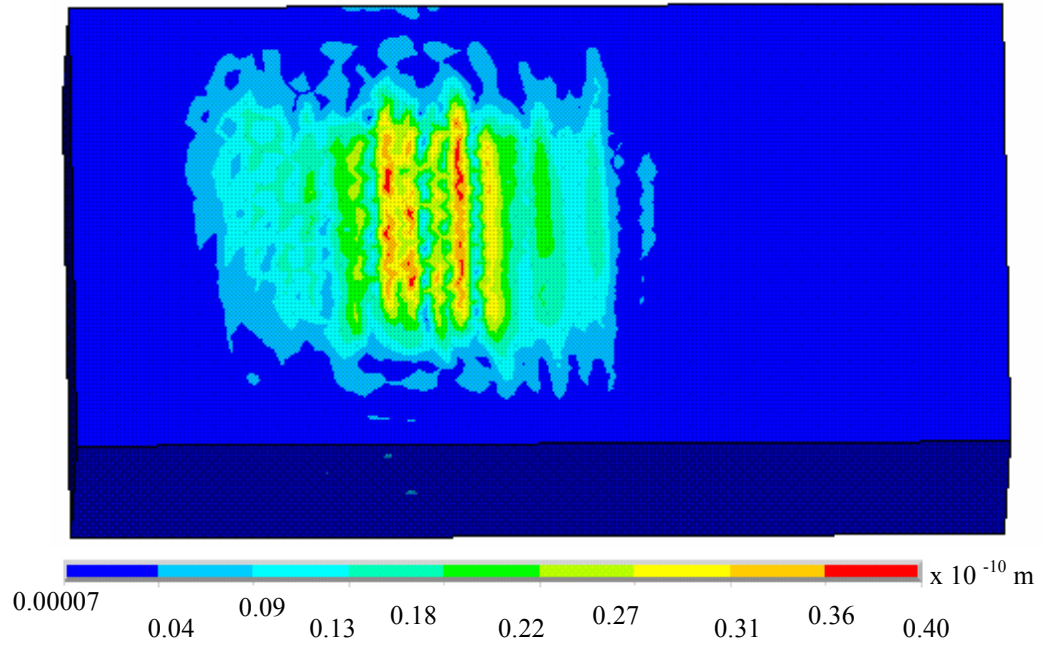
Table 3.1: Density (ρ , kg/m³), Elastic Stiffness Constants (C_{ij} , GPa), and Piezoelectric Constants (e_{ij} , C/m²) for LiNbO₃ [34]

Material constants	Value for LiNbO ₃
ρ	4700
C_{11}	20.3
C_{33}	24.5
C_{44}	6.0
C_{66}	6.0
C_{12}	5.3
C_{13}	7.5
C_{14}	0.9
e_{15}	3.7
e_{22}	2.5
e_{31}	0.2
e_{33}	1.3

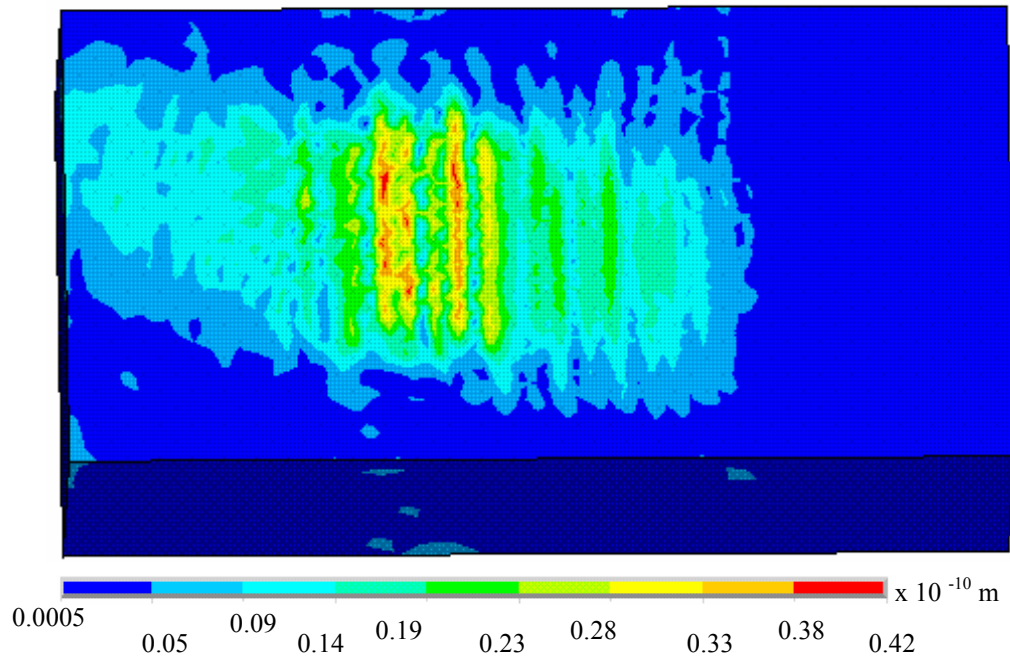
3.3 Results and Discussion

3.3.1 Device Displacement and Fluid Velocities

The piezoelectric device surface displacement profiles, shown at various time instants in Fig. 3.2, indicate that the highest displacement is occurs near the input IDTs and decays rapidly on moving away from them. The piezoelectric actuation by applying voltage to the input IDTs launches propagating waves in both directions, as evident from Fig. 3.2.



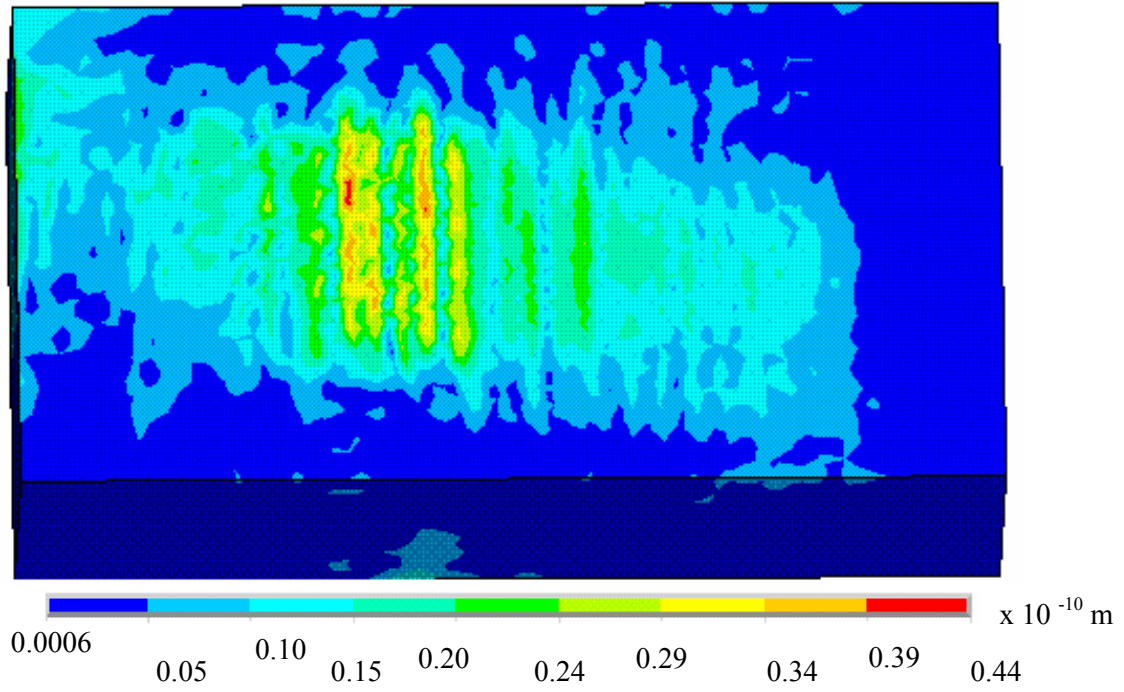
(a)



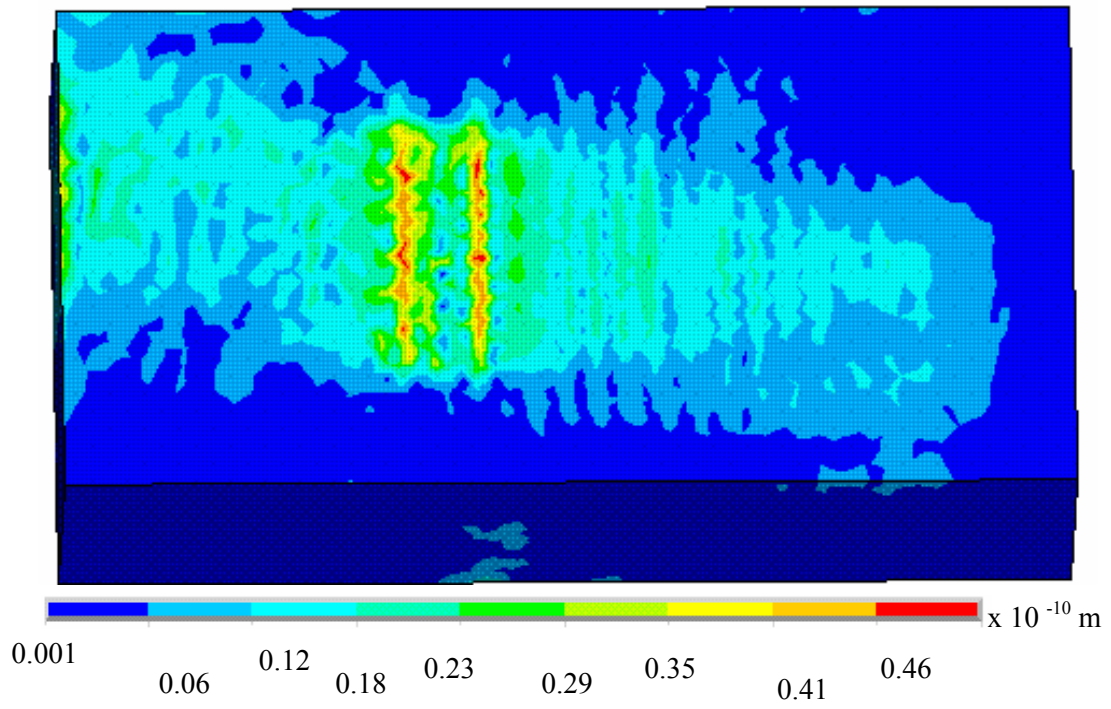
(b)

Figure 3.2: Displacement Contours on the Piezoelectric Device Surface at Various Time Instants

(a) 30 ns (b) 50 ns (c) 70 ns (d) 80 ns. Scale bar is in meters.



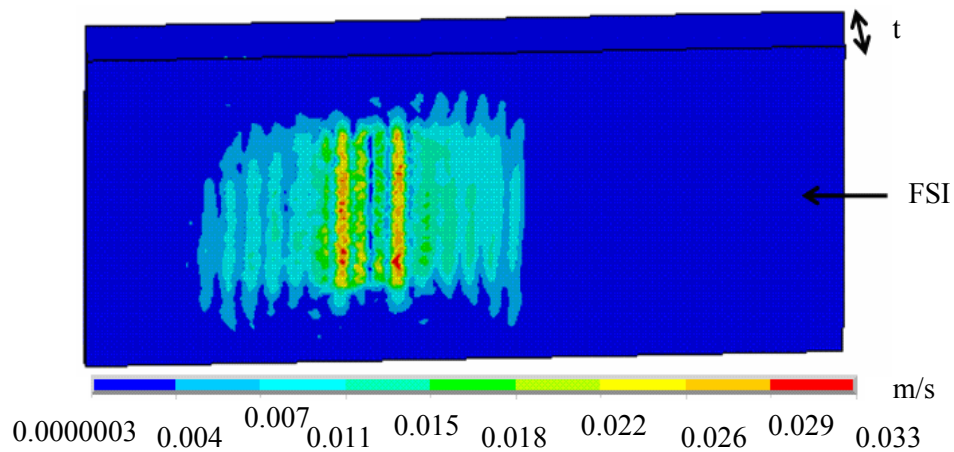
(c)



(d)

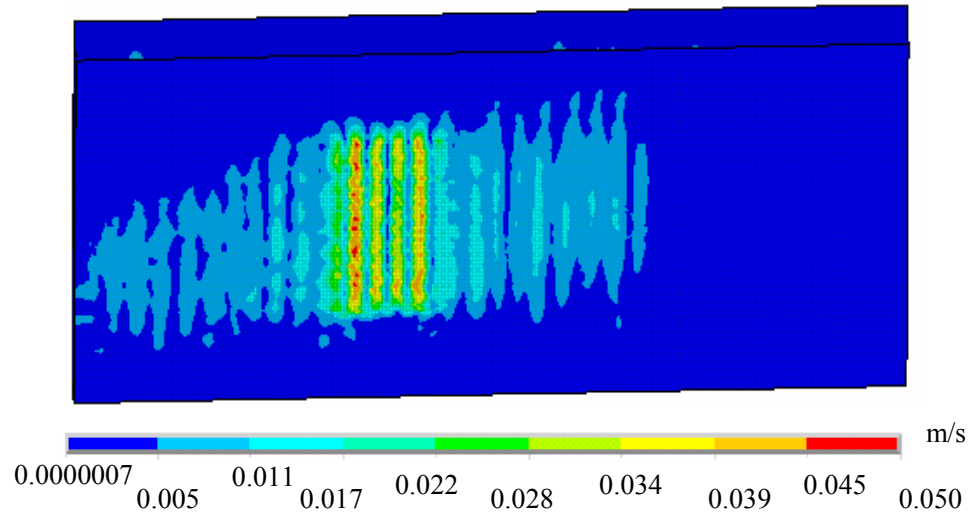
Figure 3.2: Continued.

Owing to coupling of the fluid with the piezoelectric substrate, the fluid motion also decays away from the input IDTs, leading to a conversion from Rayleigh to leaky SAW (Fig. 3.3), which in turn induces fluid motion. The conversion of attenuated sound waves into flow leads to an acoustically driven phenomenon, known as acoustic streaming. The fluid domain motion is shown in Fig. 3.3 which indicates that the fluid velocities obtained are of the order of mm/s, in accordance with the experimentally observed values [3]. The velocity contours obtained on a section through the center shows fluid recirculation away from the device surface (Fig. 3.4), suggesting the formation of eddies which can aid in particle removal by preventing their reattachment to the surface. Thus, the fluid couples strongly with the piezoelectric domain. An analysis of fluid velocity vector streamlines, which are indicative of particle trajectories, in the vicinity of the IDTs reveals recirculation leading to eddy formation between successive IDTs. Thus, one end of the IDTs acts as a source expelling the fluid and the other end acts as sink, where the fluid re-enters the IDT region. Thus, the IDTs induce fluid flow due to strong fluid-device coupling. This fluid motion decays away from the input IDTs.

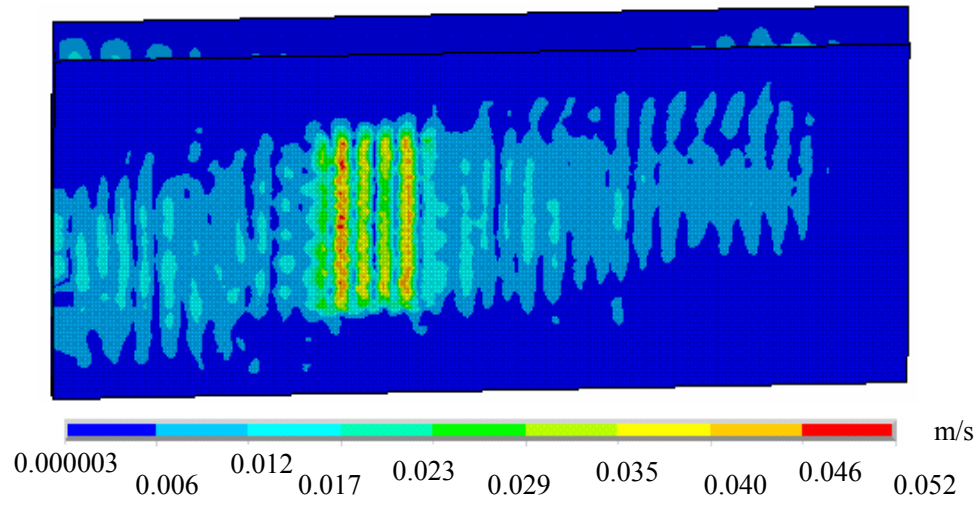


(a)

Figure 3.3: Instantaneous Fluid Velocity Profiles at Various Time Instants (a) 30 ns (b) 50 ns (c) 80 ns. Scale bar is in m/s.



(b)



(c)

Figure 3.3: Continued.

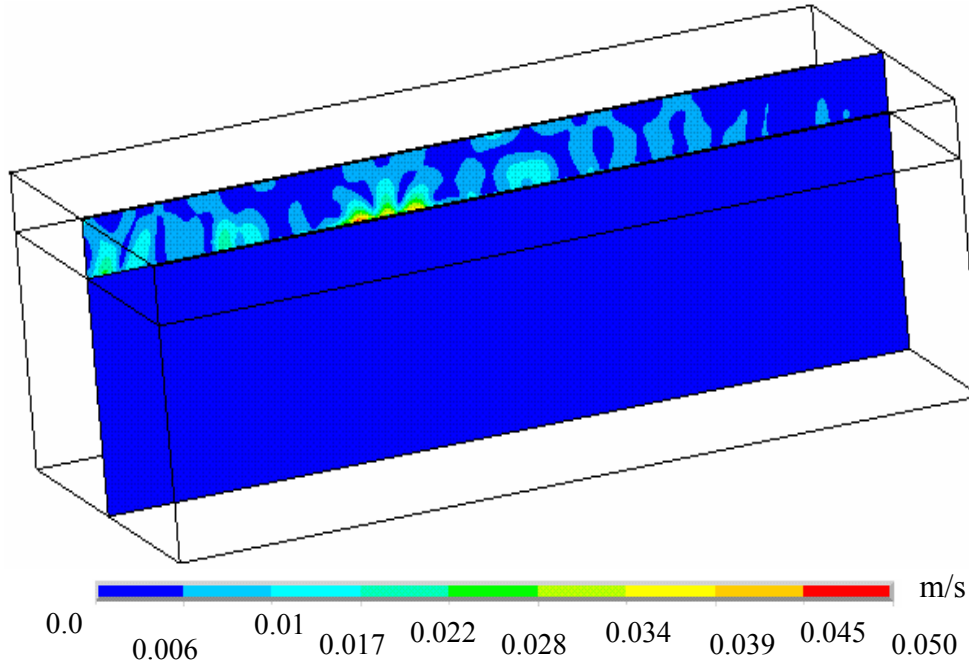


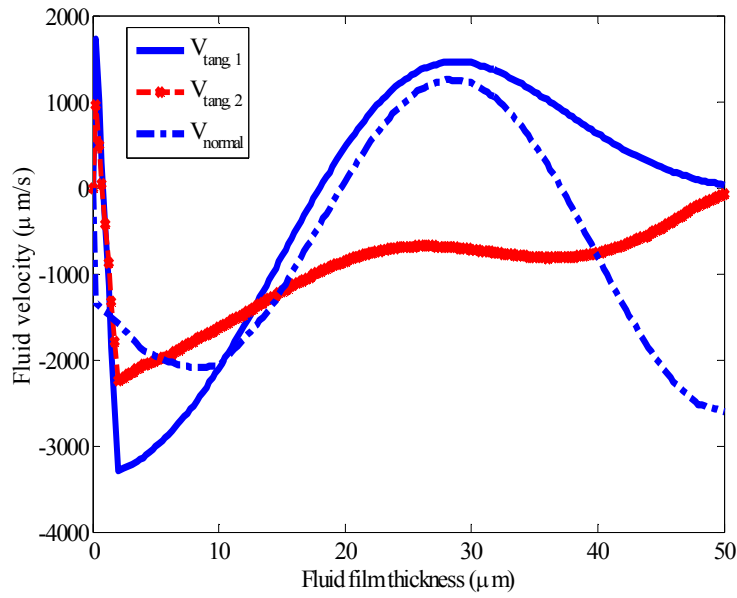
Figure 3.4: Fluid Velocity Contours on a Section Cut Through the Center of the Delay Path Along the Propagation Length at 70 ns. Scale bar is in m/s.

3.3.2 Acoustic Streaming and Non-Specific Protein Removal

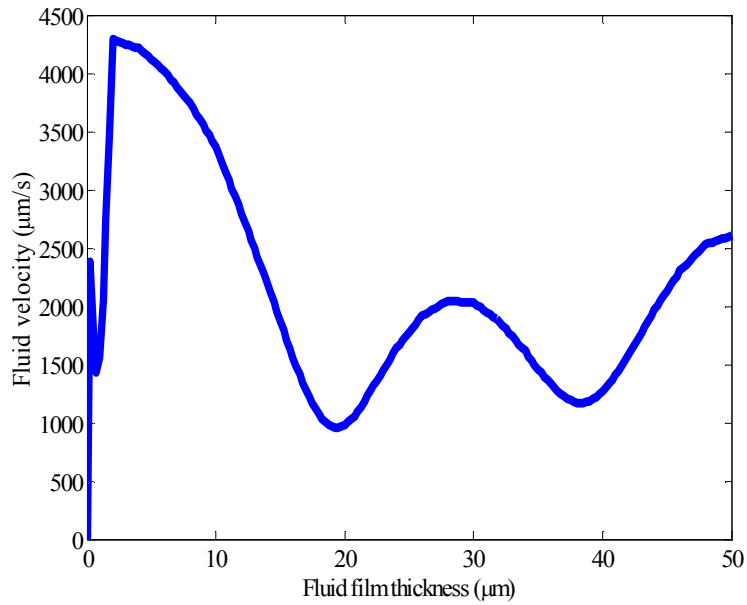
The transient solution obtained using the FSI model is used to compute acoustic streaming velocities [128]. The time averaged tangential, normal, and total streaming velocities are shown in Fig. 3.5. The profiles reveal that the normal velocity component although slightly smaller in magnitude than the tangential velocity components, is not negligible. This suggests strong coupling of the fluid with the piezoelectric domain, which eventually leads to a net pressure gradient in the fluid along the direction of wave propagation thereby causing fluid motion and giving rise to acoustic streaming. The maximum tangential and normal fluid velocities occur near the device surface. The velocity profiles indicate that most of the fluid motion is confined to the fluid thickness close to the device beyond which flow reversal takes place. This is indicative of fluid recirculation away from the surface, which can give rise to eddy formation. These eddies can

play a role in non-specific protein transport from the device surface. The tangential direction fluid velocities are higher than the normal velocities.

The removal of NSB proteins from the piezoelectric surface is the result of interplay between the removal and adhesive forces [129, 130]. The hydrodynamic forces on the NSB proteins resulting from fluid motion can lead to particle removal. The adhesive forces result from non-dispersive van der Waal's forces. The computations reveal that while the lift and drag forces are smaller compared to the adhesive van der Waal's forces, the direct SAW body force overcomes the adhesive force thereby detaching the particle from the device surface. As the detached particle moves away from the device surface, the SAW body force and adhesive van der Waal's force decrease rapidly. Therefore, following particle detachment, preventing their reattachment to the device surface is critical in ensuring their removal. At this stage, the forces exerted by the tangential and normal streaming velocity components play a role in overcoming the weight of the particle. Whereas the tangential direction velocities induce drag force leading to advection of NSB proteins, the normal velocities exert a lift force on the proteins which can prevent their reattachment to the surface. Thus, both these mechanisms play a role in the removal of the NSB proteins; however owing to the larger magnitude of tangential velocities, the drag induced particle advection plays a more prominent role as compared to the lift force.



(a)



(b)

Figure 3.5: Time Averaged Acoustic Streaming Velocity Profiles (a) Along the three principal directions. $v_{\text{tang},1}$ and $v_{\text{tang},2}$ denote tangential velocities along the propagation and transverse directions, respectively (b) Total acoustic streaming velocity.

One of the important factors in the NSB protein removal pertains to the thickness of the viscous boundary layer adjacent to the fluid-solid interface. The viscous boundary layer involved is defined as $\delta = \sqrt{2\nu/\omega}$, where δ is the thickness of the viscous boundary layer, ν is the kinematic viscosity of the fluid medium and $\omega = 2\pi f$ is the angular frequency of the surface acoustic wave. For the simulated viscosity employed in this study and the frequency of the surface waves, the thickness of the viscous boundary layer would be of the order of sub-micrometer length scale at MHz frequencies. For example, a SAW device operating at 100 MHz frequency and with a water loading ($\nu = 1 \times 10^{-6} \text{ m}^2/\text{s}$), the thickness of the viscous boundary layer is 0.05 microns whereas for a SAW operating at 100 KHz, the viscous boundary layer thickness would be 1.8 microns. It is noteworthy that protein molecule agglomerates are typically in the sub-micron size range. Therefore, the thinner boundary layer for MHz frequencies would minimize particle “hideout” as compared to devices operating at KHz frequencies.

Inside the viscous boundary layer, the simulations indicate that there is eddy formation resulting from the circular flow as the medium has to conform to the no slip condition at the fluid-solid interface. The medium outside this boundary layer vibrates irrotationally in accordance with the sound field. Therefore, the extent of viscous dissipation resulting from the vortex formation near the SAW-fluid interface would be higher at ultrasonic frequencies than under megasonic frequencies and fluid viscosity would have a critical role to play. Therefore, particle removal in viscous liquid loading at the ultrasonic (KHz) frequencies would be more difficult to achieve than under megasonic (MHz) frequencies. This clearly illustrates the role of fluid properties in biofouling elimination. The current 3-D FSI model takes into account the viscous and density effects and provides a more realistic description of the system dynamics.

The model developed for LiNbO_3 is further extended to study acoustic wave interaction with fluid domain in langasite, and is discussed in the forthcoming chapters.

3.4 Conclusion

To summarize, a three dimensional bi-directionally coupled fluid-structure interaction model, of a LiNbO_3 based SAW device in contact with fluid loading, was developed to investigate the interaction of the device with the fluid domain and gain insights into the acoustic streaming phenomenon. Device surface displacement and fluid velocity profiles indicate strong coupling of the fluid with solid domain and leakage of acoustic energy into the fluid domain, thereby launching longitudinal waves into the fluid. This attenuation of sound waves leads to an acoustically driven phenomenon known as acoustic streaming. The model predicts fluid velocities in accordance with the experimentally reported values. Further, the streaming velocities computed as the time average of the first order fluid velocities indicate fluid recirculation beyond the initial fluid thickness in contact with the piezoelectric domain. The model results also indicate that the hydrodynamic drag and lift forces exerted due to the tangential and normal velocity components play a role in NSB protein removal from the device surface; however the drag force plays a more significant role compared to the lift force. The developed model can be used to study acoustic streaming phenomenon in more complex transducer geometries and devices involving propagation of mixed waves. In a broader context, the FSI models developed in this work can be used to understand fluid motion and flow fields while accurately taking into account the structural dynamics. This has tremendous significance in potential microfluidics and biosensing applications.

Chapter 4

Orthogonal Surface Acoustic Wave Device based on Langasite for Simultaneous Biosensing and Bio-fouling Removal

This chapter reports on the first combined 3-D structural and fluid structure interaction finite element study of an orthogonal surface acoustic wave (SAW) device based on Langasite (LGS). The simulation results indicate that simultaneous sensing and non-specifically bound protein removal can be achieved through the use of multidirectional transducers on a single piezoelectric device. Based on the simulation results, the current study finds that the (0, 22, 90) Euler direction on the LGS-based device is suitable for biosensing *via* propagation of pure shear-horizontal (SH) waves, whereas, the (0, 22, 0) direction allows for acoustic streaming induced bio-fouling removal, through the propagation of mixed mode waves with prominent surface normal component. This study reveals the possibility of integration of sensing and bio-fouling removal functions on a single SAW device, thereby enhancing sensor performance.

4.1 Introduction

Biological transducer based devices used in medical diagnostic applications suffer from the deficiency of analyte discrimination and decrease in sensitivity resulting from the binding of non-specific proteins on the sensor surface, which interferes with the sensing phenomenon [99, 110, 131]. In a surface acoustic wave (SAW) device utilizing Rayleigh waves, the device-fluid interaction creates a pressure gradient in the direction of acoustic wave propagation in the fluid, leading to an acoustically driven streaming phenomenon known as acoustic streaming [74, 75]

which can be used for removal of non-specifically bound (NSB) proteins to permit sensor reuse and improve device performance, as has been shown experimentally [99]. However, simultaneous sensing and NSB protein removal poses a significant challenge in biosensing applications.

In this chapter, a novel SAW biosensor based on a Langasite (LGS) substrate, is investigated, to analyze its suitability for simultaneous biosensing and bio-fouling removal by employing multidirectional interdigital transducers (IDTs), using a finite element model. LGS offers considerable advantages for use in SAW sensors, which include a zero temperature coefficient, low sensitivity to process parameters, low phase velocity, low diffraction [19], high dielectric permittivity [20] and low level of bulk excitation waves [19] which would lead to smaller insertion loss and a high phase transition temperature of 1400 deg C [22], making it suitable for high temperature treatment during the fabrication process. Furthermore, LGS has a stronger electromechanical coupling coefficient compared to α -quartz, which is desirable especially in applications where a Rayleigh wave is excited in the SAW device [22]. Since biosensors typically operate in a fluid media, understanding the acoustic wave propagation and the sensing mechanism in SAW biosensors involving fluid interactions with complex multi-directional transducers represents a significant challenge. To-date, attempts to address this have relied on simplified numerical and analytical models or perturbation theories which neglect the mechanical properties of the fluid and treat the leaky wave as a first-order perturbation on the non-leaky wave associated with surface-wave propagation [103, 110]. This chapter reports on a 3-D fluid-structure interaction (FSI) model of SAW sensors. A novel multi-directional transducer design based on a LGS substrate is employed, to investigate the streaming velocity fields and forces induced by the SAW device.

4.2 Computational and Model Details

4.2.1 Fluid Domain

Fluid is modeled as an incompressible, viscous, Newtonian fluid using the Navier-Stokes and continuity equation in the Eulerian frame of reference given below:

$$\rho \left(\frac{\partial \mathbf{v}_f}{\partial t} + \mathbf{v}_f \cdot \nabla \mathbf{v}_f \right) + \nabla P - 2\eta \nabla \cdot \mathbf{D} = 0 \quad (4-1)$$

$$\nabla \cdot \mathbf{v}_f = 0 \quad (4-2)$$

Here, \mathbf{v}_f , P , ρ and η denote the fluid velocity, pressure, density, and viscosity, respectively. \mathbf{D} is the rate of deformation tensor given by

$$\mathbf{D} = \frac{1}{2} (\nabla \mathbf{v}_f + (\nabla \mathbf{v}_f)^t) \quad (4-3)$$

4.2.2 Piezoelectric Domain

For the piezoelectric solid, the equation of motion is obtained by modifying the elastic constitutive equation for a non-piezoelectric solid to account for the coupling between the electric field and mechanical strain. The interaction between the electric field and mechanical strain is studied by coupling the elastic and electromagnetic constitutive equations through a piezoelectric matrix [34, 116-119].

$$\underline{T} = [\underline{c}] \underline{S} - [\underline{e}] \underline{E} \quad (4-4)$$

$$\underline{D} = [\underline{e}]^T \underline{S} + [\underline{\varepsilon}] \underline{E} \quad (4-5)$$

The resulting equations, known as the piezoelectric constitutive equations, describe the interaction between elastic strain, stress, and electric field in the piezoelectric substrate.

Here, \underline{T} and \underline{D} denote stress and electric flux density vectors, respectively. \underline{S} , \underline{E} denote structural strain and electric field intensity vectors, respectively. \underline{c} , \underline{e} , and $\underline{\varepsilon}$ represent structural elasticity

matrix at constant electric field, piezoelectric stress matrix, and dielectric matrix at constant mechanical strain, respectively.

In the absence of body force, the equation of motion is given by

$$\nabla \cdot T = \rho \ddot{u} \quad (4-6)$$

where ρ is the density and u represents displacement, $\ddot{u} = \frac{\partial^2 u}{\partial t^2}$

The electric field intensity is given by the gradient of the electric potential (φ)

$$E = -\nabla \varphi \quad (4-7)$$

The strain tensor is symmetric, therefore

$$S_{ij} = \frac{1}{2} \left(\frac{\partial u_i}{\partial x_j} + \frac{\partial u_j}{\partial x_i} \right) \quad (4-8)$$

Substituting eqns. (4-7) and (4-8) in eqn. (4-4), we obtain T in tensor notation as

$$T_{ij} = \sum_{k,l=1}^3 c_{ijkl} \frac{\partial u_l}{\partial x_k} + \sum_{k=1}^3 e_{ijk} \frac{\partial \varphi}{\partial x_k} \quad (4-9)$$

Substituting eqns. (4-7), (4-8), (4-9) in eqn. (4-6),

$$\sum_{j,k,l=1}^3 c_{ijkl} \frac{\partial^2 u_l}{\partial x_k \partial x_j} + \sum_{j,k=1}^3 e_{ijk} \frac{\partial^2 \varphi}{\partial x_k \partial x_j} = \rho \frac{\partial^2 u_i}{\partial t^2} \quad (4-10)$$

In a system with no free charges,

$$\nabla \cdot D = 0 \quad (4-11)$$

Combining eqns. (4-5), (4-7), and (4-11),

$$\sum_{j,k,l=1}^3 e_{jkl} \frac{\partial^2 u_l}{\partial x_k \partial x_j} - \sum_{j,k=1}^3 \epsilon_{jk} \frac{\partial^2 \varphi}{\partial x_k \partial x_j} = 0 \quad (4-12)$$

Equation (4-10) represents three equations in four unknowns, namely the three displacements and the voltage (φ) which combined with equation (4-12), forms a set of coupled wave equations that

can be solved for the four unknowns. These equations are discretized in space and time, and solved at the nodes in the finite element domain to obtain a transient solution.

4.2.3 Fluid-Solid Interaction

The solution of fluid and solid fields in the finite-element domain requires the use of either the Lagrangian or Eulerian frame of reference. The Eulerian frame refers to the fixed frame of reference whereas Lagrangian frame is a moving frame of reference. In the Lagrangian frame, the grid deforms as the region of interest deforms. Whereas the structural phase (piezoelectric substrate) is best described using the Lagrangian frame, either frame of reference can be used for the fluid domain. In the Lagrangian frame, the mesh embedded in the fluid domain moves with the velocity of the fluid while in the Eulerian frame, the mesh, through which the fluid moves, is fixed. A purely Lagrangian frame is not suitable for dealing with strong distortions of the fluid mesh arising from the non-cohesive nature of fluid particles which causes them to travel independently and diverge in space. A purely Eulerian frame for the fluid domain introduces complexity in fluid-solid coupling as it is unable to track the path of the elements. Therefore, Arbitrary-Lagrangian-Eulerian (ALE) methods, which combine the best of the both frames of reference, are used for kinematical description of the fluid domain in such problems. In ALE, the Lagrangian frame is used for ‘almost contained’ flows and Eulerian description is used for regions where the mesh would be highly distorted if required to follow fluid motion. The theory for ALE has been developed by Hughes et al. for viscous, incompressible flows [120]. In the ALE framework, the fluid equation of motion can be written as [121]

$$\rho \left(\frac{\partial v_f}{\partial t} \right) + (v_f - w) \cdot \nabla v_f + \nabla P - 2\eta \nabla \cdot D = 0 ; \quad (4-13)$$

where w is the grid velocity such that $w \neq v_f \neq 0$.

To achieve fluid-solid coupling, an interface is defined across which displacements are transferred from solid to fluid and pressure from fluid to solid. These conditions translate to no-slip for the fluid domain (velocity continuity) and stress continuity for solid domain. The fluid mesh is continuously updated as the piezoelectric substrate undergoes deformation.

$$v_f = v_s = \frac{\partial u}{\partial t} \quad (4-14)$$

$$\sigma_{ij}^s n_j^s + \sigma_{ij}^f n_j^f = 0 \quad (4-15)$$

n_j is the outward normal at the solid-liquid interface in the deformed configuration, i denotes longitudinal direction. Superscripts f and s denote fluid and structural domain, respectively.

4.2.4 Finite Element Model

3-D Structural and FSI finite element (FE) models of a SAW device based on LGS substrate, with dimensions of 800 μm length X 400 μm depth X 200 μm height, were developed. Figure 4.1 shows the IDT configuration of the simulated orthogonal SAW device, with IDT finger pairs defined on the surface for each port along (0, 22, 0) and (0, 22, 90) Euler directions.

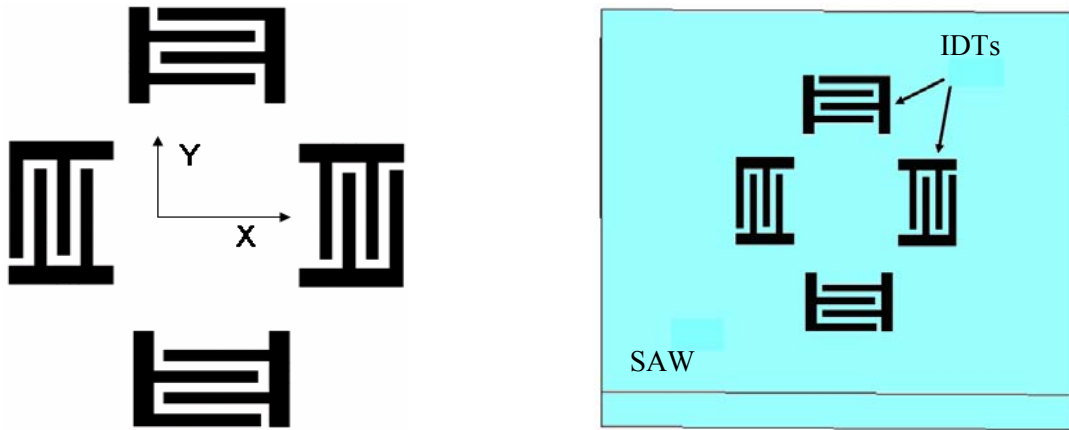


Figure 4.1: Schematic Diagram of an Orthogonal Surface Acoustic Wave Device simulated in the Current Work. X and Y denote (0, 22, 90) and (0, 22, 0) directions in the Langasite substrate, respectively. Each of the delay paths were simulated independently.

The material properties for LGS substrate are summarized in Table 4.1 [132]. The piezoelectric and elastic stiffness constants were rotated to obtain the values along the (0, 22, 0) and (0, 22, 90) directions. The IDT fingers were represented by a set of nodes coupled by voltage degrees of freedom (DOF). The fluid region, with 50 μm height, was modeled as an infinite reservoir of Newtonian, incompressible fluid subject to stress free boundary condition at the free surface (i.e. $P=0$). The piezoelectric domain was meshed using three dimensional twenty node coupled field solid elements with four DOF to account for the three translations and the voltage. The fluid domain was meshed using eight node fluid elements and discretized employing an Arbitrary Lagrangian Eulerian (ALE) frame for the kinematical description. The FSI model contained millions of nodes and elements: specifically, 2, 217, 889 nodes and 2, 085, 525 elements; a total of 208, 640 nodes and 144, 022 elements were generated for the structural model. The meshed FSI model with fluid loading is shown in Figure 4.2.

Table 4.1: Density (ρ , kg/m^3), Elastic Stiffness Constants (C_{ij} , GPa), and Piezoelectric Constants (e_{ij} , C/m^2) for Langasite [132]

ρ	5724
C_{11}	189.5
C_{33}	262.6
C_{44}	53.50
C_{66}	42.09
C_{12}	105.4
C_{13}	97.16
C_{14}	14.25
e_{11}	-0.397
e_{14}	0.203

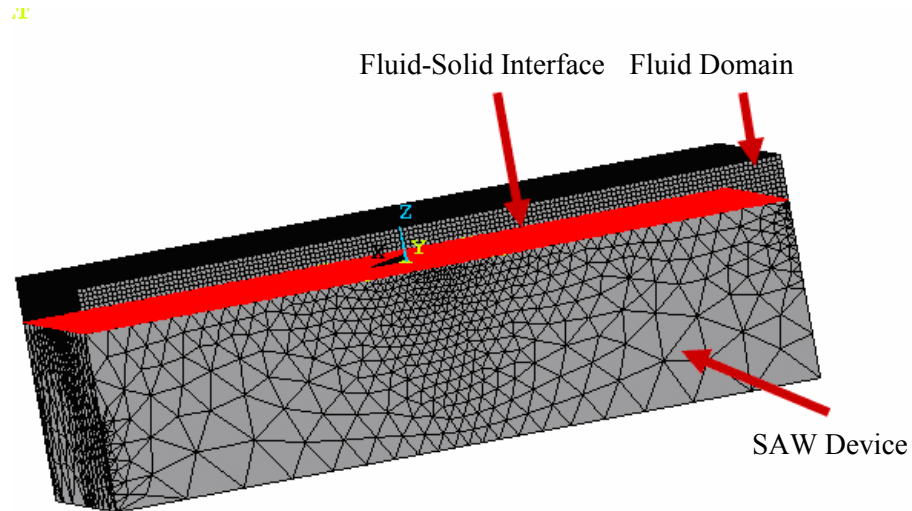


Figure 4.2: Meshed Fluid-Structure Interaction Model of the SAW Device With Fluid Loading. High mesh densities were ensured near the device surface to capture the dynamics at the surface which undergoes highest deformation. The FSI model shown here contained millions of nodes and elements: 2, 217, 889 nodes and 2, 085, 525 elements were generated.

Numerical solutions were obtained by sequentially solving the generalized Navier-Stokes equation for the fluid domain and acoustoelectric equations for the solid motion [110], employing the iterative sequential coupling algorithm[133]. In this algorithm, the governing equations for the two domains are solved separately and the solver iteration between the two domains continues till convergence of the load transferred across the interface is achieved.

4.3 Results and Discussion

4.3.1 Frequency Response

The frequency response of the device to an input impulse voltage applied at the transmitter IDT was utilized to deduce the central frequency of the device. The insertion loss of the device

was computed by taking the Fourier transform of the voltage profile at the output IDTs. Based on the insertion loss, the central frequency of the device was computed which was computed to be 68 MHz (Figure 4.3). Wave propagation characteristics and acoustic streaming velocities were obtained by transient ac analysis with a peak voltage of 2.5 V and frequency of 68 MHz applied to the transmitter IDT fingers, using a time step of 1 ns.

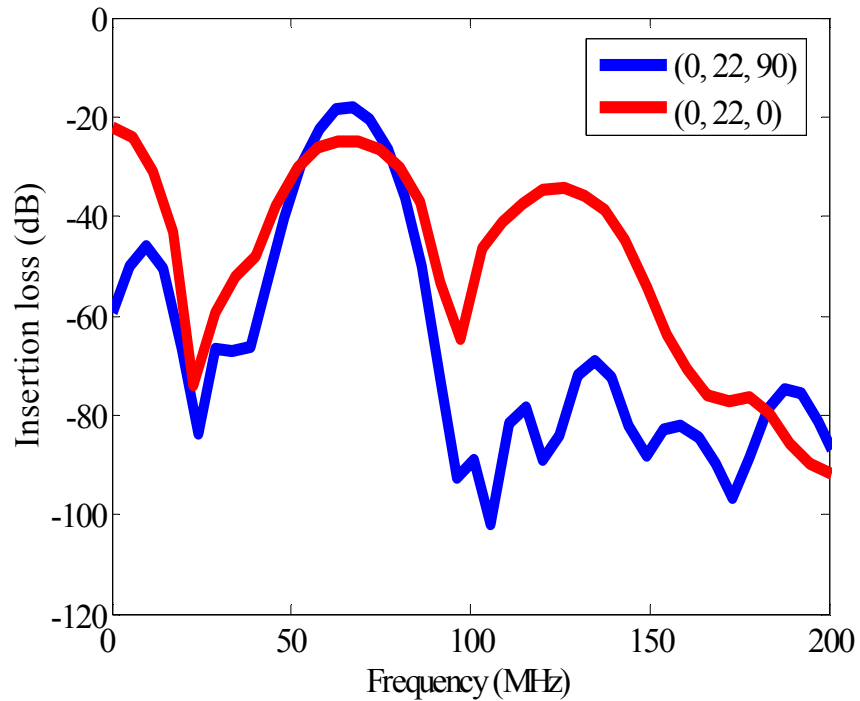


Figure 4.3: Calculated Frequency Response Along (0, 22, 0) and (0, 22, 90) Euler Directions in the Simulated Orthogonal SAW Device.

4.3.2 AC Analysis: Wave Propagation Characteristics and Device Sensitivity

An analysis of the wave propagation characteristics indicates the propagation of a pure shear horizontal (SH) mode along the on-axis (0, 22, 90) direction with a negligible surface normal component (Figure 4.4) leading to negligible coupling with the fluid domain, thereby making it suitable for biosensing.

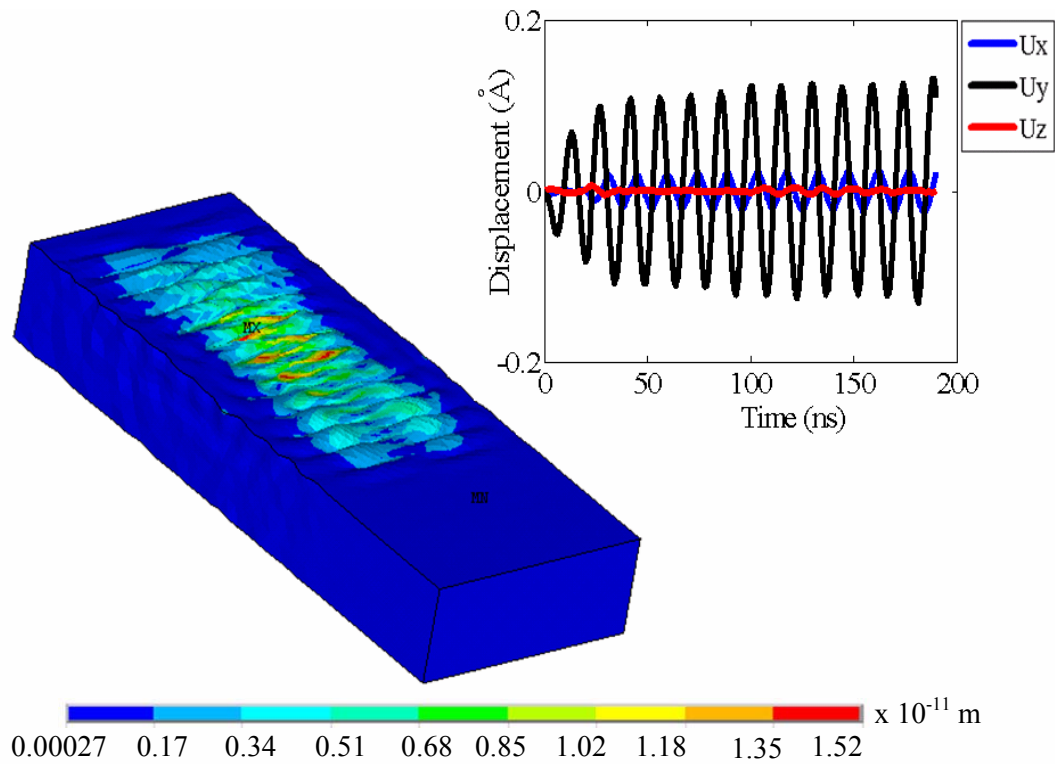
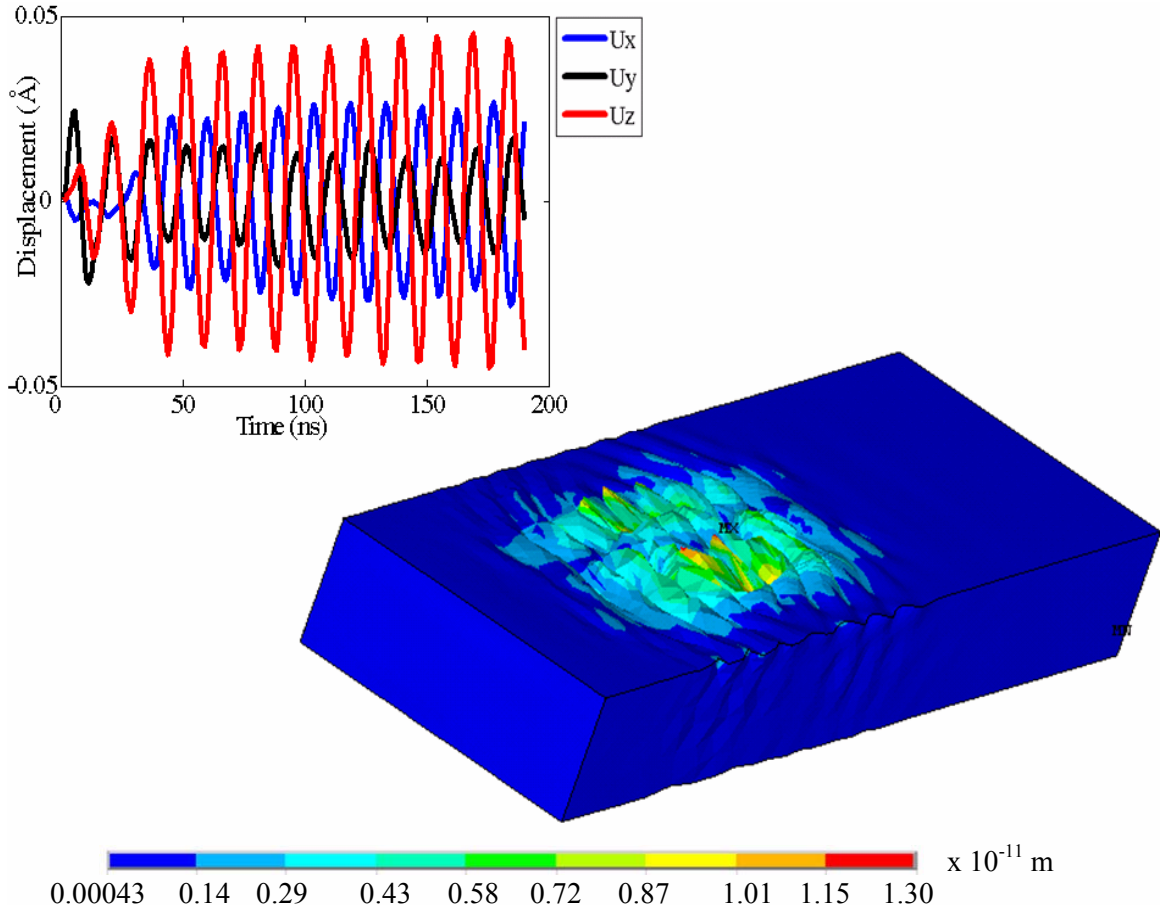


Figure 4.4: Contour Plot Showing Shear Horizontal Wave Propagation Along the (0, 22, 90) Direction on Langasite Substrate. Scale bar is in meters. Inset shows particle displacement profiles along the three principal directions for IDTs along the (0, 22, 90) direction. The device is not drawn to scale.

Propagation along the (0, 22, 90) direction indicates shallow penetration depth, rendering it suitable for liquid sensing applications such as those in biosensing in bodily fluids. Further, the (0, 22, 0) direction shows the presence of mixed modes (Figure 4.5). Despite the wave mode being mixed, the surface normal component is the dominant component in the (0, 22, 0) direction suggesting strong coupling with the fluid domain, and can thus be utilized for acoustic streaming to achieve removal of NSB proteins from the device surface.



(b)

Figure 4.5: Contour Plot Showing Mixed Mode Wave Propagation Along the (0, 22, 0) Direction on Langasite Substrate. Scale bar is in meters. Inset shows particle displacement profiles along the three principal directions for IDTs along (0, 22, 0) direction. The device is not drawn to scale.

In addition, the computed sensitivity along (0, 22, 90) direction to a 100 pg applied mass was found to be higher for the LGS device in comparison to a SAW device based on the competitive and practical 36° YX LiTaO₃ [134] substrate (11.09 Hz-cm²/ng vs. 2.98 Hz-cm²/ng, details shown in Figure 4.6). Figure 4.3 also indicates that the insertion loss for propagation in the (0, 22, 90) direction is ~ 6.9 dB lesser as compared to that for propagation along the off-axis (0, 22, 0) direction, thus suggesting increased sensitivity in the former configuration.

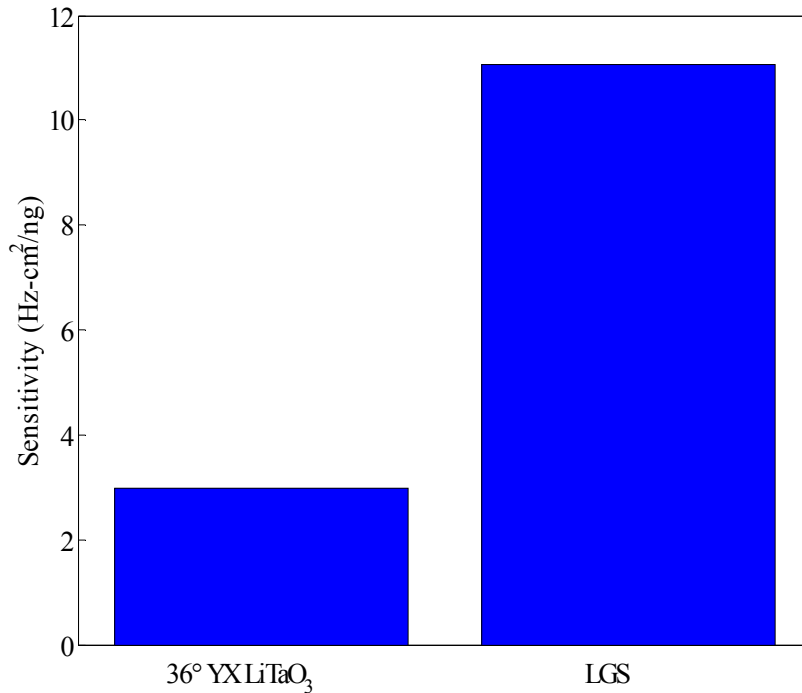


Figure 4.6: Comparison of Sensitivities for the Langasite Substrate for Propagation Along the (0, 22, 90) Euler Direction and a Comparable 36° YX-LiTaO₃ Substrate. FE models were created for 100 pg mass applied over an area of 9600 μm² in the delay path of the SAW device based on Langasite. Transient analysis was utilized to study transmission characteristics of this ideal mass perturbed sensor. The sensitivity obtained for the LGS SAW device in the current study is compared with that for the 36° YX LiTaO₃ device obtained by Cular *et al.*[134], using the same approach as outlined [134]. The sensitivity for the 100 MHz 36° YX LiTaO₃ device is scaled to match the centre frequency (68 MHz) of LGS.

4.3.3 Acoustic Streaming Velocity

The acoustic streaming velocities were computed and analyzed using the 3D FE-FSI model of the device with propagation along the (0, 22, 0) direction. The fluid motion induced by the piezoelectric actuation at a given time instant, shown in Figure 4.7, indicate that most of the fluid motion is

confined to the region near the device surface and that the velocities are of the order of mm/s in accordance with the experimentally reported values [3]. The highest fluid velocity is observed near the IDTs and decays rapidly on moving away from them. The solid displacement also decays along the delay path, suggesting acoustic energy dissipation leading to a mode conversion from Rayleigh to leaky SAW. This mode conversion results in longitudinal wave propagation in the fluid domain which, if of sufficiently high intensity, results in a net pressure gradient along its direction of propagation thereby inducing fluid flow. The fluid motion resulting from the attenuation of sound wave induces acoustic streaming. The steady state streaming velocities, computed as the average over a time period, are shown in Figure 4.8. The streaming velocity profiles show that the fluid attains the highest velocity before undergoing flow reversal and recirculation close to the device surface, beyond which there is significant dampening of the fluid motion. Fluid motion, observed near the device surface, exerts stresses on the fluid-structure interfacial boundary which in turn induce the removal of loosely and NSB proteins from the device surface. Whereas the tangential components of the fluid velocity exert viscous shear stress creating a drag force, the normal component exerts a lift force [135]. The 3D FSI model results indicate that the tangential velocity component along the propagation direction is predominant, suggesting that the drag force is significantly greater than the lift force and therefore, the particle advection induced by the former is the dominant mechanism of bio-fouling removal for the SAW sensor based on LGS.

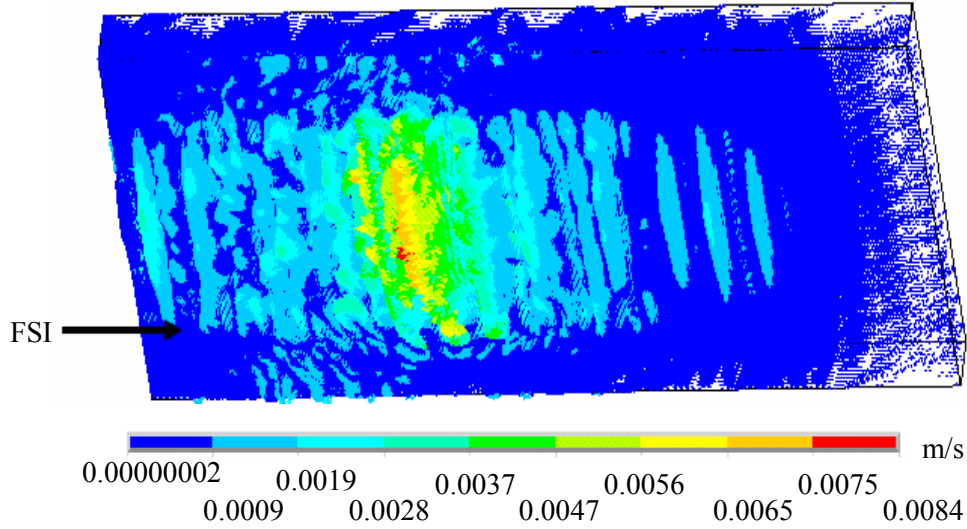


Figure 4.7: Simulated Fluid Velocity Vector Profile for a Peak Input AC Voltage of 2.5V Applied to the Langasite SAW Device Operating at 68 Mhz. Scale bar is in m/s.

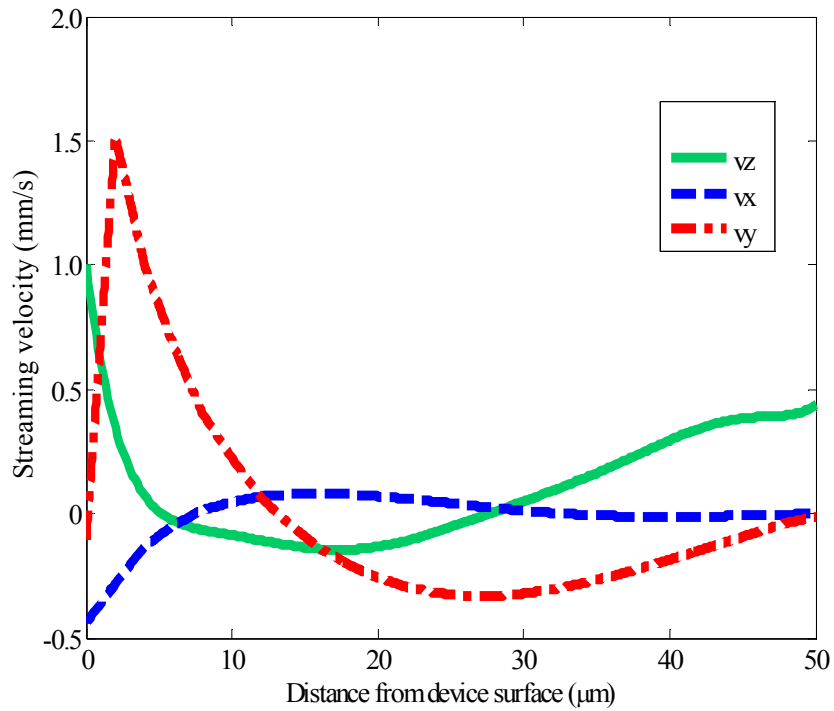


Figure 4.8: Streaming Velocity Profiles Along the Fluid Film Thickness Computed by Time Averaging, for a Peak Input AC Voltage of 2.5V Applied to the Langasite SAW Device Operating at 68 Mhz.

4.3.4 Adhesive And Removal Forces

The various removal forces, namely the SAW body force, lift force, and drag force were computed using the simulated fluid velocities as outlined [110] and compared with the adhesive force to predict a bio-fouling removal mechanism. The comparisons (Table 4.1) reveal that for a demonstrative particle radius of 1 μm , the fluid induced lift force ($1.0 \times 10^{-15} \text{ N/m}^2$) is significantly smaller than the drag force ($1.8 \times 10^{-12} \text{ N/m}^2$) and neither of these two forces is sufficient to overcome the Van der Waals force of attraction ($-4.2 \times 10^{-8} \text{ N/m}^2$). Interestingly, the SAW body force ($3.3 \times 10^{-5} \text{ N/m}^2$) overcomes the Van der Waals force to detach the non-specific protein particles and move them away from the surface till the adhesive force decreases significantly. Since the SAW body force also decreases on moving away from the device surface, the fluid induced lift and drag forces come into play away from the surface to prevent NSB protein reattachment to the surface and facilitate its removal from the fluid stream, respectively. Thus, the mixed modes, as observed for propagation along the off-axis (0, 22, 0) direction in LGS, are instrumental in bio-fouling removal. It is worth mentioning that owing to the pure SH mode propagation along the on-axis direction (0, 22, 90), the calculated removal (particularly SAW body) force is significantly smaller than the adhesive force indicating non-feasibility of NSB protein removal in a single IDT configuration and necessitating a multi directional IDT configuration to achieve the dual objective of sensing and bio-fouling removal. Furthermore, the minimum protein radius that can be removed using the phenomenon of acoustic streaming in the vicinity of the IDTs, computed in the limit when the dominant removal force equals the non-specific adhesive Van der Waals force, reduces as the number of IDT finger pairs is increased (Table 4.2). This is due to the fact that dominant removal force increases with increasing number of IDT pairs (Table 4.2), thereby facilitating removal of smaller sized proteins. It should be noted that with increasing distance from the IDTs, the amplitude of the displacement decays resulting in decreased removal efficiency away from the IDTs.

Table 4.2: Comparison of Non-Specific Adhesive and Removal Forces for Particles on a 70 MHz SAW Device Based on Langasite for Propagation Along the Off-Axis (0, 22, 0) Direction. The calculated forces are based on the fluid velocity fields generated near the device surface close to the IDTs. The particle diameter R is varied from 0.1 μm to 10 μm and typical displacement amplitude of 2.5 nm is used.

Forces (N)	Particle radius R (μm)		
	0.1	1	10
F_{vdw}	-4.2×10^{-9}	-4.2×10^{-8}	-4.2×10^{-7}
F_{SAW}	3.3×10^{-7}	3.3×10^{-5}	3.3×10^{-3}
F_{L}	1.0×10^{-17}	1.0×10^{-15}	1.0×10^{-13}
F_{ST}	1.8×10^{-13}	1.8×10^{-12}	1.8×10^{-11}

Table 4.3: Calculations of Removal Force for Different Number of IDT Pairs and Comparison With Non-Specific Adhesive Force. Also included is the minimum protein radius which can be removed.

Number of IDT pairs	Particle radius R = 1 μm		Minimum protein radius which can be removed R_{min} (nm)
	Non-specific adhesive force F_{vdw} (N)	Dominant removal force F_{SAW} (N)	
3	-4.2×10^{-8}	3.3×10^{-5}	1.28
5	-4.2×10^{-8}	4.2×10^{-5}	0.99
7	-4.2×10^{-8}	4.7×10^{-5}	0.89

4.4 Conclusion

To summarize, it has been shown that multidirectional transducer based SAW devices on a single piezoelectric substrate offer the advantage of selectively exploiting features which are specific to acoustic waves propagating along a given crystallographic orientation. Computational modeling on an orthogonal SAW device based on LGS indicates differing characteristics of acoustic waves propagating in different Euler directions facilitating the incorporation of dual functionality of target analyte detection and NSB protein elimination, in the same device, which can lead to enhanced device performance. In the simulated device, the (0, 22, 90) direction is suitable for biosensing and (0, 22, 0) direction for potential application in removal of NSB proteins through acoustic streaming. These results are of tremendous significance for not only improving the device design, but also for understanding biosensing mechanisms in multi-directional acoustic wave devices as well as actuation mechanisms in potential microfluidic applications of these devices.

Chapter 5

Enhanced SAW Biosensor Performance *via* Integrated Transducer and Delay Path Modifications: A Computational Study

Integrated multi-directional inter-digital transducers (IDTs) and delay path modifications for surface acoustic wave (SAW) sensors in a Langasite substrate are shown to positively and significantly impact power consumption, device sensitivity, and bio-fouling elimination capability. Simulated devices have mutually interacting orthogonal IDTs and micro-cavities of square cross-sections of side $\lambda/2$, and of different depths located in the middle of the delay path. A combined orthogonal IDT- polystyrene filled micro-cavities device (of dimensions $\lambda/2 \times \lambda/2 \times \lambda/2$), with constructive wave interference and enhanced surface acoustic wave entrapment in the delay region, is shown to be most efficient and reduces insertion loss by 23.6 dB, generates two orders of magnitude larger streaming forces, and exhibits velocity sensitivity 100% larger than that of a simulated standard SAW sensor with unidirectional IDTs along the (0, 22, 90) direction.

5.1 Introduction

Recent challenges for developing reliable and efficient biosensors include factors such as power consumption, sensitivity, and reproducibility. In biosensing applications, one of the most critical issues is biofouling which arises from the binding of non-specific proteins to the sensor surface[110, 131]. Biofouling can drastically reduce the sensitivity, selectivity, and reproducibility[99]. Conventional methods of improving SAW device sensitivity include the use of either a waveguide to create Love wave devices or lithographic techniques to reduce the

interdigital finger spacing thereby reducing the acoustic wavelength [136]. However, these methods are insufficient to address the critical issue of biofouling. One of the ways to eliminate biofouling involves the use of acoustic streaming induced forces to overcome the adhesive forces between the sensor surface and non-specifically bound proteins [99, 110]. Multidirectional transducer configurations [15] which allow for the generation of streaming through acoustic modes with a prominent surface normal component along one direction and shear horizontal mode along the other can lead to simultaneous biofouling elimination and sensing. Sensitivity enhancement due to coherent wave interaction in the common region being probed can also be achieved. Such devices involve complex non-linear interactions arising from mutually interacting transducers which cannot be accounted for by using simple analytical and numerical models. This work investigates a Langasite (LGS) based SAW device comprising of mutually interacting interdigital transducers (IDTs), utilizing coupled field finite element (FE) structural and fluid-structure interaction (FSI) analysis. The main focus of this work is the development of a biosensor device, with integrated delay path modifications and mutually interacting IDTs, which can provide enhanced sensitivity, reduced power loss and enhanced biofouling elimination capability on a single piezoelectric device.

Power consumption is another important issue in sensing applications. . Typical SAW delay line sensors are expected to have insertion loss in the range of 7-20 dB. Methods to reduce the SAW device power loss include utilization of reflective gratings, grooves and corrugated gratings, and waveguides to improve the conversion of bulk waves into surface waves and entrapment of energy near the surface that would otherwise be lost to bulk waves [47, 137]. It was recently reported that micro-cavities etched along the delay path of a 36-YX LiTaO₃ substrate can reduce insertion loss substantially (20 dB for the case simulated compared to a standard device with unidirectional IDTs and no delay path modifications) [134].

In this chapter, a novel SAW biosensor, with integrated multi-directional inter-digital transducers (IDT) and delay path modifications on a device based on a Langasite (LGS) substrate, is introduced. The choice of LGS was motivated due to its significant advantages over other standard substrates such as quartz investigated previously [69]. For example, shear horizontal (SH)-SAW mode on quartz suffers from low electro-mechanical coupling coefficients, high penetration depth, and low dielectric permittivity with respect to the liquid media while LGS offers considerable advantages which include a much stronger electromechanical coupling coefficient compared to α -quartz, desirable especially in applications where a Rayleigh wave is excited in the SAW device, a zero temperature coefficient, low sensitivity to process parameters, low phase velocity, low diffraction, high dielectric permittivity and low level of bulk excitation waves which would lead to smaller insertion loss and a high phase transition temperature of 1400 deg C, making it suitable for high temperature treatment during the fabrication process[19, 22, 138]. The investigated device design is a superior alternative to the available conventional devices and is shown to give significantly enhanced performance in terms of reduced power consumption, enhanced device sensitivity, and larger biofouling elimination efficiency. Coupled field FE analyses are used to first deduce the best case micro-cavity on a LGS surface. These micro-cavities are then integrated into an orthogonally-oriented, mutually-interacting IDT configuration to study the improvements in sensor performance (Fig. 5.1). To the best of my knowledge, this is the first study that simulates a device with interacting IDTs including the second order effects and non-linear interactions arising between surface and bulk modes which are excited by the IDTs.

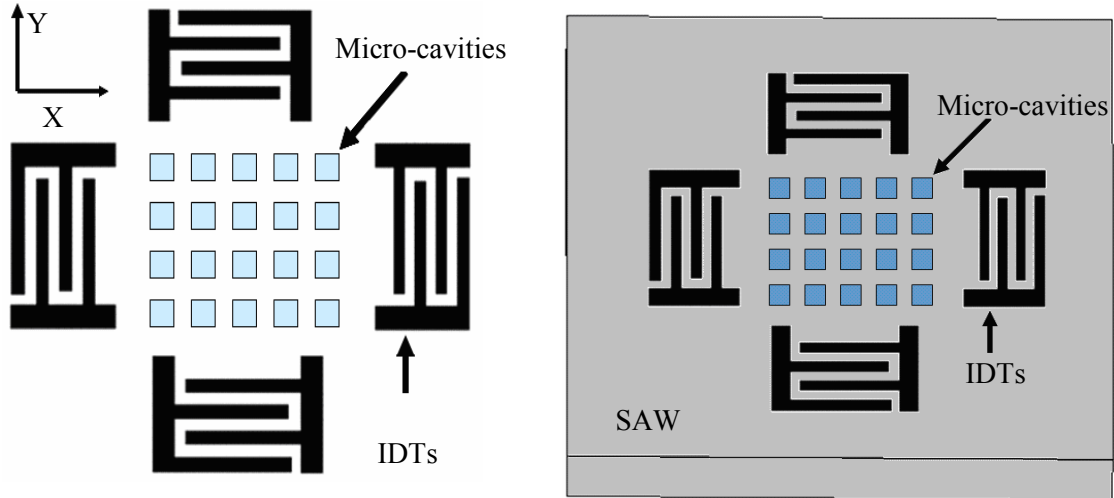


Figure 5.1: Schematic Diagram of a Mutually Interacting Orthogonal IDT Device With Micro-Cavities Etched Along the Delay-Path of the SAW Device. The device is not drawn to scale. X and Y directions denote different crystallographic directions allowing for propagation of waves of different characteristics.

5.2 Computational Details

5.2.1 Structural Model

FE models of a SAW device based on LGS substrate, with dimensions $1600 \mu\text{m}$ length x $1600 \mu\text{m}$ depth x $200 \mu\text{m}$ height, were developed. Figure 5.1 shows a schematic diagram of the simulated SAW device with orthogonal IDT configuration integrated with delay path modification, in the form of micro-cavities. IDT finger pairs, with width 2λ and periodicity $40 \mu\text{m}$, were defined on the surface for each port along $(0, 22, 0)$ and $(0, 22, 90)$ Euler directions. The piezoelectric domain was meshed using a three dimensional twenty node coupled field solid element with four degrees of freedom accounting for the three translations and voltage and ensuring high mesh densities near the surface. Impulse response analysis was performed during 190 ns by applying an impulse voltage of 100 V at the input IDT and employing a time step of 0.95 ns [15]. Subsequently, an ac analysis was carried out using a peak voltage of 2.5 V with the

device frequency obtained from impulse response analysis for each of the propagation directions. Using simulations involving unidirectional IDTs along (0, 22, 90) and (0, 22, 0) directions, it has been established that the (0, 22, 90) direction with pure SH mode is best suited for sensing and (0, 22, 0) with mixed modes can be used to generate streaming induced forces for bio-fouling elimination [139].

5.2.2 Fluid Structure Interaction Model

The fluid region, with 50 μm height, was modeled as an infinite reservoir of Newtonian, incompressible fluid on top of the piezoelectric domain, subject to stress free boundary condition at the free surface (i.e. $P=0$). The piezoelectric domain was meshed using a ten node tetrahedral coupled field solid element with four DOF to account for the three translations and the voltage. The fluid domain was meshed using eight node fluid elements and discretized employing an Arbitrary Lagrangian Eulerian (ALE) frame for the kinematical description. The FSI model contained millions of nodes and elements: 2, 217, 889 nodes and 2, 085, 525 elements. Numerical solutions were obtained by sequential solution of the generalized Navier-Stokes equation for the fluid domain and acoustoelectric equations for the piezoelectric motion [110], employing the iterative sequential coupling algorithm[133]. In this algorithm, the governing equations for the two domains are solved separately and the solver iteration between the two domains continues till convergence of the load transferred across the interface is achieved.

5.2.3 Best Case Micro-Cavities

To obtain the best micro-cavity configuration for sensing, 20 micro-cavities of $\lambda/2$ square cross sections with varying depths were etched on the device surface along the delay path with IDTs along the (0, 22, 90) direction. These micro-cavities were filled with a waveguide material polystyrene (PS) to provide increased entrapment of acoustic energy near the device surface [134].

5.3 Results and Discussion

5.3.1 Best Case Micro-Cavities

Based on the simulated node translation data, it is found that Love waves incident on a shallow groove or cavity on the surface of a piezoelectric substrate filled with another elastically isotropic material such as polystyrene are weakly scattered with a part of the energy contained in the reflected and the transmitted Love waves and the other part converted into the bulk shear waves that propagate into the substrate. The simulations indicate that PS filled micro-cavities with dimensions $\lambda/2 \times \lambda/2 \times \lambda/2$ exhibit the highest energy transmission and smallest insertion loss (lesser by 2 dB compared to the next best PS filled $\lambda/2 \times \lambda/2 \times \lambda/8$ micro-cavities) (Fig. 5.2). An analysis of displacement profiles for each of the simulated micro-cavity designs indicate that these improvements are brought about by a larger coherent reflection of the incident Love wave and subsequent reduced conversions into bulk shear modes which radiate into the substrate (Fig. 5.3). Details of the pass-bands are shown in Fig. 5.2 where a 21.8 dB increase in energy transmission is clearly shown for the best case micro-cavity over the SAW sensor with unidirectional IDTs along the (0, 22, 90) Euler direction and no delay path modifications (henceforth, referred to as standard SAW). Therefore, 20 PS-filled micro-cavities with dimensions $\lambda/2 \times \lambda/2 \times \lambda/2$ were incorporated in the delay path of a SAW device with

orthogonally-oriented, mutually-interacting IDTs along the (0, 22, 0) and (0, 22, 90) Euler directions.

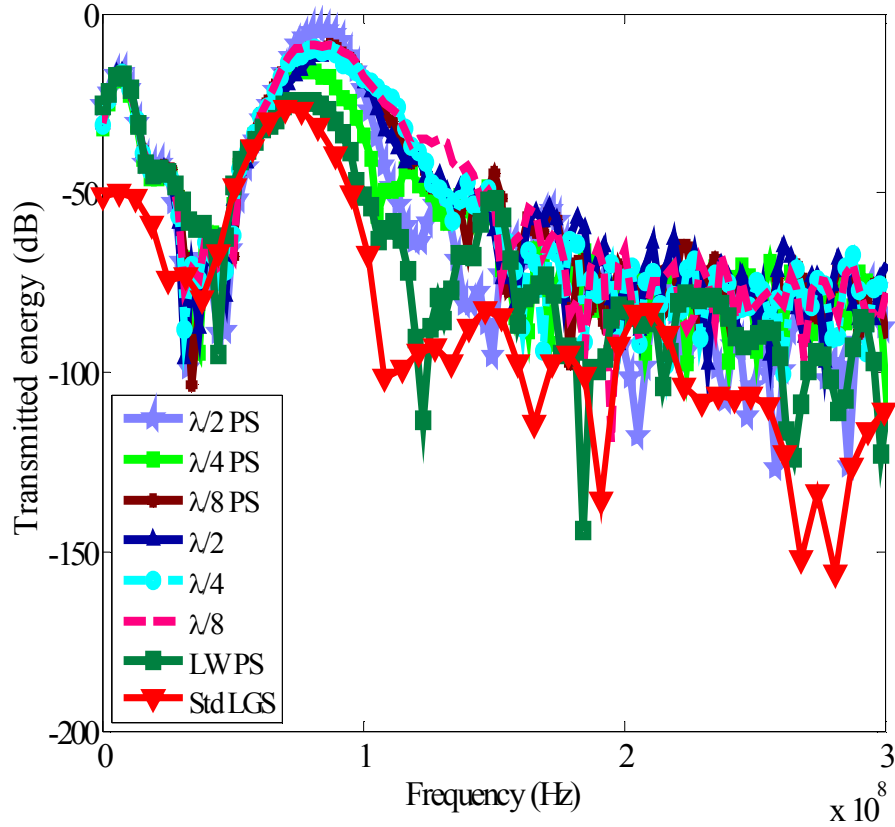
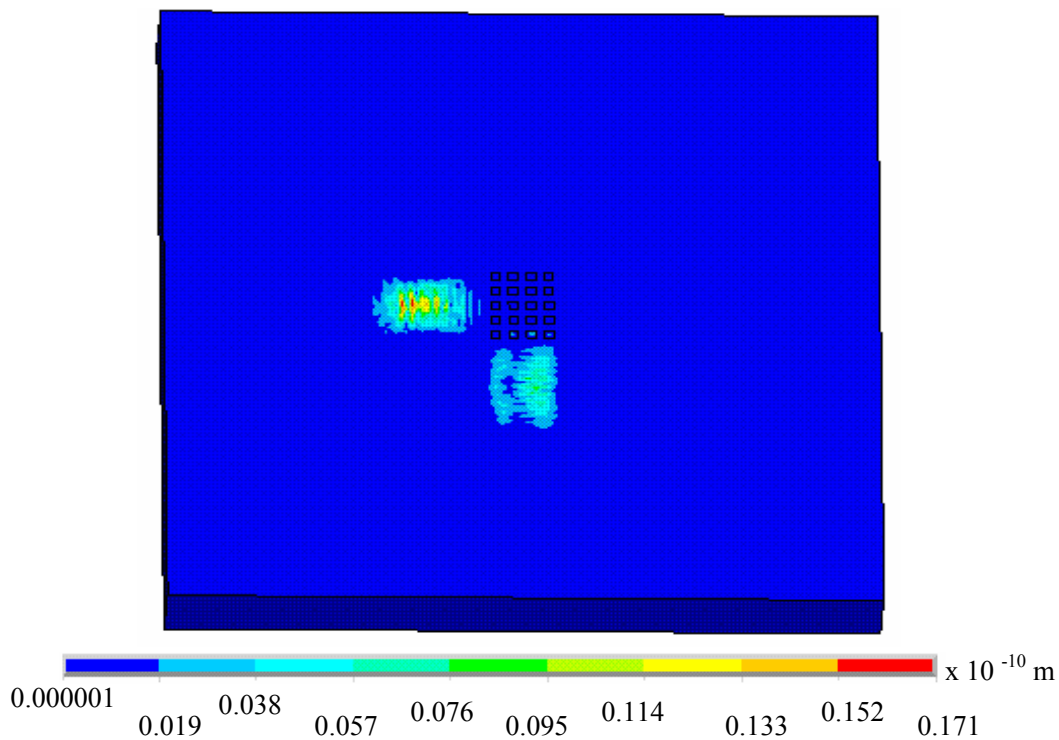


Figure 5.2: Comparison of Transmitted Energies for Empty and PS-Filled Micro-Cavities Having $\lambda/2$ Square Cross Section and Depths of $\lambda/4$, $\lambda/4$ and $\lambda/2$ With Standard LGS SAW Delay-Line Device and an Optimized LW Device. Std LGS refers to a device with unidirectional IDTs and no delay path modifications. PS filled micro-cavities with dimensions $\lambda/2 \times \lambda/2 \times \lambda/2$ exhibit the highest energy transmission and smallest insertion loss and form the best case configuration.

5.3.2 Device Displacements and Transmission Losses

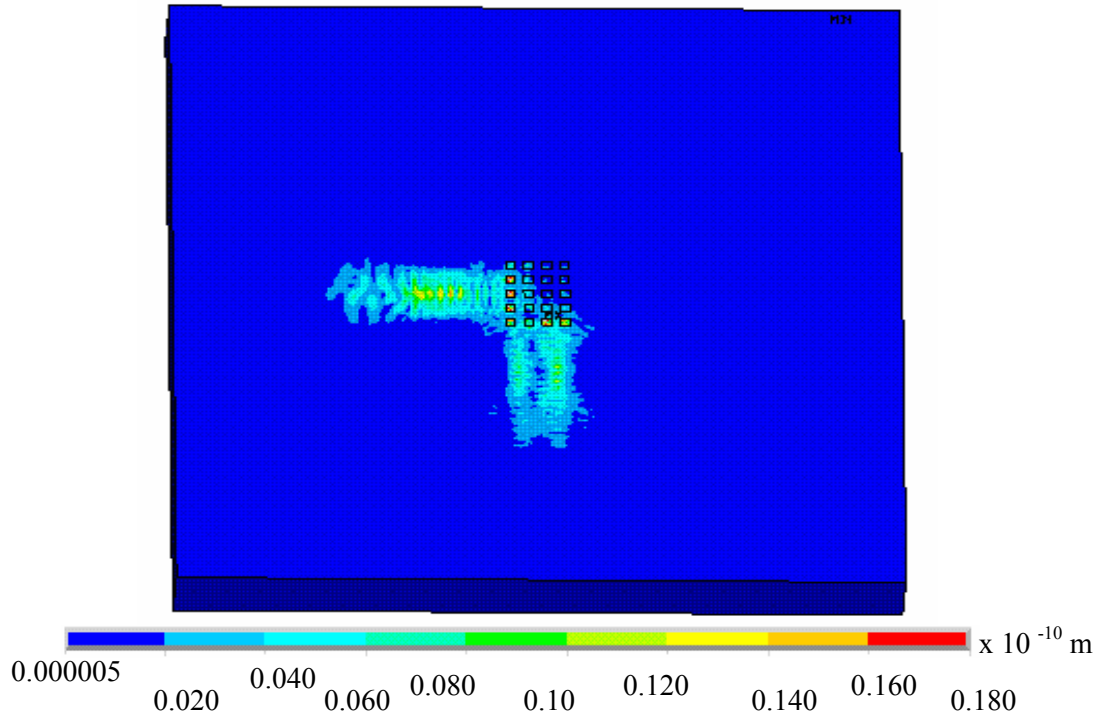
Figure 5.3 shows the displacement contours at various instants of time, showing surface wave propagation in the orthogonal SAW device with micro-cavities having depth $\lambda/2$ and square

cross section $\lambda/2$. The magnitudes of the surface displacements increase and the wave front marches forward towards the micro-cavities with time. The device displacement profiles indicate that the wave reaches the micro-cavities after almost 30 ns, beyond which the surface displacements are mostly confined to the micro-cavities. Maximized displacements are observed in the proximity of the micro-cavities owing to the larger coherent reflection of the incident Love wave and subsequent reduced conversions into bulk shear modes which radiate into the substrate [140, 141].

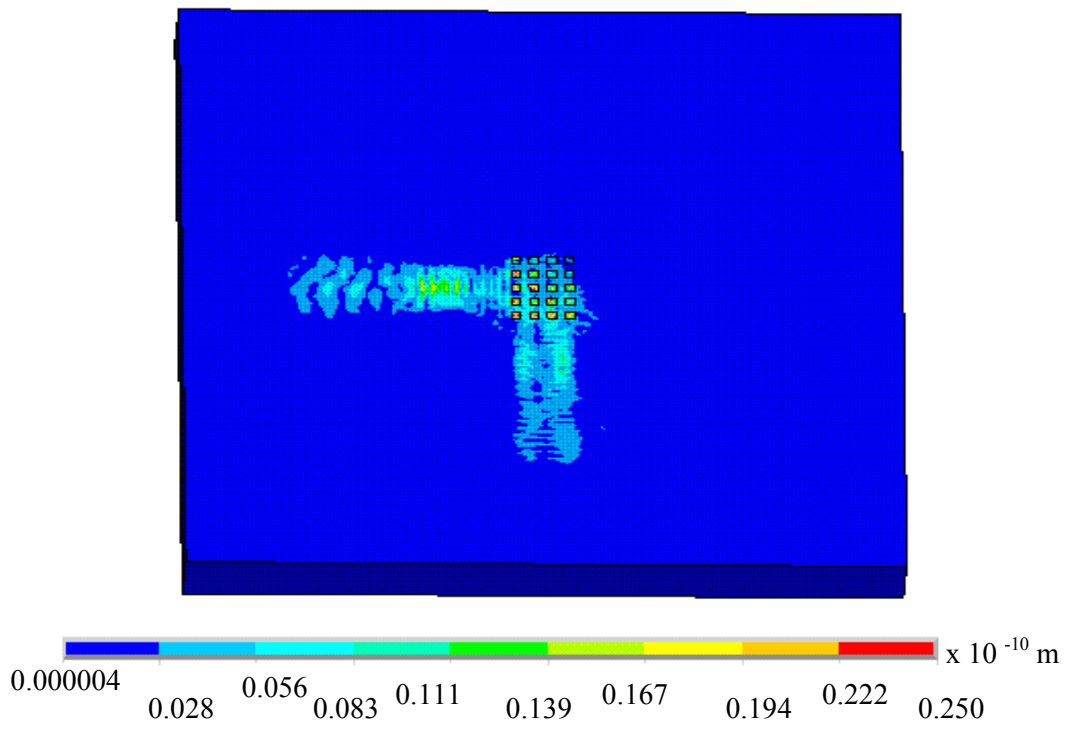


(a)

Figure 5.3: Snapshots of Displacement Contours Taken at Various Time Instants Showing Surface Acoustic Wave Propagation in the LGS Orthogonal SAW Device With Micro-Cavities ($\lambda/2 \times \lambda/2 \times \lambda/2$) in the Delay Path. Acoustic wave confinement leading to maximized displacements in the micro-cavities is clearly shown after the wave reaches the micro-cavities. Scale bar is in meters. (a) 30 ns (b) 70 ns (c) 100 ns (d) 180 ns.

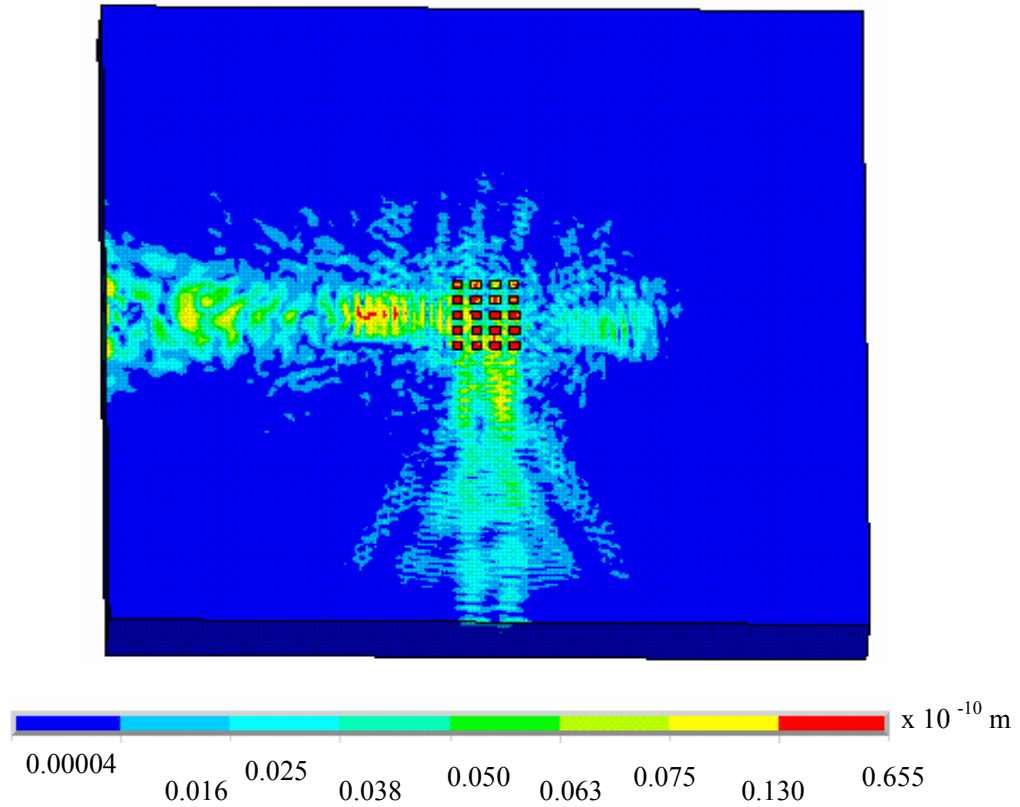


(b)



(c)

Figure 5.3: Continued.



(d)

Figure 5.3: Continued.

It is interesting to note from Fig. 5.4 that the orthogonal SAW device which includes non-linear interactions between the orthogonally propagating waves has smaller insertion loss compared to the unidirectional standard device. When two waves interact and superimpose, the particle displacement at a point is the vector sum of the individual wave displacements such that the resultant displacement is determined by the phase difference [34]. To analyze the nature of the wave interaction, the phase difference (ϕ) between the orthogonally propagating waves was computed. The calculated value of the phase angle ϕ ranges from 86.2 to 92.6 degrees for the different components of displacement, suggesting constructive interference between the waves. Therefore, the insertion losses in the orthogonal SAW device are smaller (by 15.6 dB) as

compared to a standard device with unidirectional IDTs, as seen in Fig. 5.4. Furthermore, for reasons stated before, the incorporation of micro-cavities in the delay path leads to further enhancement in surface acoustic energy entrapment, thereby further reducing the insertion loss by 8.0 dB. Thus, the smallest insertion loss was observed for orthogonal IDTs with micro-cavities in the delay path making it the best possible configuration amongst the simulated designs.

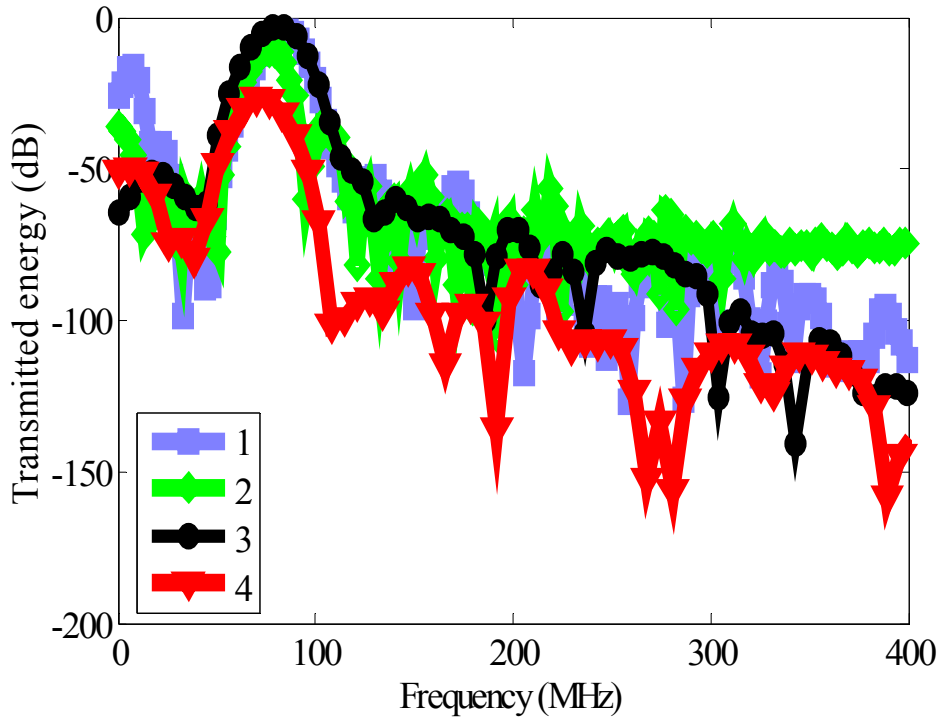


Figure 5.4: Comparison of Transmitted Energies for Different Device Configurations. (1) denotes unidirectional IDTs along $(0, 22, 90)$ with PS-filled micro-cavities $(\lambda/2 \times \lambda/2 \times \lambda/2)$ on LGS; (2) denotes mutually interacting orthogonal IDTs without micro-cavities; (3) denotes mutually interacting orthogonal IDTs with PS-filled micro-cavities $(\lambda/2 \times \lambda/2 \times \lambda/2)$; (4) denotes unidirectional standard LGS SAW device. Transmitted energies for all the devices shown are calculated at the output IDT port corresponding to propagation along the $(0, 22, 90)$ Euler direction.

5.3.3 Fluid Streaming and Biofouling Elimination

Bio-fouling elimination in the simulated orthogonal SAW device due to mixed mode waves propagating along (0, 22, 0) Euler direction is dependent on the magnitude of the induced acoustic streaming forces given by [124, 139, 142]:

$$F = -\rho (1 + \alpha^2)^{3/2} A^2 \omega^2 \alpha k_i \exp 2(k_i x + \alpha k_i z) \quad (5-1)$$

Here, α and k_i refer to the attenuation constant and leaky SAW wave number, respectively, and are obtained using a perturbation approach [102, 103]. And, ω refers to the angular frequency and A refers to the acoustic wave displacement, which are obtained using FE simulations. The induced streaming forces for water loading (density $\rho = 1000 \text{ Kg/m}^3$) for the various device designs are shown in Fig. 5.5. Owing to the constructive interference of the orthogonally propagating waves, the resultant displacement amplitudes are much larger than in the unidirectional standard SAW device, which in turn lead to higher fluid velocities in the former configuration. As a result, the streaming force in orthogonal SAW device ($F=3.24 \times 10^5 \text{ N/m}^2$), computed using Eq. (5-1), is an order of magnitude larger than that in the standard SAW device ($F=5.44 \times 10^4 \text{ N/m}^2$). Integration of the orthogonal SAW device with delay path modifications in the form of PS filled micro-cavities leads to significantly enhanced surface acoustic energy entrapment (Fig. 5.3), which further contributes to an increase in the generated streaming force ($F=3.49 \times 10^6 \text{ N/m}^2$, *i.e.*, two orders larger than in the standard SAW device, Fig. 5.5), leading to much larger removal efficiency of non-specifically bound proteins.

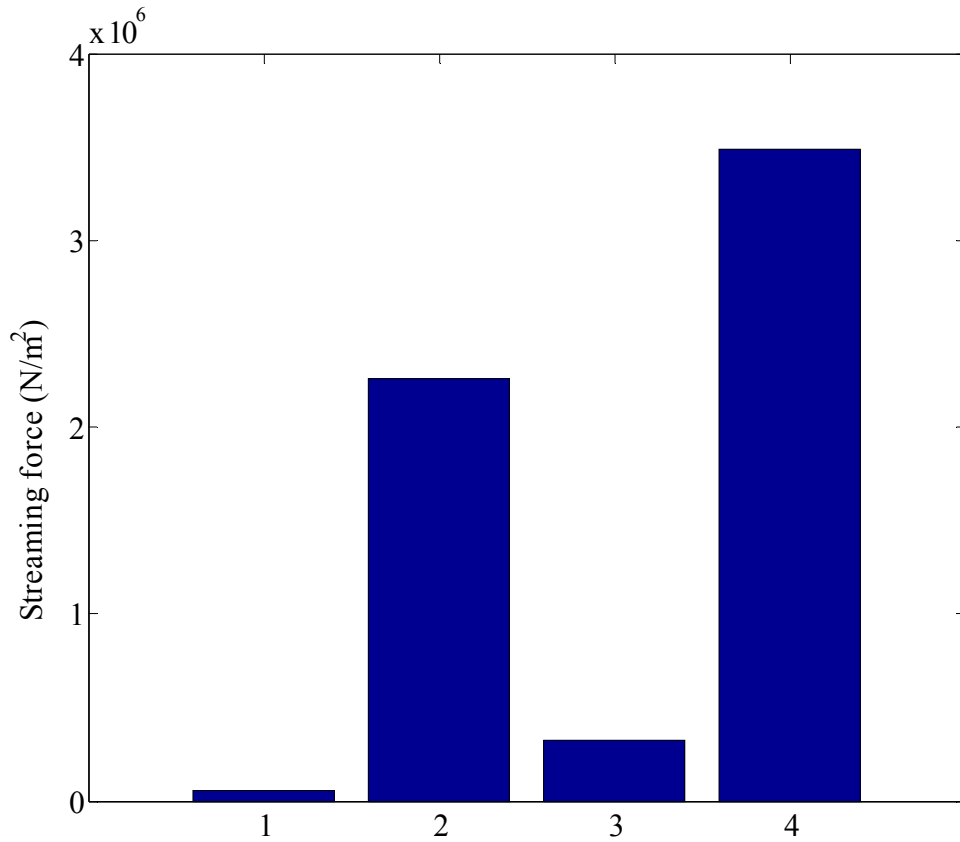


Figure 5.5: Comparison of Streaming Forces. (1) denotes standard unidirectional LGS SAW device, (2) denotes unidirectional SAW device with best case micro-cavities ($\lambda/2 \times \lambda/2 \times \lambda/2$), (3) denotes orthogonal SAW device, and (4) denotes orthogonal SAW device with micro-cavities ($\lambda/2 \times \lambda/2 \times \lambda/2$). The unidirectional propagation direction is $(0, 22, 0)$ for computing streaming force.

The increase in acoustic streaming force in the orthogonal SAW device with micro-cavities is also evident from the fluid velocity profiles obtained using 3-D FSI simulations (Figs. 5.6, 5.7, 5.8), which shows that in a micro-cavity based orthogonal SAW device, the highest fluid velocity is observed in the proximity of the micro-cavity region in the delay path thereby allowing for high biofouling removal efficiency along the entire delay path etched with micro-

cavities which is also the sensing region. It is important to note that in a standard unidirectional SAW device, the maximum fluid velocity occurs just near the input IDTs and the velocity decays in intensity on moving away from the input IDTs[110] suggesting a reduction in removal efficiency away from the IDTs. In contrast, the occurrence of highest fluid velocities near the micro-cavity region in the micro-cavity based orthogonal SAW device, as seen in Figs. 5.6 and 5.7, leads to higher streaming forces (Fig. 5.5) and therefore enhancement in acoustic streaming induced NSB protein removal along the entire delay path.

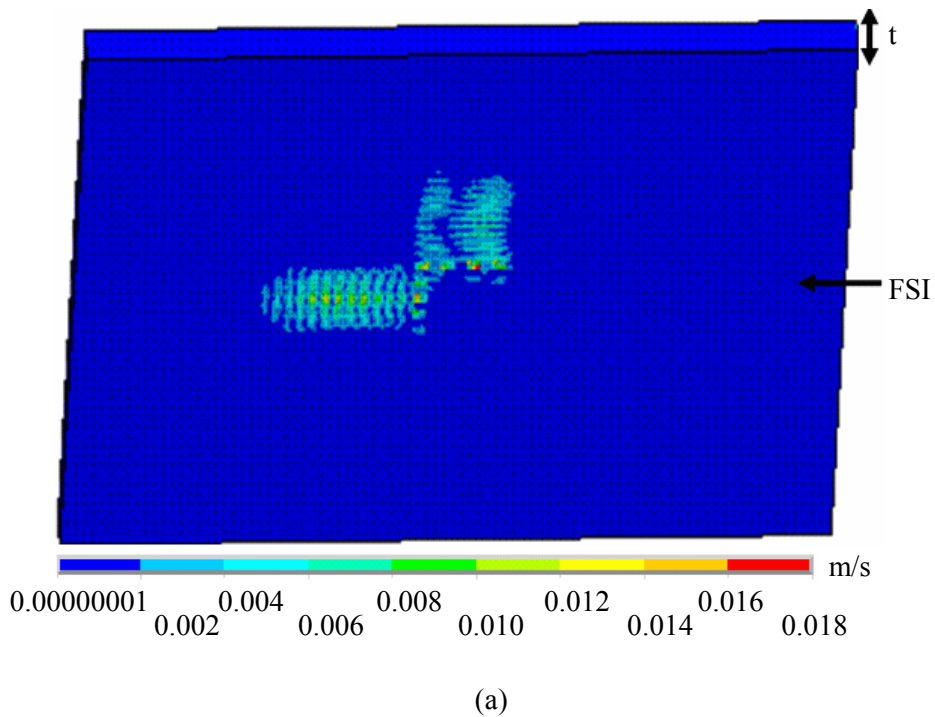
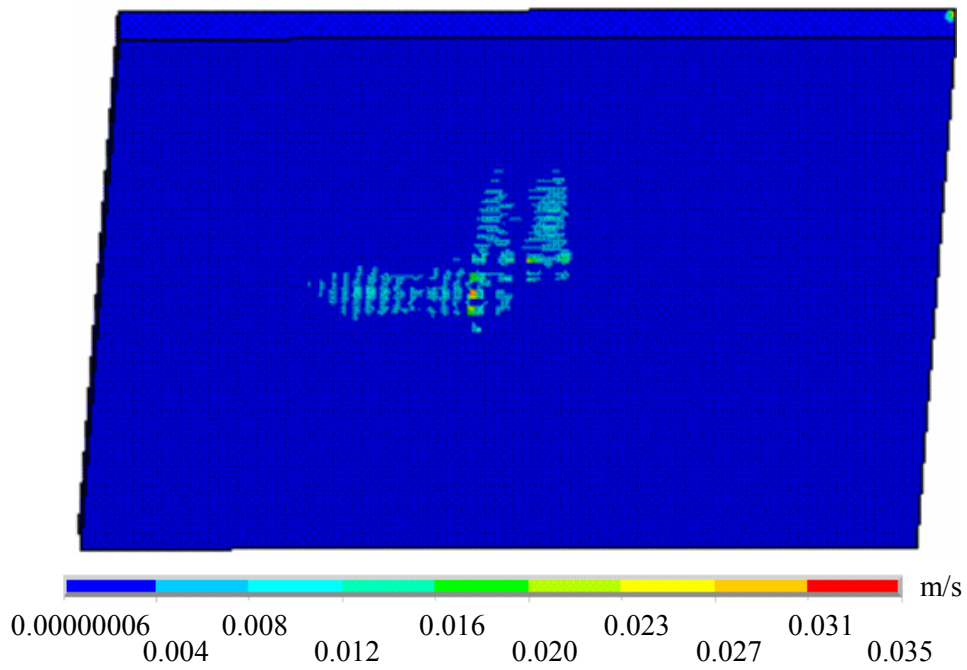
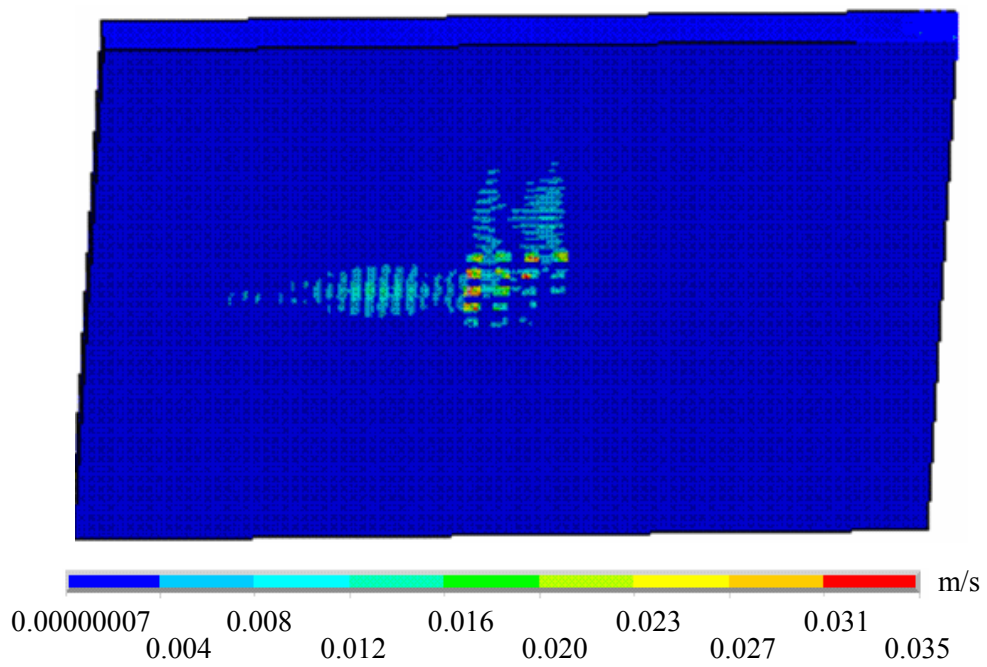


Figure 5.6: Instantaneous Fluid Velocity Contours at Various Time Instants in the Orthogonal SAW Device Having Micro-Cavities ($\lambda/2 \times \lambda/2 \times \lambda/2$) Etched in the Delay Path (a) 50 ns (b) 70 ns (c) 100 ns. Scale bar is in m/s. FSI denotes fluid-structure interface and t denotes fluid film thickness.



(b)



(c)

Figure 5.6: Continued.

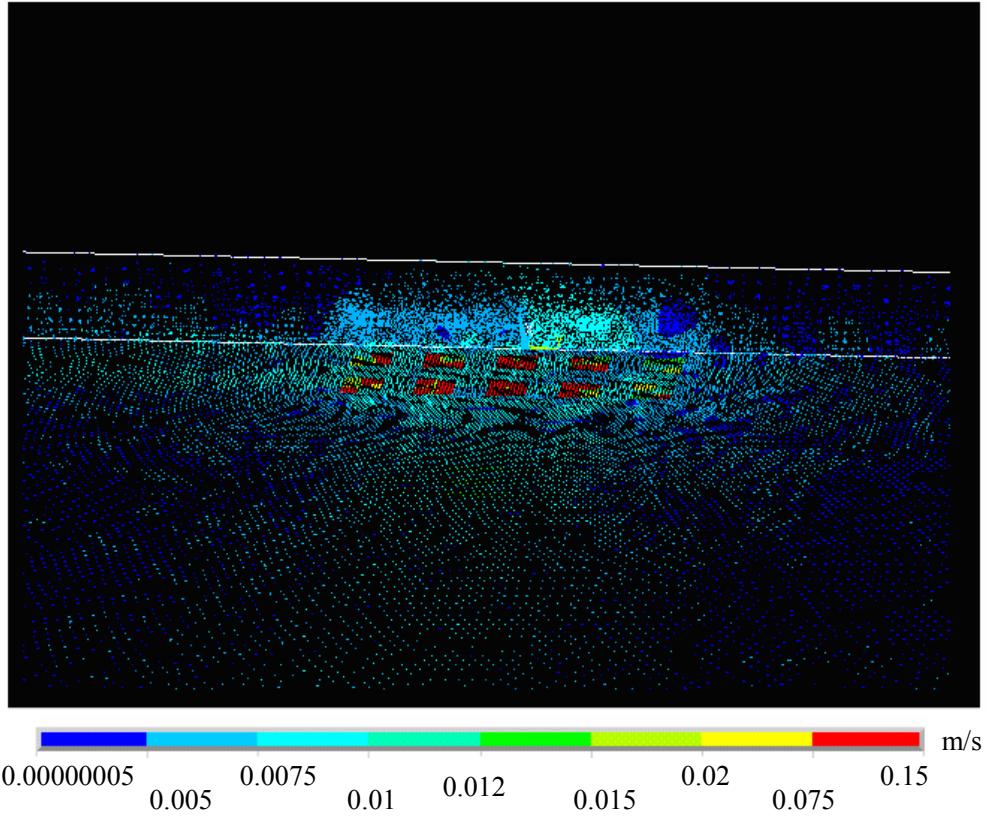


Figure 5.7: Fluid Velocity Vector for Orthogonal SAW Device With Micro-Cavities in Delay Path. A section is cut along the delay path to clearly depict the velocity vectors along the propagation length as well as fluid depth. Scale bar is in m/s.

The fluid streaming velocities along the three principal directions for the micro-cavity based orthogonal SAW device are compared with those for the standard device with unidirectional IDTs along $(0, 22, 0)$ in Fig 5.8. As clearly evident, the transverse direction tangential velocity has the largest magnitude for both cases; however the magnitude of the velocity in each of the three directions is almost two orders of magnitude higher for the micro-cavity based orthogonal device compared to the standard device.

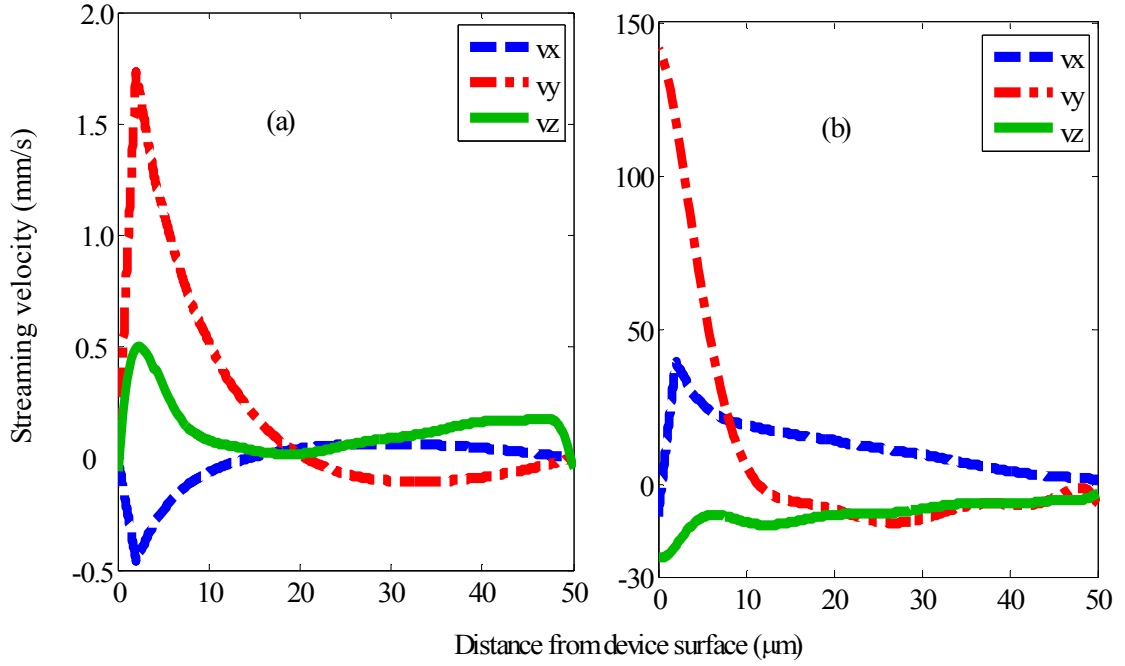


Figure 5.8: Comparison of Time Averaged Streaming Velocity Profiles in the Three Principal Directions Across the Fluid Film Thickness (a) Standard SAW device with IDTs along (0, 22, 0) and (b) Orthogonal SAW device with micro-cavities in delay path.

5.3.4 Device Sensitivity

Finally, device sensitivity was computed using the perturbation theory utilizing the mass sensitivity equation applicable to all kinds of surface acoustic devices independent of the kind of acoustic modes [143]:

$$S = -\frac{f_0 \omega^2}{4} \left(\frac{u_x^2 + u_y^2 + u_z^2}{U} \right) \quad (5-2)$$

To calculate the mass sensitivity, the values of mode center frequency f_0 , angular frequency ω , average area density of wave energy U , and displacements u_x , u_y , and u_z were derived from the

finite element simulations. Figure 5.9 compares the calculated sensitivities for orthogonal and unidirectional standard SAW devices with and without best case PS filled micro-cavities.

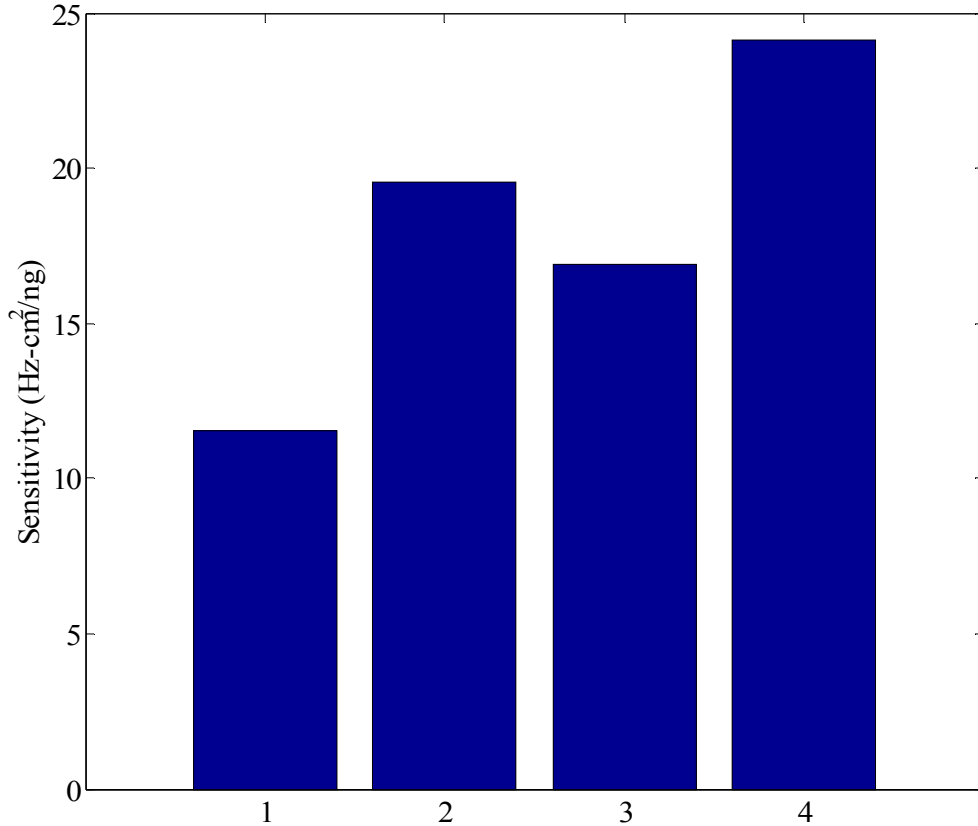


Figure 5.9: Comparison of Mass Sensitivities. (1) denotes standard unidirectional LGS SAW device, (2) denotes unidirectional SAW device with best case micro-cavities ($\lambda/2 \times \lambda/2 \times \lambda/2$), (3) denotes orthogonal SAW device, and (4) denotes orthogonal SAW device with micro-cavities ($\lambda/2 \times \lambda/2 \times \lambda/2$). The unidirectional propagation direction is (0, 22, 90) for computing mass sensitivity.

The finite element analysis shows a clear correlation of surface perturbations with sensitivity. As wave displacements increase due to constructive interference, the surface mass sensitivity value calculated using Eq. (5-2) and shown in Fig. 5.9 also increases. In addition, the use of micro-cavities in the delay path leads to an enhanced entrapment of acoustic energy near

the surface, leading to maximum displacements in the micro-cavity region, as clearly seen in the displacement contours (Fig. 5.3). This integrated effect of constructive wave interference due to orthogonally mutually interacting acoustic waves and acoustic energy confinement in micro-cavities leads to maximized energy entrapment and displacements on the surface, thereby imparting the highest sensitivity of 24.15 Hz-cm²/ng to orthogonal SAW devices with PS filled micro-cavities. This design reflects more than 100% increase in sensitivity over that of a standard SAW device (11.56 Hz-cm²/ng). Together with the capability to simultaneously eliminate biofouling at the highest possible efficiency amongst the investigated designs, the SAW device with combined delay-path and transducer modifications marks a significant improvement over the standard SAW biosensor with unidirectional IDTs and no delay path modifications.

5.4 Conclusion

In summary, the effects arising from mutually interacting transducers and delay path modifications in the form of micro-cavities, on SAW sensors fabricated in LGS, have been evaluated using FE simulations. This work reveals that phase difference between the orthogonally propagating waves in LGS allows for constructive acoustic wave interference in mutually interacting, multidirectional IDTs leading to decreased power loss. Furthermore, the results indicate that the enhanced acoustic energy entrapment through the incorporation of sensor surface modifications such as PS-filled micro-cavities in the orthogonal SAW device results in dramatically increased transmitted acoustic energy, further reducing the power consumption. Compared to a standard LGS-based SAW device, a configuration with integrated multidirectional IDTs and PS-filled micro-cavities in the delay path provides advantages of significantly increased sensor sensitivity and much higher streaming induced non-specifically bound protein removal efficiency to overcome biofouling. The improved SAW device design has tremendous significance and implications in the areas of biosensing and microfluidic applications.

Chapter 6

Enhancement of Acoustic Streaming Induced Flow on a Focused SAW Device: Implications for Biosensing and Micro-fluidics

Fluid motion induced on the surface of 100 MHz focused surface acoustic wave (F-SAW) devices with concentric inter-digital transducers (IDTs) based on YZ LiNbO₃ substrate was investigated using three dimensional bi-directionally coupled finite element fluid-structure interaction models. Acoustic streaming velocity fields and induced forces for the F-SAW device are compared with a conventional SAW device with uniform IDTs. The velocity vector streamlines indicate recirculation patterns which differ between the conventional and F-SAW devices. While the conventional SAW shows maximum fluid recirculation near input IDTs, the region of maximum recirculation is concentrated near the focal point of the F-SAW device. The current simulation results indicate acoustic energy focusing by the F-SAW device leading to maximized device surface displacements, fluid velocity, and streaming forces near the focal point located in the center of the delay path, in contrast to the conventional SAW exhibiting maximized values of these parameters near the input IDTs. Significant enhancement in acoustic streaming is observed in the F-SAW device when compared to the conventional ones; the increase in streaming velocities was computed to be 352% and 216% for tangential velocities in propagation and transverse directions, respectively, and 353% for the normal velocity. Consequently, the induced streaming force for F-SAW is 480% higher than conventional SAW. In biosensing applications, this allows for the removal of smaller sub-micron sized particles by F-SAW which are otherwise difficult to remove using the conventional SAW; the F-SAW presents an order of

magnitude reduction in the smallest removable particle size compared to the conventional device. Thus, the results from the present study indicate that the acoustic energy focusing and acoustic streaming enhancement brought about by the F-SAW device manifests itself as enhanced biofouling efficiency of F-SAW throughout the device delay path compared to the conventional device, thereby providing enhanced device sensitivity, selectivity and permitting device reuse. The results of this work are shown to have significant implications in biosensing and microfluidic applications. In a broader context, the results of the present study demonstrate a technique of enhancing streaming induced flows, which is of great importance to contemporary problems involving microfluidic and sensing applications of piezoelectric devices.

6.1 Introduction

Surface acoustic wave (SAW) sensors find intensive applications in chemical and biological sensing owing to their portability, cost effectiveness, high sensitivity, and reliability [43, 46-52]. Typically, biosensing applications require the detection and measurement of biomarkers in fluid media [54]; such as the measurement of certain proteins in bodily fluids for the detection of pathologies. The use of SAW sensors in biosensing applications requires the integration of SAW devices with microfluidics [144], which is the science of designing systems and processes that handle and use fluid volumes of the order of picoliters to nanoliters thereby reducing the dead volume in the system. Some applications of microfluidics include gene expression analysis using DNA chips, DNA hybridization, lab-on-chip systems, immuno-assays, micro-arrays, biosensing, drug screening, drug delivery, ultrasonic mixing, actuation, and flow cytometry to name a few [3-10]. In microfluidic applications, the performance of the SAW device is influenced by its ability to generate high enough velocities in a small volume [145] which can be achieved through high frequency acoustic waves generated in these devices. SAW devices can

also be used as actuators for pumping small volumes of fluid to generate high enough velocities in the small fluidic channels owing to the high intensity acoustic waves.

Most of the clinical and diagnostic biosensing applications of SAW devices require transduction of picogram to nanogram level of biomarkers into a readable signal without interference from other proteins and biomarkers, thereby requiring high device sensitivity and selectivity. However, most of the biosensors are plagued with the issue of non-specific protein binding to the device surface [99, 110, 131, 146] which interfere with the sensing phenomenon and leads to a reduction in the device sensitivity, selectivity, and analyte discrimination capabilities. Thus, non-specifically bound (NSB) protein removal remains a challenge in biosensing applications. Additionally, high device sensitivity is required so as to detect small enough concentrations of the analyte. Acoustic streaming, which refers to fluid motion induced by high intensity sound waves, can be used to eliminate non-specifically bound (NSB) proteins from the SAW surface [110]. When Rayleigh waves with a prominent surface normal component propagate in a SAW device, they couple strongly with the fluid in contact with the device and leak energy into the fluid domain leading to conversion from Rayleigh to leaky SAW, which results in the propagation of longitudinal waves in the fluid domain. This SAW-fluid interaction creates a pressure gradient in the direction of acoustic wave propagation in the fluid, inducing fluid flow and leading to an acoustically driven streaming phenomenon known as SAW streaming [74, 75] which can facilitate the removal of loosely bound non-specific proteins as demonstrated through recent experimental investigations in our laboratory [99, 101] and consequently improve sensor selectivity and sensitivity. The interplay of SAW body force and the acoustic streaming induced fluid forces with the adhesive force plays a critical role in NSB removal. While the acoustically induced tangential fluid motion exerts viscous stresses at the interface boundary causing fluid recirculation and particle advection, the normal motion exerts a lift force on the particles preventing particle re-attachment to the device surface [110, 139, 147] which are

detached from the surface when the SAW body force overwhelms the adhesive van der Waal's force between the particle and the device surface. Thus, streaming induced flows on device surface can play a significant role in biosensing applications.

Enhancement of ultrasonic micro transport via acoustic streaming through the design and use of novel device and transducer configurations has received considerable attention in recent years [145]. Typically in a conventional SAW device with uniform finger IDTs (henceforth referred to as conventional SAW), the SAW displacement field and consequently the streaming force decay rapidly on moving away from the input IDTs in the sensing region. This aspect severely limits the application of conventional SAW devices in biosensing applications. One of the critical issues in this regard is the generation of sufficiently high acoustic streaming velocities and streaming force along the entire SAW delay path, which in turn requires the generation of strong SAW fields in the region being probed. The latter can be realized through the generation of focused beam using specialized IDT designs [148]. Experimental and theoretical investigations have revealed that focused interdigital transducers (F-IDTs), based on concentric wave surfaces, can excite waves with high intensity, high beam-width compression ratio, and small localized area. [149-152]. These high intensity excited waves can be utilized to enhance the streaming induced removal of fouling proteins leading to highly sensitive biosensors.

The efficient utilization of acoustic streaming in SAW devices requires the understanding of wave propagation and fluid dynamics as well as the interaction of acoustic waves with the fluid domain in these systems. Previous attempts to address this have utilized simplified analytical models treating the leaky wave as a first-order perturbation on the non-leaky wave associated with surface-wave propagation and numerical models in conjunction with perturbation theory derived parameters to predict streaming velocities and forces based on the continuum model of Nyborg [14, 103, 110, 122]. However, these models ignore the effect of liquid loading and viscous dissipation in the presence of the same, owing to simplification of the Navier-Stokes

equation. A comprehensive understanding of the SAW-fluid interaction and the effectiveness of complex IDT configurations such as F-IDTs in acoustic streaming enhancement requires the development of fully coupled three dimensional (3-D) finite element (FE) fluid structure interaction (FSI) models. These models would be instrumental in investigating methods to increase the acoustic streaming velocity for NSB protein removal while minimizing the influence of the streaming force on the sensing layer, thereby increasing the sensitivity and selectivity.

In the present work, a 3-D FE FSI model has been developed to investigate and analyze the streaming velocity fields and forces induced by SAW devices with F-IDTs based on concentric wave surfaces. Using the developed 3-D FSI model, the acoustic streaming enhancement brought about by the F-SAW device is analyzed by comparison with a conventional SAW device having uniform IDTs. Till date, there have been no three dimensional fluid structure interaction studies on the streaming induced by F-SAW devices which can quantitatively give an estimate of the streaming velocity variations introduced by viscous effects.

6.2 Computational Details

This section discusses the FSI model and the associated theory to investigate acoustic streaming and compute streaming velocities in the SAW device in contact with fluid domain.

6.2.1 Theory

A coupled-field FSI model of a piezoelectric device in contact with a liquid loading requires the solution of the piezoelectric constitutive equations in conjunction with the fluid dynamical equations. A system of four coupled wave equations for the electric potential and the three component of displacement in piezoelectric materials are solved for the piezoelectric substrate[34].

$$-\rho \frac{\partial^2 u_i}{\partial t^2} + c_{ijkl}^E \frac{\partial^2 u_k}{\partial x_j \partial x_l} + e_{kij} \frac{\partial^2 \phi}{\partial x_k \partial x_j} = 0 \quad (6-1)$$

$$e_{ikl} \frac{\partial^2 u_k}{\partial x_l \partial x_l} - \varepsilon_{ik}^s \frac{\partial^2 \phi}{\partial x_l \partial x_k} = 0 \quad (6-2)$$

c, e, and ε represent structural elasticity matrix at constant electric field, piezoelectric stress matrix, and dielectric matrix at constant mechanical strain, respectively and ϕ denotes the electric potential. These coupled wave equations are discretized and solved to obtain voltage and displacement profiles at each element/node.

The fluid domain is modeled as incompressible and Newtonian, using the Navier-Stokes in conjunction with the continuity equation.

$$\rho \left(\frac{\partial v_f}{\partial t} \right) + v_f \cdot \nabla v_f + \nabla P - 2\eta \nabla \cdot D = 0 \quad (6-3)$$

$$\nabla \cdot v_f = 0 \quad (6-4)$$

Here, v_f , P , ρ and η denote the fluid velocity, pressure, density, and viscosity, respectively. D is the rate of deformation tensor given by

$$D = \frac{1}{2} (\nabla v_f + (\nabla v_f)^t) \quad (6-5)$$

Whereas a Lagrangian frame is used for discretization of the structural domain, the fluid domain can be discretized using either Eulerian or Lagrangian frame of reference. However, a purely Lagrangian frame, in which the mesh moves with the velocity of the fluid, is not suitable for dealing with large deformations of the fluid mesh arising from the non-cohesive nature of fluid particles which causes them to travel independently and diverge in space. On the other hand, a purely Eulerian frame for the fluid domain in which the mesh is fixed, is unable to track the path of the elements. Therefore, Arbitrary-Lagrangian-Eulerian (ALE) methods, which combine the best of the both frames of reference, are used for discretization of the fluid domain in such

problems [120, 121]. In ALE method, an Eulerian frame is used for regions with significant fluid motion such that a deformable mesh could undergo excessive distortion and the Lagrangian frame is used for regions of negligible flows; the equation of motion for the fluid domain can be written as follows

$$\rho \left(\frac{\partial v_f}{\partial t} \right) + (v_f - w) \cdot \nabla v_f + \nabla P - 2\eta \nabla \cdot D = 0; \quad (6-6)$$

where w is the grid velocity such that $w \neq v_f \neq 0$

The fluid-solid coupling is established by maintaining stress and displacement continuity at the fluid-structure interface. These conditions translate to no-slip for the fluid domain (velocity continuity) and stress continuity for solid domain, given by

$$v_f = v_s = \frac{\partial u}{\partial t} \quad (6-7)$$

$$\sigma_{ij}^s n_j^s + \sigma_{ij}^f n_j^f = 0 \quad (6-8)$$

n_j is the instantaneous outward normal at the fluid-structure interface, i denotes longitudinal direction. Superscripts f and s denote fluid and structural domain, respectively and u denotes displacement of the piezoelectric domain. The fluid mesh is updated with the distortion of the structural domain.

The velocity v calculated from Equations (6-4) through (6-8) contains harmonically varying terms and a “dc” term. The latter induces acoustic-streaming. When averaged over a relatively long time, the effect of the harmonically varying terms disappears and only the contributions from the dc part appear in the solution, producing a time invariant mean flow. The acoustic-streaming velocity ($\bar{v}_{a,i}$, $i=x, y, \text{ and } z$) is therefore obtained by averaging v over a time period as follows:

$$\bar{v}_{a,i} = \frac{1}{T} \int_0^T v_i dt, \quad i=x, y \text{ and } z \quad (6-9)$$

where T is the time period of the wave propagation.

6.2.2 Model Details

A 3-D coupled field FSI model of a SAW device based on YZ-LiNbO₃ with a liquid loading was developed to gain insights into the acoustic streaming phenomenon. A piezoelectric substrate, with dimensions 400μm width x 800μm propagation length x 200μm depth and in contact with a 50 μm thick fluid film, was modeled to investigate acoustic streaming in the SAW device (Fig. 6.1a). Two sets of IDTs were defined: the input IDTs and the output IDTs with three IDT finger pairs on the surface in each port. The focused SAW (F-SAW) device was constructed by adopting a pair of concentrically shaped F-IDTs as shown in Fig. 6.1b.

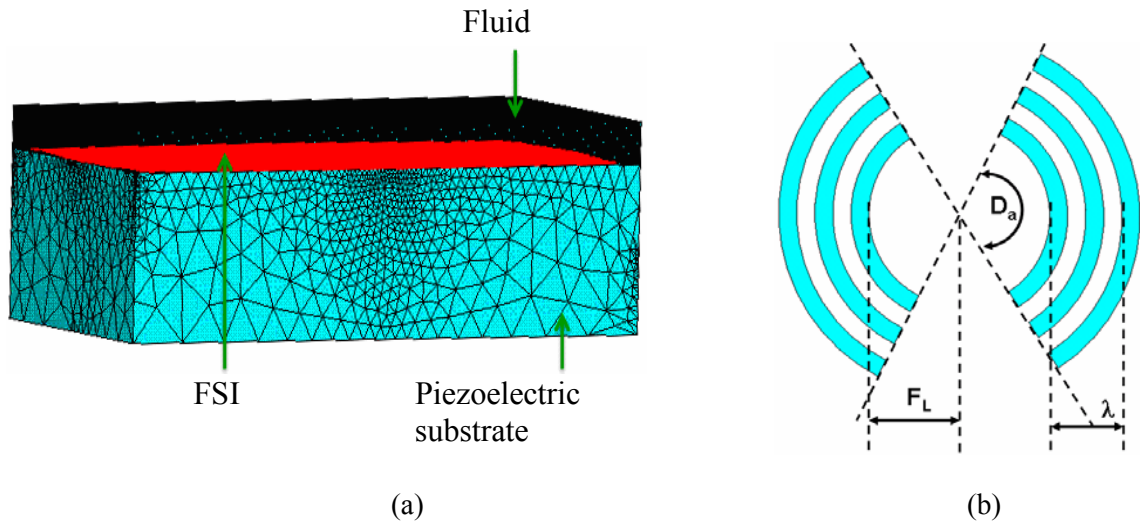
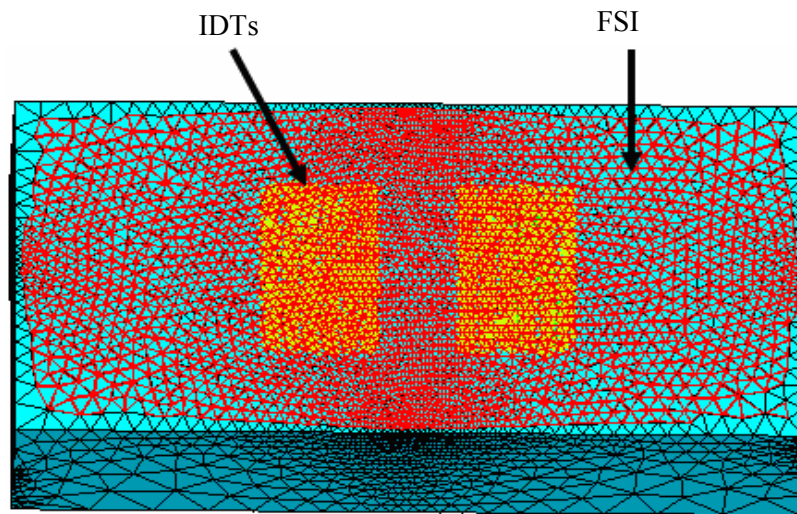


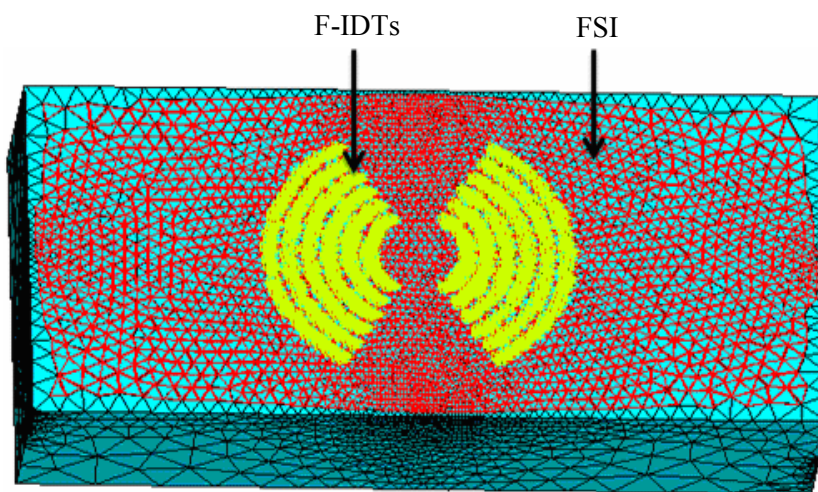
Figure 6.1: (a) Meshed Fluid-Structure Interaction Model of the Surface Acoustic Wave Device in Contact With the Fluid Domain. (b) Schematic Showing Focused Interdigital Transducers in a Focused SAW Device. FSI denotes fluid-structure interface. D_a , F_L , and λ denote angle of arc, focal length, and wavelength, respectively.

The IDT fingers were represented by a set of nodes coupled by voltage degrees of freedom (DOF). The piezoelectric domain was meshed with tetragonal solid elements with four degrees of freedom, namely the three translations and the voltage. The fluid domain was meshed using eight node fluid elements and discretized employing an Arbitrary Lagrangian Eulerian (ALE) frame for the kinematical description. To optimize on the computation time while capturing the interface dynamics accurately, the mesh density was such that it was refined near the fluid-structure interface and coarser away from it. A total of 2, 218, 399 nodes and 2, 085, 877 elements were generated.

To achieve bidirectional fluid structure coupling, stress and displacement continuity were maintained across the fluid-structure interface. To achieve this, displacements were transferred from solid to fluid and pressure from fluid to solid across the interface. The fluid mesh was continuously updated as the piezoelectric substrate undergoes deformation. Numerical solution was obtained by solving the governing equations for the two domains using the iterative sequential coupling algorithm: the Navier-Stoke's equation for fluid and acoustoelectric equations for the piezoelectric domain [110, 133]. In this algorithm, the governing equations for the two domains are solved separately and the solver iteration between the two domains continues till convergence of the load transferred across the interface is achieved. Structural simulations were carried out for different F-IDT designs having varying degree of arc, focal length, and wavelength. The F-IDT design that provides the maximum streaming force and least insertion loss was used in the FSI simulation to investigate acoustic streaming in F-SAW device. The enhancement in F-SAW induced acoustic streaming velocity was computed by comparison with a conventional SAW device having finger IDTs defined with a periodicity of 40 μm and aperture width of 200 μm . The meshed structures for the conventional and F-SAW device are shown in Figures 6.2(a, b).



(a)



(b)

Figure 6.2: Meshed Structures of the Simulated SAW Devices With IDTs (a) Uniform IDTs (b) Focused IDTs (F-IDTs). FSI denotes fluid-structure interface.

The central frequency of the device was computed to be 100 MHz using an impulse response analysis. To investigate acoustic streaming, the acoustic excitation of the device was

induced by applying an input AC voltage with a peak of 2.5 V and a frequency of 100 MHz (Fig. 6.3).

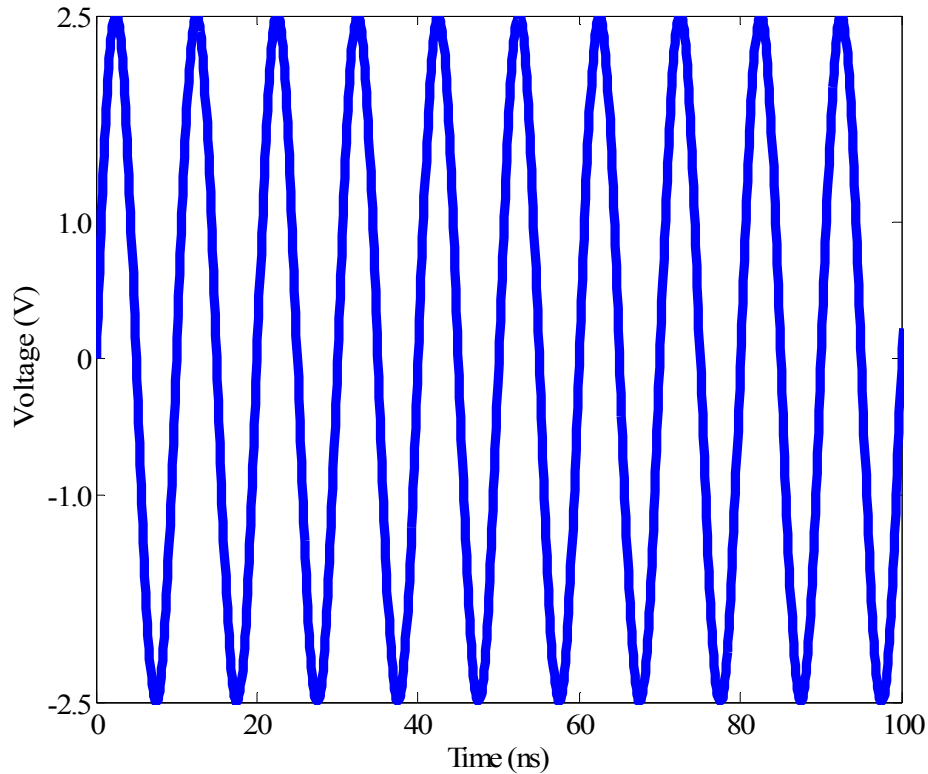


Figure 6.3: AC Voltage for Structure Excitation Applied to Input IDTs.

6.3 Results and Discussion

Structural simulations have been carried out previously [14] for various F-IDT configurations with varying degree of arc (D_a), focal length (F_L), and wavelength (λ) to estimate the magnitude of insertion loss and SAW displacements for various device designs and identify the best F-IDT configuration that can lead to enhanced acoustic streaming. The results for various device designs are summarized in Table 6.1 below.

Table 6.1: Summary of Various F-SAW Designs Simulated [14].

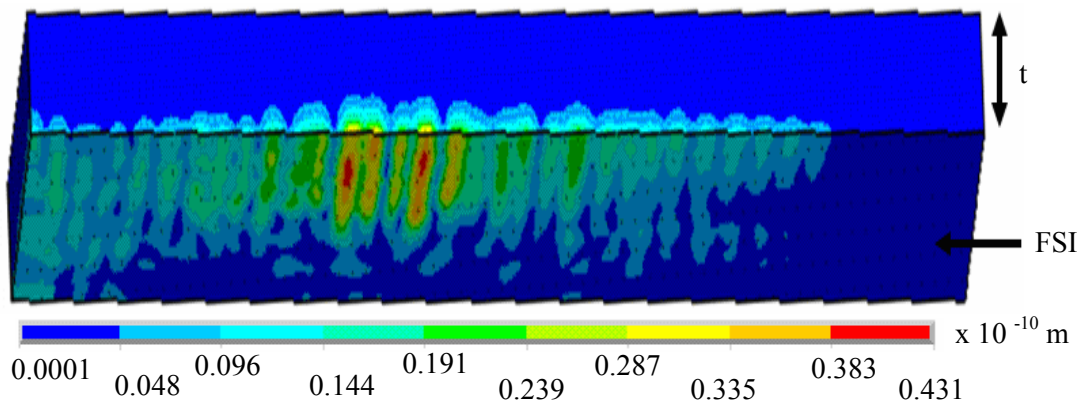
	Geometric Focal length (μm)	Degree of arc D_a	Wavelength (μm)	Insertion loss (dB)	Normalized displacement (λ)
1	45	120°	40	-9.5	1.16
2	45	120°	60	-11.6	0.75
3	45	120°	80	-11.9	0.60
4	45	90°	40	-8.6	1.03
5	45	60°	40	-3.8	0.96

It can be seen that minimum insertion loss corresponds to design 5. However, for microfluidic actuation and sensing applications involving biofouling elimination which requires enhanced streaming, insertion loss is not the most critical criteria. It is more important to have higher amplitudes of SAW displacement, which can in turn lead to higher induced SAW streaming. When the device displacement amplitude are analyzed, the device with periodicity/wavelength of 40 μm , geometric focal length of 45 μm and degree of arc (D_a) 120° provides the best design. This design configuration was utilized in FSI simulations to study fluid flow profiles and streaming velocity fields generated in SAW devices involving focused IDTs. The aperture width of the fingers varied depending on their radial distance from device center.

6.3.1 SAW Fluid Interaction

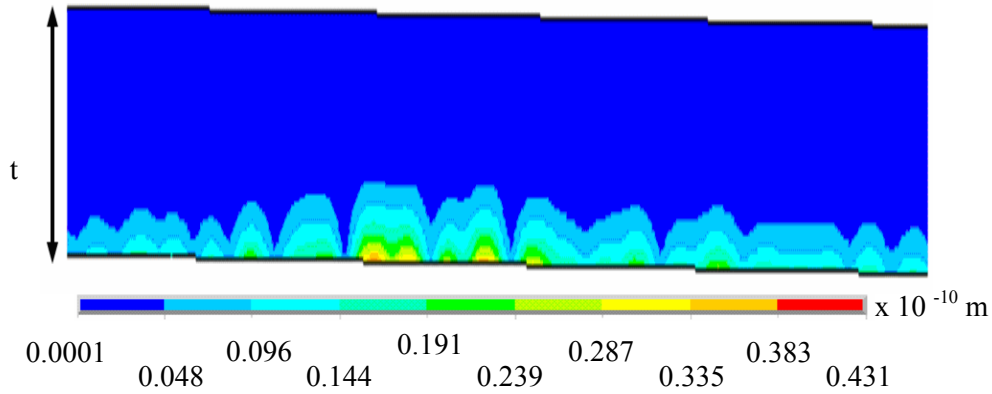
The SAW device with a propagating Rayleigh wave couples strongly and leaks acoustic energy into the fluid, leading to a mode conversion from Rayleigh to leaky SAW (Figures 6.4, 6.6b). The leaky SAW decays with distance from the input IDTs (Fig. 6.4). This mode conversion eventually generates a pressure gradient in the direction of acoustic wave propagation in the fluid,

leading to an acoustically driven phenomenon known as acoustic streaming. The highest fluid displacements and velocities are obtained close to the device surface beyond which significant damping of fluid motion is observed. The fluid is characterized by velocities the order of 20 mm/s in the 50 μm thick fluid film, in accordance with the reported experimental values [3], yielding a Reynolds number of 0.8 suggesting that the flow is completely laminar. Flow reversal leading to recirculation is obtained close to the device surface, which can lead to eddy formation. This fluid motion and recirculation facilitates particle transport via advection and lift, attributable to the generation of various hydrodynamic forces.



(a)

Figure 6.4: (a) Simulated Fluid Displacement Profile for the Conventional SAW Device (b) Simulated Fluid Displacement on a Section Cut Through the Device Center Across the Fluid Film Thickness Along the Propagation Length in the Conventional Saw Device. The figure is enlarged near the IDT region. The decay of the fluid motion on moving away from the IDTs can be clearly seen. Scale bar is in meters. FSI denotes fluid-structure interface. ‘t’ denotes fluid film thickness.



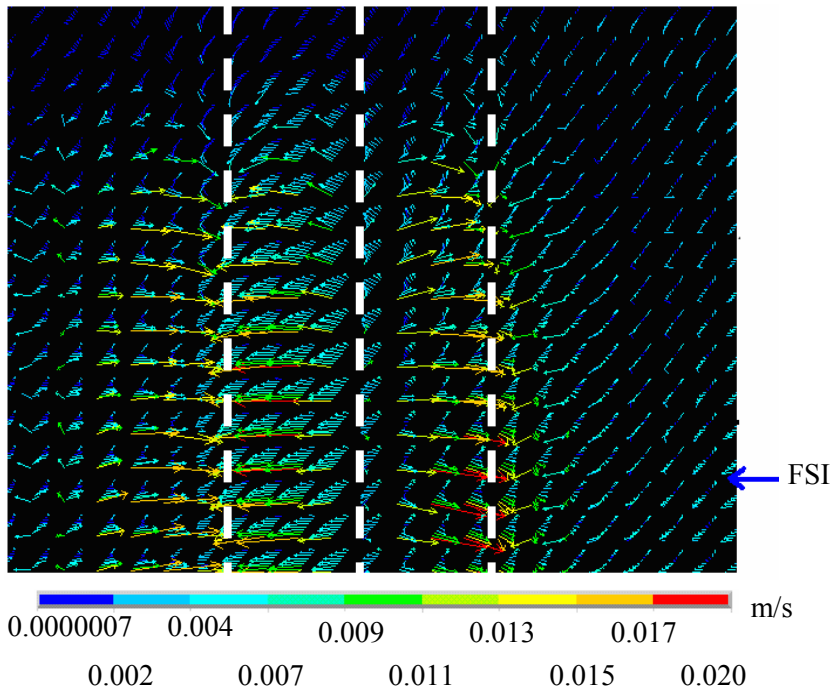
(b)

Figure 6.4: Continued.

6.3.2 Fluid Flow Fields and Substrate Displacement Profiles

The fluid velocity vector along the fluid-device interface, zoomed in close to the IDT regions, for the conventional and F-SAW device are shown in Fig. 6.5. The streamlines of the vector field are representative of the trajectory of particles advected by the fluid. The fluid vector streamlines in the conventional device indicate recirculation leading to eddy formation between the IDTs. Since the flow is mainly laminar, this eddy formation near the IDTs may be attributable to the impedance to fluid flow between two successive crests formed between two successive IDT fingers. When fluid flows through these wave crests that result from the alternating motion of the IDTs, it experiences frictional resistance. As the flow circumvents these crests, the viscous effect drives a counter-circulation leading to eddy formation. In the conventional device, the extent of recirculation and hence eddy formation is reduced away from the IDTs. In contrast, the IDTs focus the fluid flow near the device focal point in the F-SAW device, thereby increasing the intensity of recirculation and therefore eddy formation in the region near the focal point (Fig. 6.5b). With time, these eddies rise from the device surface and break into smaller ones, while new ones are formed at the surface. These eddies play a role in particle advection. It is worth mentioning that the operating conditions can be chosen obtain an increased intensity of acoustic

actuation due to focusing effect, which can be utilized for various microfluidic applications like micro-dispensing to pico-dispensing.



(a)

Figure 6.5: Simulated Fluid Velocity Vectors for the Conventional and Focused SAW Device. (a) Fluid velocity vectors zoomed in near the IDT region for the conventional SAW device. The dotted white lines indicate IDT fingers. Fluid recirculation near the IDTs is clearly shown. (b) Fluid velocity vectors (zoomed in) at the fluid surface in contact with the focused SAW device. The recirculation near the device focal point in the delay path is clearly shown. Fluid layer at the interface is depicted and the direction of viewing is normal to the fluid-structure interface. Scale bar is in m/s.

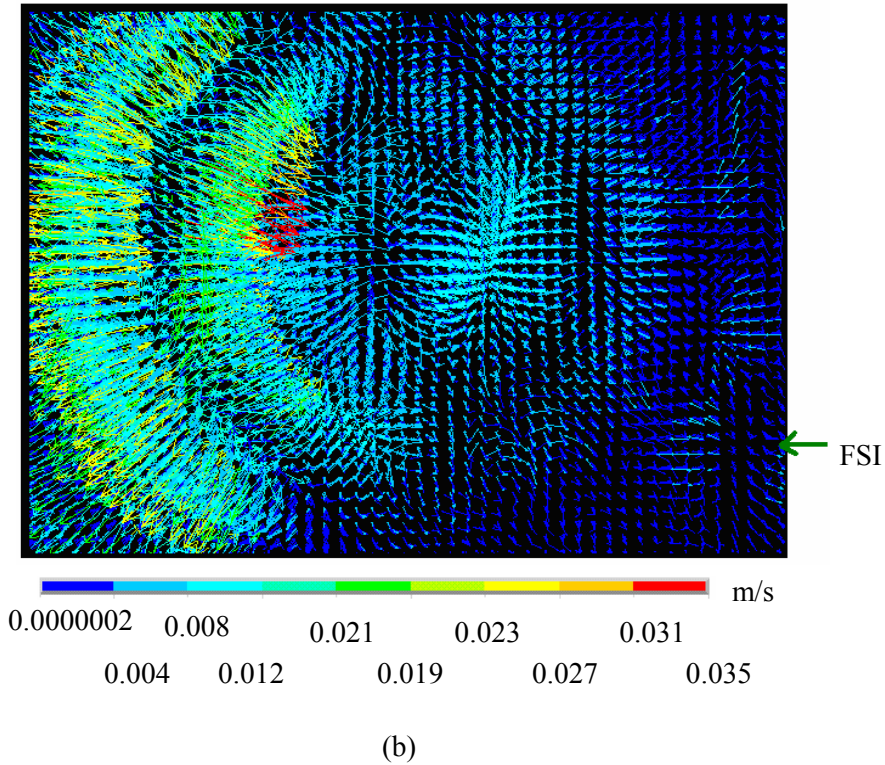
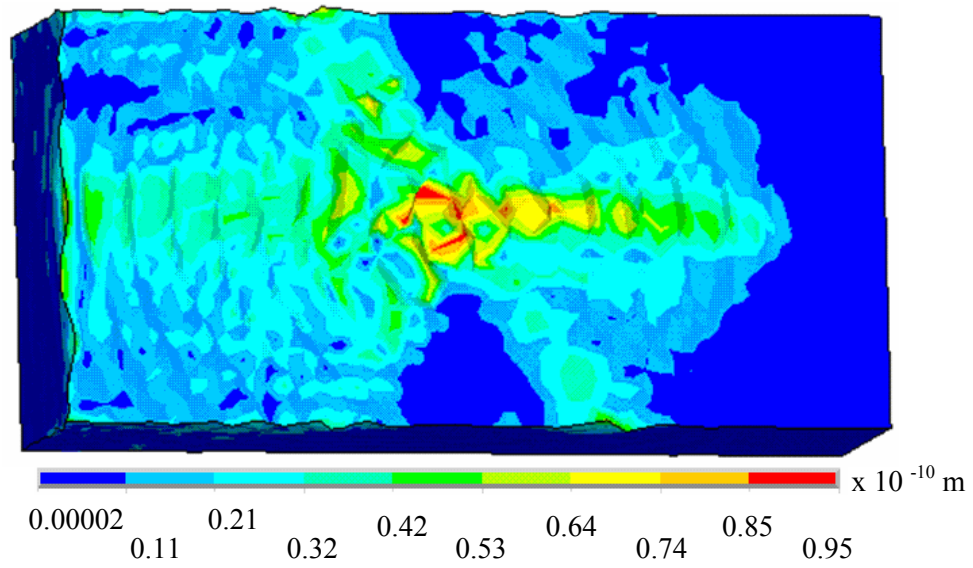


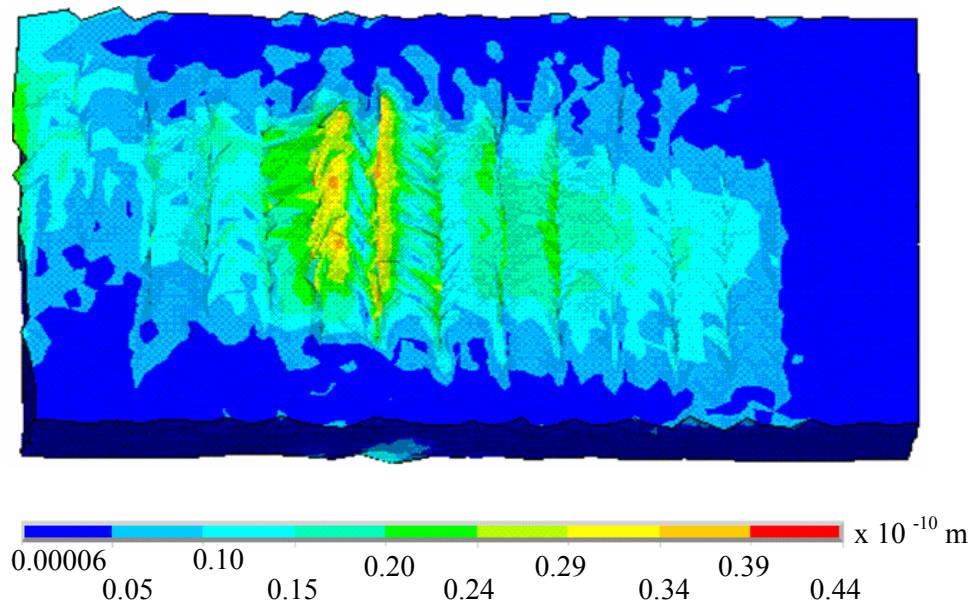
Figure 6.5: Continued.

As the piezoelectric device is excited, surface displacements are generated leading to the propagation of a wave through the piezoelectric substrate. A comparison of the simulated device displacement profiles reveals an increase in the surface displacements of a F-SAW device compared to a conventional SAW device with a similar size, finger periodicity and applied input voltage (Figs. 6.6, 6.7), consequently leading to an enhancement in the induced acoustic streaming. Further, the F-SAW device leads to the acoustic energy focusing leading to maximized displacements near the focal point in the center of the delay path, in contrast to the conventional SAW device in which the displacements are maximum near the input IDTs and decay rapidly on moving away from them (Fig. 6.7). The increased and localized surface displacements of the F-SAW device eventually lead to enhanced acoustic streaming thereby making the F-SAW device

more suitable for microfluidic applications, such as biofouling elimination in biosensing, compared to the conventional SAW.



(a)



(b)

Figure 6.6: Simulated Piezoelectric Device Displacement Contours (a) Focused SAW device (b) Conventional SAW device with uniform IDTs. Scale bar is in meters.

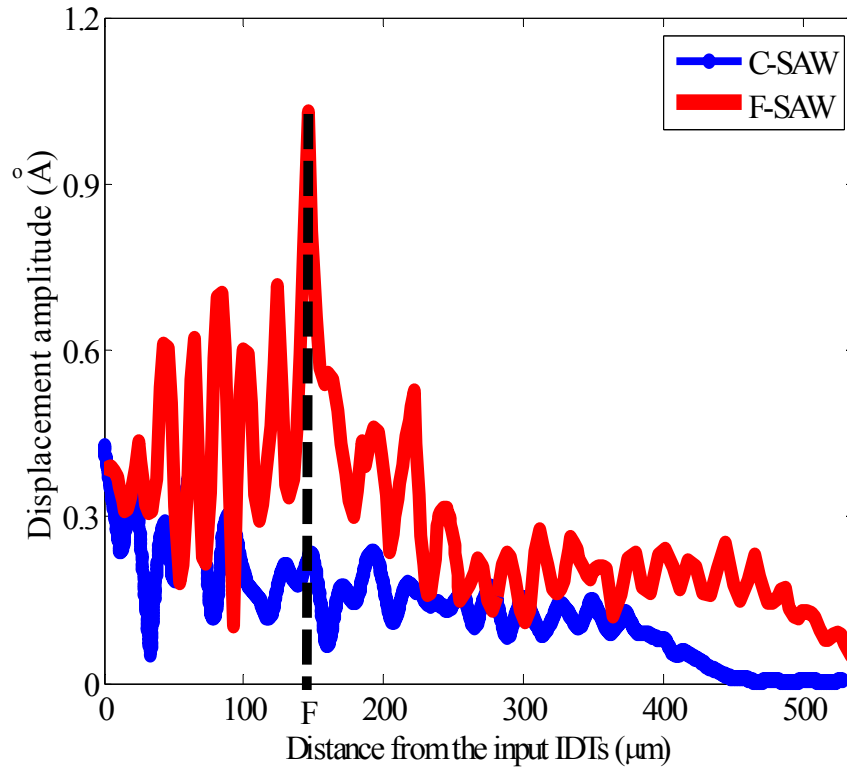
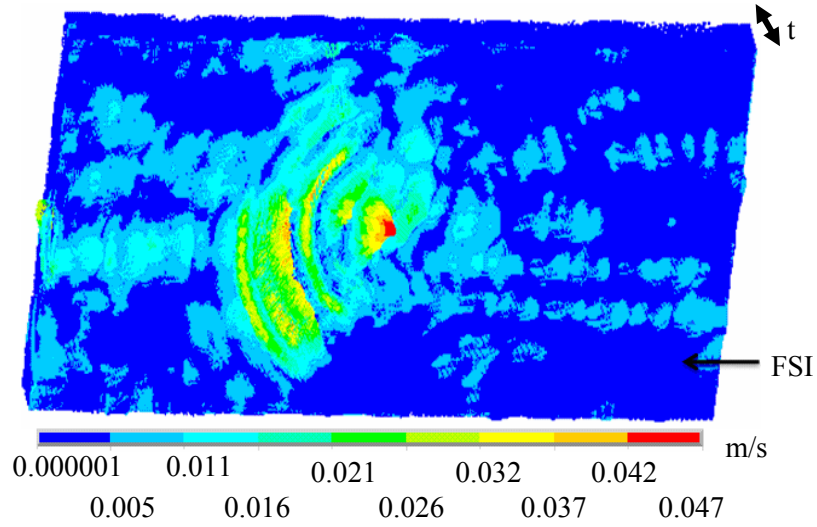
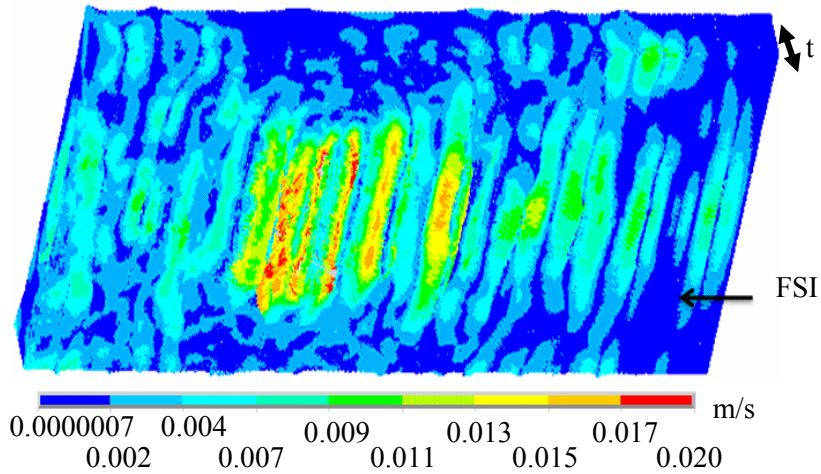


Figure 6.7: Comparison of Particle Displacement on the Device Surface Along the Propagation Length for Focused SAW (F-SAW) vs. Conventional SAW (C-SAW) Device Having Uniform IDTs for a Peak Input AC Voltage of 2.5 V.

The fluid velocity vectors for the conventional and F-SAW device, shown in Fig. 6.8, indicate that the F-SAW device generates higher velocities in the fluid domain in contact with the device as compared to the conventional SAW. For the current configuration, the F-SAW device generated fluid velocity is almost double the velocity generated by the conventional device. Further, owing to the acoustic energy focusing in the F-SAW device leading to peak displacements near the focal point (Fig. 6.7), the highest fluid velocities are generated near the focal point in the F-SAW device whereas in the conventional SAW, the fluid velocity peaks near the input IDTs (Fig. 6.8).



(a)



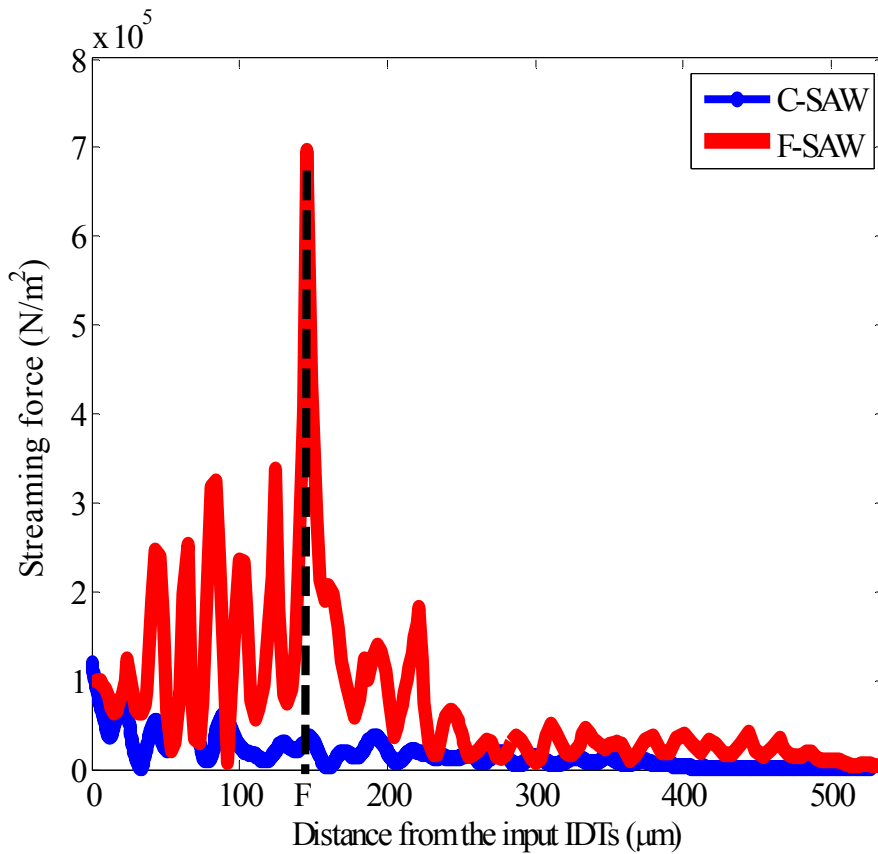
(b)

Figure 6.8: Simulated Fluid Velocity Profiles (a) Focused SAW device (b) Conventional SAW device with uniform IDTs. Scale bar is in m/s. t denotes fluid film thickness, FSI denotes fluid-structure interface.

6.3.3 Acoustic Streaming Velocity and Force

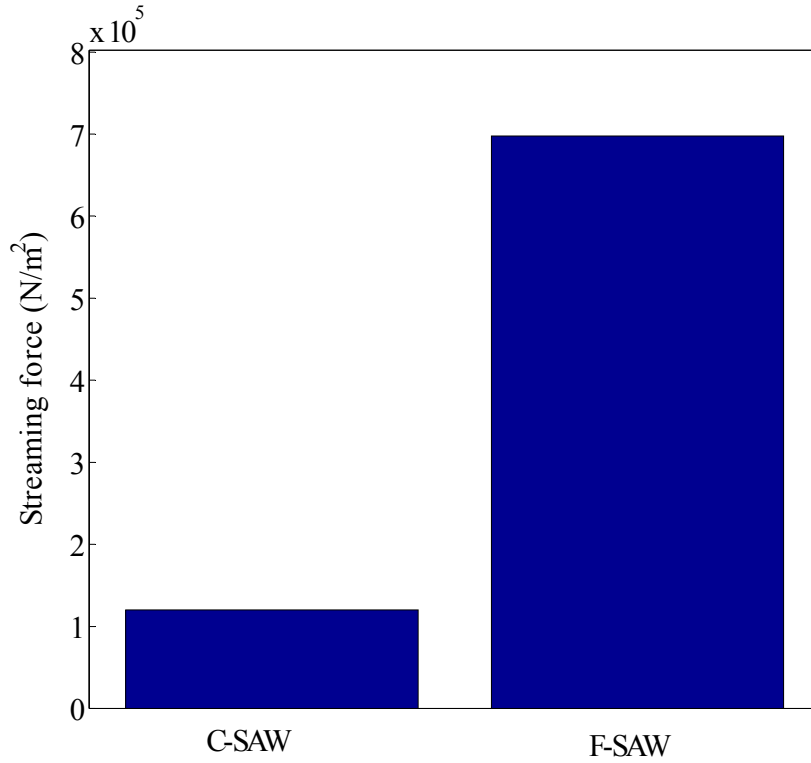
In line with the device displacement and fluid velocity patterns, the highest streaming force is observed near the input IDTs in the conventional SAW device and decays on moving

away from them whereas the streaming force peaks near the focal point in the F-SAW device (Fig. 6.9a). Further, the F-SAW induced streaming force is higher than the conventional SAW device throughout the delay path (Fig. 6.9a), providing higher magnitude of peak streaming force in the F-SAW device compared to the conventional SAW device (Fig. 6.9b) suggesting enhanced performance of the F-SAW device in biofouling elimination and other microfluidic applications, as brought out later.



(a)

Figure 6.9: Comparison of Streaming Forces (FSAW) for Focused SAW (F-SAW) vs. Conventional SAW (C-SAW) Device Having Uniform IDTs Corresponding to a Peak Applied Input AC voltage of 2.5 V (a) Streaming forces on the device surface along the propagation length. F denotes focal point of the F-SAW device (b) Maximum streaming force.

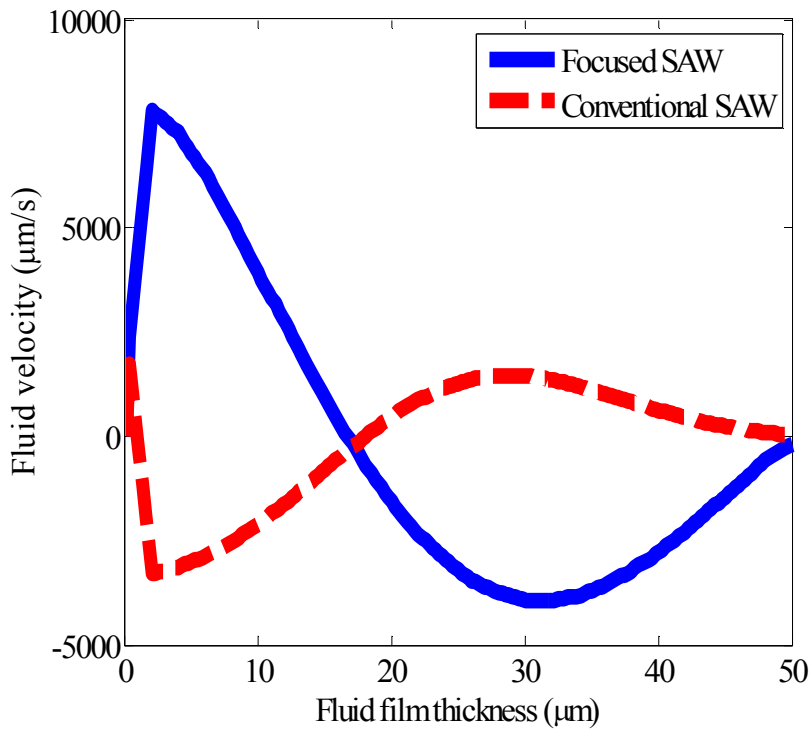


(b)

Figure 6.9: Continued

Equation (6-9) was used to compute the streaming velocity in the F-SAW device, which gives a time invariant mean flow. The calculated tangential and normal streaming velocity obtained for an F-SAW was compared to a conventional SAW device with the same wavelength (Fig. 6.10). The velocity profiles for both the devices indicate that the highest tangential and normal velocities occur close to the device surface. The fluid motion is confined to a small fluid thickness close to the device surface beyond which the wave motion is dampened significantly. In addition, beyond initial small fluid thickness, flow reversal is observed indicating fluid recirculation close to the SAW device surface. It is noteworthy that for both the devices, the tangential velocity component is higher as compared to the normal velocity component. This suggests that the streaming induced drag force is greater than the lift force. Further, the F-SAW

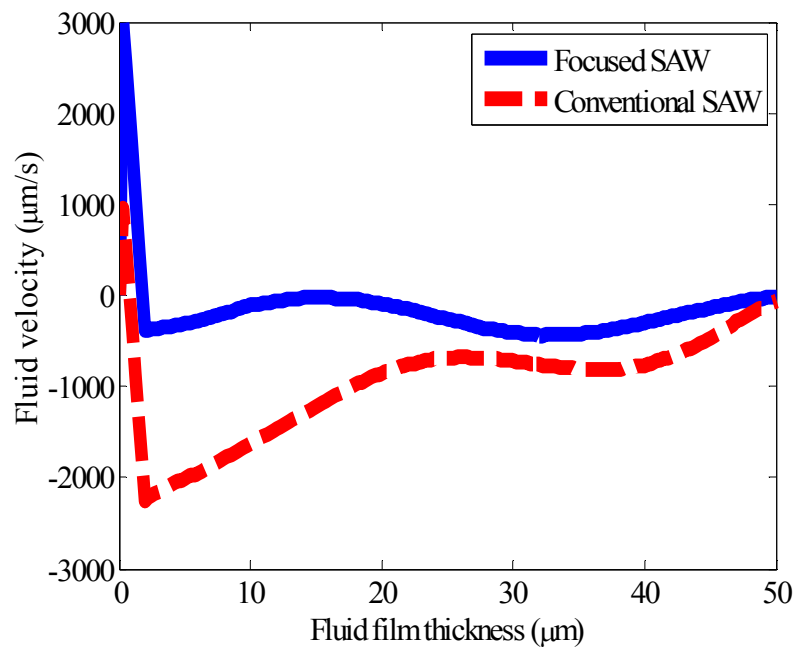
device generates much higher intensities of both forward and backward flow thereby suggesting a stronger recirculation as compared to conventional SAW. A comparison of the velocity fields between focused and conventional SAW devices indicates a significant increase in the tangential velocity in the propagation as well as transverse directions, normal velocity, and consequently total streaming velocity as a result of focusing brought about by the FSAW devices, leading to enhanced intensity of acoustic streaming. The F-SAW induced increase was found to be 352% and 216% for tangential velocities in propagation and transverse directions, respectively, and 353% for the normal velocity.



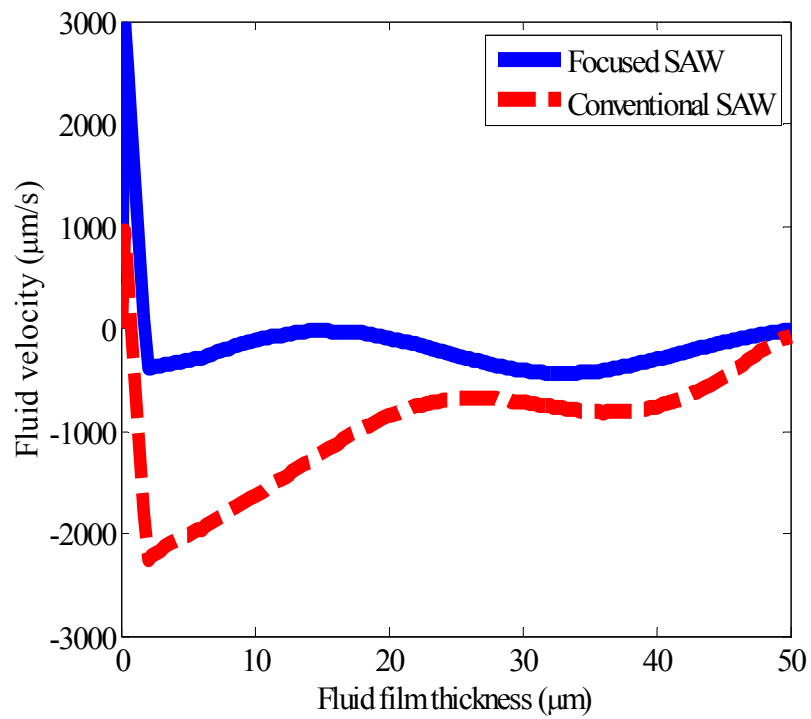
(a)

Figure 6.10: Comparison of Variation in Fluid Streaming Velocity Along the Fluid Film Thickness in Focused SAW vs. Conventional SAW Device for a Peak Input AC Voltage of 2.5 V

(a) Tangential fluid velocity in the propagation direction (b) Tangential fluid velocity in the transverse direction (c) Normal fluid velocity.



(b)



(c)

Figure 6.10: Continued.

As brought out in the forthcoming sections, the enhancement in acoustic streaming leads to enhanced particle removal capability of the F-SAW device, making them more suitable for biofouling elimination and biosensing applications compared to the conventional SAW device.

6.3.4 Non-Specifically Bound Protein Removal (Focussed vs. Conventional SAW)

Using the computed streaming velocities, various hydrodynamic[153] and adhesive forces were computed to predict and compare NSB removal from the F-SAW wand conventional SAW device. The NSB removal from the device surface is the result of a complex interplay between the adhesive and removal forces. When the device is in contact with the fluid domain, the adhesive forces are van der Waal's dispersion, electric double layer, and gravitational forces. However, the electrostatic double layer forces are ignored in an order of magnitude analysis as the maximum magnitude of these forces can be of the order of van der Waal's force. If the non specific protein in contact with the SAW device is modeled as a spherical particle of radius R, the non retarded van der Waal's force of adhesion between a sphere and a plate is given by [154]

$$F_{vdw} = \frac{AR}{6z^2}. A \text{ denotes Hamaker's constant (typical value of } 10^{-20} \text{ J), } z \text{ denotes the distance}$$

beyond which the adhesion force becomes retarded. Typically, z ranges from 0.2-0.4nm; in this work, z = 0.3 nm is used. The removal forces on the particle are mainly hydrodynamic in nature and are a result of the linear and non-linear fluid-device interactions that eventually give rise to acoustic streaming. The linear forces include added mass and Basset forces whereas the non-linear ones include radiation pressure, the SAW body force arising from the motion of the piezoelectric device, and acoustic streaming induced drag forces and lift forces. The added mass force is an inertial force which acts on a particle in an accelerating fluid due to the work done by the particle in displacing the fluid and changing the kinetic energy of the surrounding fluid. This force is computed as $F_{AM} \sim 2\pi f \rho R^3 u$. For particles submerged in the boundary layer of an

accelerating fluid, i.e. particle radius being comparable to the boundary layer thickness, the acceleration of the relative motion between the fluid and the particle leads to a delay in the boundary layer formation and viscous effects gain importance. These two effects are accounted for by the Basset force, given by $F_B = \sqrt{F_D F_{AM}}$; F_D denotes Stoke's drag. The particle in contact with the piezoelectric device is acted upon by a direct SAW body force resulting from the displacement of the device surface. The magnitude of this force is given by $F_{SAW} = \sqrt{F_x^2 + F_z^2} R^2$ where F_x and F_z denote the tangential and normal components of the body force computed at the center of the device given by [110, 122]

$$F_x = -\rho(1 + \alpha_1^2)A^2\omega^2k_i; F_z = -\rho(1 + \alpha_1^2)A^2\alpha_1\omega^2k_i \quad (6-10)$$

A denotes the magnitude of surface displacement, α_1 is the attenuation constant, ω is the device angular frequency and k_i is the leaky SAW wave number. The values of k_i and α_1 for the 100 MHz YZ-LiNbO₃ devices are computed to be 16409 m⁻¹ and 1.92, respectively.

The acoustic streaming induced drag force is given by $F_D \sim \mu R u_x$, the streaming induced lift force is given by $F_L \sim \mu (R u_z)^2$. The radiation pressure force is imparted by the acoustic radiation into the fluid and is given by [155]

$$F_{RS} \sim 8\rho \left(\frac{2\pi f}{c} \right) R^3 u^2 \sin(2kl) \left(\frac{1 + 2/3 \left(1 - \frac{\rho}{\rho_p} \right)}{2 + \frac{\rho}{\rho_p}} \right) \quad (6-11)$$

ρ_p denotes particle density, f denotes device frequency, μ and ρ represent fluid density and viscosity, respectively, u_x and u_z denote the tangential and normal acoustic streaming velocity components and u denotes total fluid velocity. The various forces have been computed for two different particle sizes, for the conventional and F-SAW devices and compared in Table 6.2.

Table 6.2: Comparison of Adhesive and Removal Forces Corresponding to Three Different Particle Sizes for Focused SAW (F-SAW) vs. Conventional SAW (C-SAW) Devices.

	R=0.03 μm		R=1.0 μm		R=50 μm	
	F-SAW	C-SAW	F-SAW	C-SAW	F-SAW	C-SAW
F_{vdw}	5.6×10^{-10}	5.6×10^{-10}	1.9×10^{-8}	1.9×10^{-8}	9.3×10^{-7}	9.3×10^{-7}
F_{g}	1.1×10^{-18}	1.1×10^{-18}	4.1×10^{-14}	4.1×10^{-14}	5.1×10^{-9}	5.1×10^{-9}
F_{SAW}	6.3×10^{-10}	1.1×10^{-10}	7.0×10^{-7}	1.2×10^{-7}	4.4×10^{-4}	3.0×10^{-4}
F_{D}	2.8×10^{-13}	1.2×10^{-13}	9.4×10^{-12}	4.0×10^{-12}	4.7×10^{-10}	2.0×10^{-10}
F_{L}	2.9×10^{-17}	6.1×10^{-18}	3.2×10^{-14}	6.8×10^{-15}	8.1×10^{-11}	1.7×10^{-11}
F_{AM}	8.0×10^{-16}	4.6×10^{-16}	3.0×10^{-11}	1.7×10^{-11}	3.7×10^{-6}	2.1×10^{-6}
F_{B}	3.0×10^{-14}	1.9×10^{-14}	3.3×10^{-11}	2.2×10^{-11}	8.3×10^{-8}	5.4×10^{-8}
F_{RS}	1.5×10^{-18}	3.3×10^{-19}	5.4×10^{-14}	1.2×10^{-14}	6.8×10^{-9}	1.5×10^{-9}

A comparison of the various forces reveals that while the hydrodynamic forces are smaller compared to the adhesive van der Waal's force, the direct SAW body force is of sufficient magnitude to overcome the adhesive force. Following particle detachment, preventing particle reattachment to the surface becomes critical to achieve biofouling elimination. From the order of magnitude analysis, it appears that the acoustic streaming induced drag and lift, radiation pressure, Basset, and the added mass forces appear to be inconsequential as they are much smaller compared to the van der Waal's adhesive force. However, it is important to note that both the SAW body force and van der Waal's force decrease with increasing distance from the device surface. Therefore, after the particle becomes fluid borne and moves away from the zone of adhesion to a distance where the van der Waal's force becomes insignificant and the gravitational

force $\left(F_g \sim \frac{4\pi R^3 \rho g}{3} \right)$ (g denotes gravitational constant) is the prominent adhesive force that

can bring the particle closer to the device surface for reattachment. At this juncture, the hydrodynamic forces come into play, which include drag, lift, acoustic radiation, added mass, and Basset forces and can easily overcome F_g . Thus, these hydrodynamic forces play a key role in preventing the reattachment of the particle to the device surface by overcoming F_g . This interplay of the various adhesive and removal forces is summarized in Fig. 6.11.

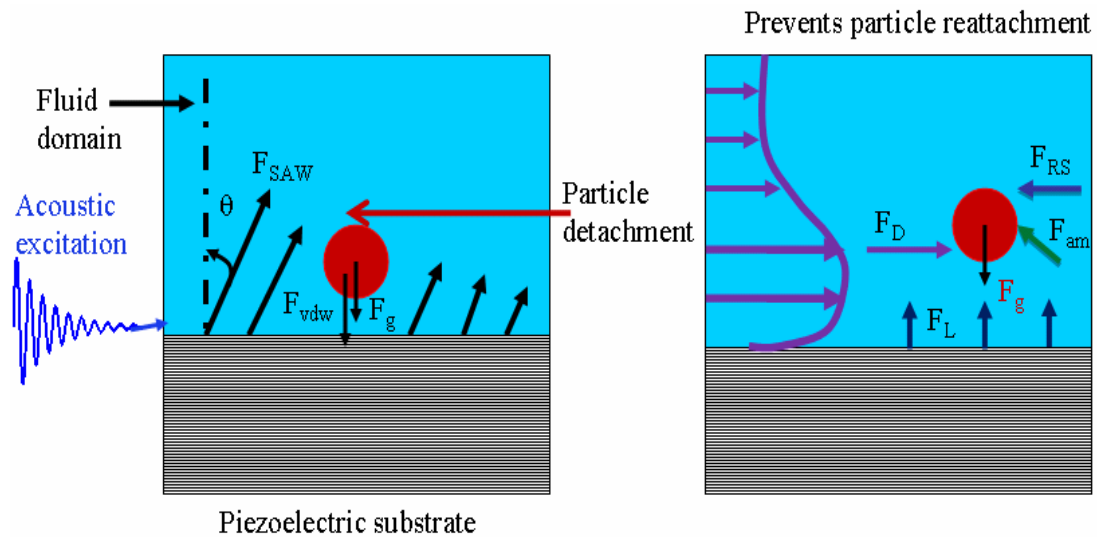


Figure 6.11: Illustration of the Interplay of Various Adhesive and Removal Forces on the Non-Specific Proteins Bound to the SAW Surface. The SAW body force leads to particle detachment from the device surface while the hydrodynamic forces including added mass, acoustic radiation, acoustic streaming induced drag and, lift prevent particle re-attachment to the surface and are responsible for particle transport from the fluid stream. F_{SAW} , F_D , F_{am} , F_L , F_g , F_{vdw} denote SAW body, streaming induced drag, added mass, streaming induced lift, gravitational and van der Waal's forces, respectively.

A comparison of the various forces also reveals that for very small sub-micron particles, streaming induced drag is larger compared to the other hydrodynamic removal forces; however for larger particles, the added mass and Basset forces are larger than streaming induced drag and lift forces. Therefore, particle advection by streaming induced drag is a dominant mechanism in preventing particle reattachment following detachment for sub-micron particles whereas the added mass force due to the accelerating fluid plays a dominant role in preventing particle reattachment and removal of very large particles. Nevertheless, the interplay of the various hydrodynamic and adhesive forces leads to a net particle displacement which ultimately translates to particle removal from the fluid stream.

From Table 6.2, it is evident that the F-SAW device generates higher magnitudes of hydrodynamic and direct SAW body removal forces compared to the conventional SAW device due to an increase in the intensity of acoustic streaming as well as induced streaming velocities (Fig. 6.10) as a result of the acoustic energy focusing in a small localized area. It is important to note that for large particle sizes such as $50\ \mu\text{m}$, the hydrodynamic removal force such as added mass is sufficient to overcome the adhesive van der Waal's force in the conventional as well as the F-SAW device whereas for smaller particle sizes such as $R = 1.0\ \mu\text{m}$, only the SAW body force is of sufficient magnitude to overcome the adhesive force; the other hydrodynamic forces come into play after the adhesive force becomes insignificant some distance away from the surface. For very small particles ($R = 0.03\ \mu\text{m}$), the removal forces in the conventional SAW cannot inflict particle removal owing to their smaller magnitude compared to the adhesive van der Waal's force; however the F-SAW induced SAW body force overwhelms the van der Waal's force and facilitates sub-micron particle size elimination. Therefore, it appears that while the removal of sub-micron sized particles is not achievable in a conventional SAW device, the high intensity focused beam in the F-SAW device is instrumental in removing smaller sub-micron sized particles.

It can be seen that as particle size reduces, the removal forces namely the direct SAW body force and hydrodynamic forces namely drag, added mass, Basset, radiation pressure forces decay much faster compared to the adhesive van der Waal's force since the latter varies linearly with particle size whereas the removal forces, excluding the lift force, vary as higher powers of particle size. Therefore, removal of smaller particles poses a greater challenge while it is relatively easy to remove larger particles. The smallest particle removable *via* acoustic streaming can be computed in the limit when the SAW body force overcomes the adhesive van der Waal's force and is used as an indicator of removal efficiency of the SAW device. The smallest particle radius (R_{\min}) is given by

$$R_{\min} = \frac{A}{6z\sqrt{F_x^2 + F_z^2}} \quad (6-12)$$

The ability of the F-SAW device to generate higher magnitudes of hydrodynamic and direct SAW body removal forces compared to the conventional SAW device, as discussed before, manifests itself as the ability of the F-SAW to remove much smaller particles compared to the conventional SAW device (Fig. 6.12), thereby ensuring higher removal efficiency of the F-SAW device. It is also worthwhile to note that in a conventional SAW device, the smallest particle is removable near the input IDT region owing to the fact that the device displacements and therefore streaming force are highest near the input IDTs and decay exponentially on moving away from the source; thus only larger particles can be removed in the delay path away from input IDTs. However, in a F-SAW device, the smallest particle can be removed at the focal point of the device in the center of the delay path due to localized acoustic energy focusing. Further, the acoustic streaming enhancement due to acoustic energy focusing manifests itself as the capability of the F-SAW to remove much smaller particles throughout the delay path corresponding to the sensing region, which are otherwise not removable using the conventional SAW. The F-SAW device presents almost an order of magnitude reduction in the smallest removable particle size compared

to the conventional SAW, allowing for the removal of sub-micron sized particles which cannot be removed by the conventional device. Thus, the F-SAW device provides an enhancement over the conventional SAW device through its ability to achieve increased biofouling removal efficiency throughout the delay path or the sensing region, thereby enhancing device sensitivity, selectivity and permitting device reuse. These results suggest acoustic wave focusing brought about by F-SAW device is an efficient technique to generate enhancing streaming velocities and streaming forces, which can be utilized for a plethora of microfluidic actuation and sensing applications.

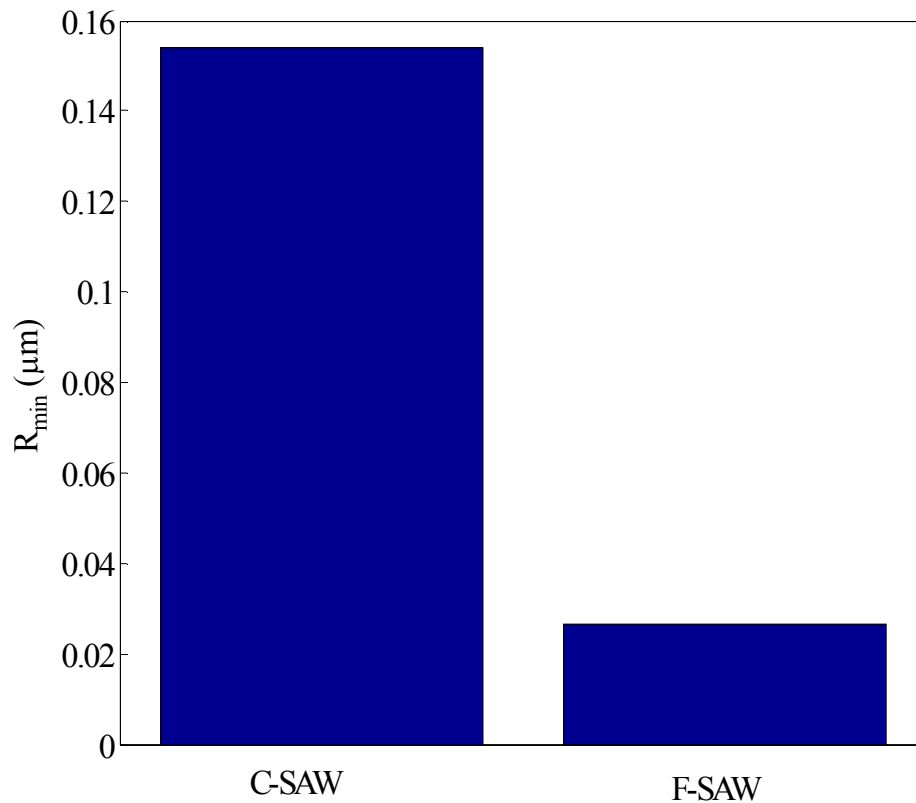


Figure 6.12: Comparison of Radius of the Smallest Particle (R_{\min}) That Can Be Removed, in a Conventional SAW (C-SAW) vs. Focused SAW (F-SAW) device. The smallest particle is removed near the input IDTs in the C-SAW device and focal point in the F-SAW device.

6.4 Conclusion

In summary, 3-D FE-FSI models were developed for an F-SAW device to investigate acoustic streaming flow fields and evaluate the enhancement in acoustic streaming induced biofouling elimination brought about by the F-SAW device in comparison to a conventional SAW. Results from the FSI simulations indicate an increase in the surface displacements, fluid velocity, and streaming force in F-SAW device compared to a conventional SAW device with a similar size, finger periodicity and applied input voltage. Further, the acoustic energy focusing in the F-SAW device leads to maximized surface displacements, fluid velocity, and consequently streaming force near the focal point in the center of the delay path in contrast to the conventional SAW in which the peak surface displacements, fluid velocity, and streaming force occur near the input IDTs and decay rapidly on moving away from them. The fluid vector streamlines in the conventional device differ significantly from those in the F-SAW device. The velocity vectors in the conventional SAW indicate maximum intensity of recirculation and IDTs near the IDTs, which reduce away from the IDTs. In contrast, the concentric IDTs focus the fluid flow near the device focal point, leading to maximum intensity of recirculation near the focal point in the F-SAW device. The streaming velocities obtained using the FE-FSI simulations were used to compute the various adhesive and hydrodynamic removal forces on the non-specifically bound protein particles. A comparison of the various forces indicates that the interplay between the adhesive van der Waal's and gravitational forces, SAW body force and the hydrodynamic removal forces leads to a net particle displacement which eventually translates to NSB protein detachment from the device surface as well as their removal from the fluid stream. The smallest removable particle size was used as a measure of the biofouling elimination efficiency in the SAW device. Whereas conventional SAW removes smallest particle near the input IDTs, the F-SAW device realizes the elimination of smallest particles near the focal point in the delay path corresponding to the sensing region. Further, the results from the developed FE FSI models indicate that the

acoustic streaming enhancement in the F-SAW device manifests itself in the F-SAW device capability to remove much smaller particles compared to the conventional SAW having uniform IDTs. The enhanced biofouling elimination capability owing to the acoustic streaming enhancement brought about by the F-SAW device increases the suitability of the F-SAW device in biosensing applications, providing higher sensitivity, selectivity, and device reuse capabilities. Although the results have been discussed in the context of biofouling elimination in biosensors, the findings of this work are of general applicability and have tremendous significance for other microfluidic actuation applications of SAW devices.

Chapter 7

Design of Mutually Interacting Multi-Directional Transducer Configurations on a Surface Acoustic Wave Device for Enhanced Biosensing

Transducers used in biosensing applications are plagued by biofouling, which refers to the binding of non-specific proteins to the device surface resulting in a compromise of the device sensitivity and selectivity. Acoustic streaming, resulting from high intensity sound waves, has the potential to address the issue of biofouling elimination in biosensors. Multi-directional transducers have the capability of achieving the dual objectives of biosensing and non-specifically bound protein removal for improved sensor performance. Also, focused interdigital transducers (IDTs) have the potential for acoustic energy focusing, thereby increasing the intensity of acoustic streaming. In the previous chapters, it has been identified that various crystallographic orientations allow the propagation of different modes thereby rendering them suitable for different applications. For example, in Langasite, shear horizontal modes propagate along $(0, 22, 90)$ Euler direction while mixed modes with prominent surface normal component are obtained along $(0, 22, 0)$ direction. Thus, the $(0, 22, 90)$ and $(0, 22, 0)$ directions are suitable for biosensing and the removal of NSB founding proteins from device surface, respectively. In this chapter, a Langasite based biosensor, with a mutually interacting multidirectional IDT configuration along the two identified Euler directions for enhanced biosensor performance, is investigated using 3-D FE models. Uniform IDTs (U-IDTs) are employed in the $(0, 22, 90)$ direction while focused IDTs (F-IDTs) are placed along the $(0, 22, 0)$ direction. The enhancement in sensor performance was analyzed in terms of device sensitivity and acoustic streaming force.

The results indicate that the streaming force and the sensitivity for the device with the mutually interacting U-IDTs/F-IDTs are significantly higher when compared to uniform unidirectional IDTs. Thus, the Langasite based device with mutually interaction U-IDTs and F-IDTs represents a significant enhancement over the conventional SAW device having uniform IDTs and is better suited for biosensing applications. This work broadly applies to all transducers used for biological species sensing that suffer from fouling and non-specific binding of protein molecules to the device surface.

7.1 Introduction

Surface acoustic wave devices find use in an array of applications including biosensing, chemical sensing, gene expression analysis, actuation, droplet excitation, and lab-on-chip systems, to name a few [9, 10, 46, 47]. However, biosensing applications of SAW devices suffer from reduction in sensitivity and selectivity owing to the binding of non-specific proteins from the biosensing medium, to the device surface, thereby severely compromising device performance. Acoustic streaming, resulting from the interaction of Rayleigh waves propagating in the piezoelectric device with the fluid domain, has been shown to remove non-specifically bound (NSB) proteins from the device surface. Biosensing and NSB protein removal requires the propagation of various types of wave modes. While a shear horizontal mode, which can resist attenuation in the fluid domain, is potentially beneficial for biosensing of target moieties, a Rayleigh wave is most suited to knock off the NSB proteins from the device surface *via* the phenomenon of acoustic streaming. Selective exploitation of different wave characteristics along various Euler directions holds the key to address the issue of achieving the dual objective of biosensing and biofouling elimination. In the previous chapters, we have demonstrated the possibility of simultaneous sensing and biofouling elimination on a single device, *via* the use of orthogonal IDTs on Langasite. It has also been established, in the previous chapters, that for

devices based on a Langasite substrate the $(0, 22, 90)$ allows for propagation of shear horizontal mode and is, therefore, best suited for biosensing [139]. The $(0, 22, 0)$ direction is ideal for the generation of waves with prominent surface normal component and hence is critical for NSB removal [139]. Further, efficient removal of NSB proteins *via* acoustic streaming requires the generation of high enough fluid velocities and Rayleigh wave amplitudes. Furthermore, this dissertation has also established that devices with focused interdigital transducers (F-IDTs) based on concentric wave surfaces provide enhanced acoustic streaming compared to the conventional SAW device with uniform IDTs (U-IDTs) [156, 157]. In this chapter, the concepts from the device design configurations explored in the previous chapters are combined to achieve high streaming forces while providing improved sensing capabilities of Langasite based biosensor. Specifically, the orthogonal IDT configuration explored in Chapter 4 is further modified to include F-IDTs along the $(0, 22, 0)$ direction while U-IDTs along the $(0, 22, 90)$ direction. The aim is to exploit the capability of the F-IDTs to generate high streaming forces along the $(0, 22, 0)$ direction which allows for the propagation of waves with a prominent surface normal component. This chapter presents the first report on a Langasite based biosensor employing mutually interacting F-IDTs and U-IDTs along the two different crystallographic directions, in order to allow for enhanced biofouling efficiency along the $(0, 22, 0)$ direction while simultaneously allowing for sensing along the $(0, 22, 90)$ direction. Three dimensional (3D) coupled field finite element (FE) models are developed to investigate the second order effects arising from such a combination of mutually interacting IDTs and biosensor performance is analyzed in terms of device sensitivity and biofouling removal efficiency. The results are compared with those for a conventional SAW device having U-IDTs along $(0, 22, 90)$ Euler direction. Such a device is expected to provide enhanced performance compared to a conventional SAW device having U-IDTs along $(0, 22, 90)$ direction and orthogonal device having mutually interacting U-IDTs along each of the $(0, 22, 0)$ and $(0, 22, 90)$ directions.

7.2 Computational and Model Details

7.2.1 Fluid Domain

Fluid is modeled as an incompressible, viscous, Newtonian fluid using the Navier-Stokes and continuity equation in the Eulerian frame of reference given below

$$\rho \left(\frac{\partial \mathbf{v}_f}{\partial t} + \mathbf{v}_f \cdot \nabla \mathbf{v}_f \right) + \nabla P - 2\eta \nabla \cdot \mathbf{D} = 0 \quad (7-1)$$

$$\nabla \cdot \mathbf{v}_f = 0 \quad (7-2)$$

Here, \mathbf{v}_f , P , ρ and η denote the fluid velocity, pressure, density, and viscosity, respectively. \mathbf{D} is the rate of deformation tensor given by

$$\mathbf{D} = \frac{1}{2} (\nabla \mathbf{v}_f + (\nabla \mathbf{v}_f)^t) \quad (7-3)$$

7.2.2 Piezoelectric Domain

For the piezoelectric solid, the equation of motion is obtained by modifying the elastic constitutive equation for a non-piezoelectric solid to account for the coupling between the electric field and mechanical strain. The interaction between the electric field and mechanical strain is studied by coupling the elastic and electromagnetic constitutive equations through a piezoelectric matrix [34, 116-119].

$$\underline{T} = [c] \underline{S} - [e] \underline{E} \quad (7-4)$$

$$\underline{D} = [e]^T \underline{S} + [\varepsilon] \underline{E} \quad (7-5)$$

The resulting equations, known as the piezoelectric constitutive equations, describe the interaction between elastic strain, stress, and electric field in the piezoelectric substrate. Here, \underline{T} and \underline{D} denote stress and electric flux density vectors, respectively. \underline{S} , \underline{E} denote structural strain

and electric field intensity vectors, respectively. c , e , and ε represent structural elasticity matrix at constant electric field, piezoelectric stress matrix, and dielectric matrix at constant mechanical strain, respectively.

In the absence of body force, the equation of motion is given by

$$\nabla \cdot T = \rho \ddot{u} \quad (7-6)$$

where ρ is the density and u represents displacement, $\ddot{u} = \frac{\partial^2 u}{\partial t^2}$

The electric field intensity is given by the gradient of the electric potential (φ)

$$E = -\nabla \varphi \quad (7-7)$$

The strain tensor is symmetric, therefore

$$S_{ij} = \frac{1}{2} \left(\frac{\partial u_i}{\partial x_j} + \frac{\partial u_j}{\partial x_i} \right) \quad (7-8)$$

Substituting eqns. (7-7) and (7-8) in eqn. (7-4), we obtain T in tensor notation as

$$T_{ij} = \sum_{k,l=1}^3 c_{ijkl} \frac{\partial u_l}{\partial x_k} + \sum_{k=1}^3 e_{ijk} \frac{\partial \varphi}{\partial x_k} \quad (7-9)$$

Substituting eqns. (7-7), (7-8), (7-9) in eqn. (7-6),

$$\sum_{j,k,l=1}^3 c_{ijkl} \frac{\partial^2 u_l}{\partial x_k \partial x_j} + \sum_{j,k=1}^3 e_{ijk} \frac{\partial^2 \varphi}{\partial x_k \partial x_j} = \rho \frac{\partial^2 u_i}{\partial t^2} \quad (7-10)$$

In a system with no free charges,

$$\nabla \cdot D = 0 \quad (7-11)$$

Combining eqns. (7-5), (7-7), and (7-11),

$$\sum_{j,k,l=1}^3 e_{jkl} \frac{\partial^2 u_l}{\partial x_k \partial x_j} - \sum_{j,k=1}^3 \varepsilon_{jk} \frac{\partial^2 \varphi}{\partial x_k \partial x_j} = 0 \quad (7-12)$$

Equation (7-10) represents three equations in four unknowns, namely the three displacements and the voltage (ϕ) which combined with equation (7-12), forms a set of coupled wave equations that can be solved for the four unknowns. These equations are discretized in space and time, and solved at the nodes in the finite element domain to obtain a transient solution.

7.2.3 Fluid-Solid Interaction

The solution of fluid and solid fields in the finite-element domain requires the use of either the Lagrangian or Eulerian frame of reference. The Eulerian frame refers to the fixed frame of reference whereas Lagrangian frame is a moving frame of reference. In the Lagrangian frame, the grid deforms as the region of interest deforms. Whereas the structural phase (piezoelectric substrate) is best described using the Lagrangian frame, either frame of reference can be used for the fluid domain. In the Lagrangian frame, the mesh embedded in the fluid domain moves with the velocity of the fluid while in the Eulerian frame, the mesh, through which the fluid moves, is fixed.

A purely Lagrangian frame is not suitable for dealing with strong distortions of the fluid mesh arising from the non-cohesive nature of fluid particles which causes them to travel independently and diverge in space. A purely Eulerian frame for the fluid domain introduces complexity in fluid-solid coupling as it is unable to track the path of the elements. Therefore, Arbitrary-Lagrangian-Eulerian (ALE) methods, which combine the best of the both frames of reference, are used for kinematical description of the fluid domain in such problems. In ALE, the Lagrangian frame is used for ‘almost contained’ flows and Eulerian description is used for regions where the mesh would be highly distorted if required to follow fluid motion. The theory for ALE has been developed by Hughes et al. for viscous, incompressible flows [120]. In the ALE framework, the fluid equation of motion can be written as [121]

$$\rho \left(\frac{\partial v_f}{\partial t} \right) + (v_f - w) \cdot \nabla v_f + \nabla P - 2\eta \nabla \cdot D = 0 ; \quad (7-13)$$

where w is the grid velocity such that $w \neq v_f \neq 0$.

To achieve fluid-solid coupling, an interface is defined across which displacements are transferred from solid to fluid and pressure from fluid to solid. These conditions translate to no-slip for the fluid domain (velocity continuity) and stress continuity for solid domain given by

$$v_f = v_s = \frac{\partial u}{\partial t} \quad (7-14)$$

$$\sigma_{ij}^s n_j^s + \sigma_{ij}^f n_j^f = 0 \quad (7-15)$$

n_j is the outward normal at the solid-liquid interface in the deformed configuration, i denotes longitudinal direction. Superscripts f and s denote fluid and structural domain, respectively. The fluid mesh is continuously updated as the piezoelectric substrate undergoes deformation.

7.2.4 Finite Element Model

A three dimensional finite element model of a SAW device based on Langasite substrate, with U-IDTs/F-IDTs was developed [158], as shown in Fig. 7.1. The dimensions of the piezoelectric substrate were 1600 μm width x 1600 μm propagation length x 200 μm depth.

The device was modeled with two port delay line consisting of two sets of IDTs along each of the two delay paths: the input IDTs and the output IDTs. The fingers were defined with periodicity of 40 μm and aperture width of 200 μm along the (0, 22, 90) direction. Along the (0, 22, 0) direction, aperture width of the fingers varies depending on their radial distance from device center. The model was meshed with tetragonal solid elements with four degrees of freedom, three of them being the three translations and the fourth being the voltage. To optimize on the computation time while capturing the dynamics accurately, highest mesh densities were ensured near the device surface and the middle of the substrate. A total of 388, 893 nodes and 266, 762 elements were generated. An impulse response analysis was performed during 190 ns by applying

an impulse voltage of 100 V at the input IDT and employing a time step of 0.95 ns to deduce the central frequency of the device in each direction.

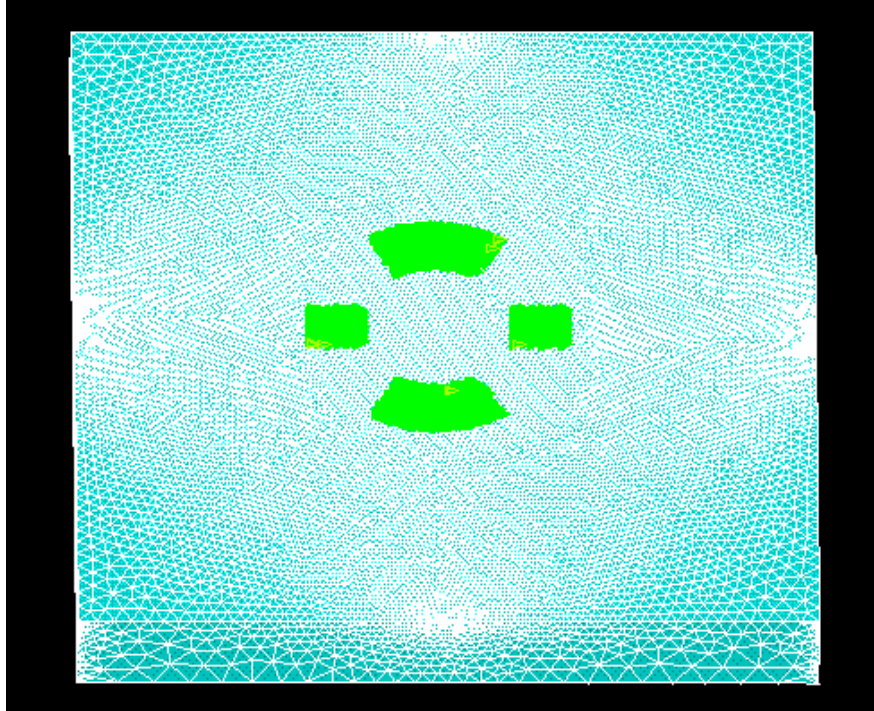


Figure 7.1: Meshed Model Showing Mutually Interacting Inter-Digital Transducers Along Different Euler Directions. Focused IDTs are used along $(0, 22, 0)$ direction and uniform IDTs are used along $(0, 22, 90)$ direction

The central frequencies were computed as 68 MHz and 64 MHz along the $(0, 22, 90)$ and $(0, 22, 0)$ direction, respectively. Subsequently, an ac analysis was carried out using the respective frequency in each Euler direction, by applying a peak voltage of 2.5 V to the input IDTs in each of the two Euler directions and employing a time step of 1 ns, to investigate the nature of waves propagating in the two directions. The device sensitivity and acoustic streaming force were computed and compared with devices having uniform unidirectional IDTs in the respective directions.

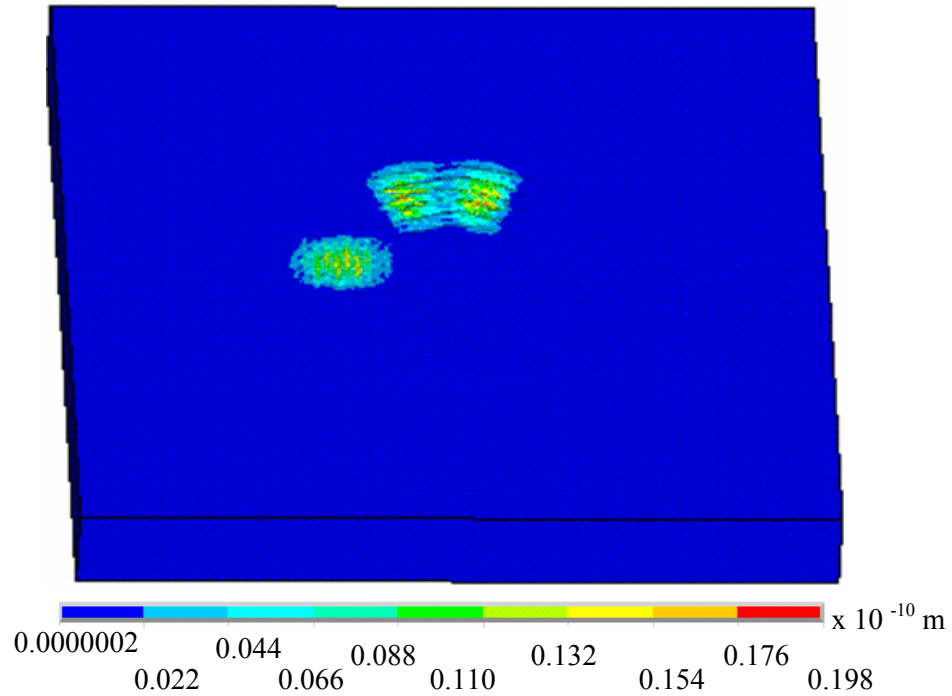
7.3 Results and Discussion

Previous experimental and computational studies have demonstrated acoustic streaming induced by Rayleigh waves with prominent surface normal component can be effectively used to achieve removal of non-specifically bound (NSB) proteins from the device surface, thereby enhancing device performance [99, 110]. The key biosensing issues which are addressed in this work include identifying transducer configurations that lead to enhanced sensitivity while simultaneously enhancing the biofouling elimination capability of the device. Enhancement in acoustic energy confinement to the device surface brings about improvement in device sensitivity while increase in acoustic streaming intensity is related to increase in the efficiency of biofouling elimination. Results from the developed 3D coupled field FE simulations involving unidirectional IDTs along different Euler directions indicate that while pure shear horizontal mode propagates along (0, 22, 90) direction, thereby rendering it ideal for biosensing in fluid media, the (0, 22, 0) direction is most suited for acoustic streaming induced biofouling elimination owing to mixed modes with dominant surface normal component of displacement [139]. Specifically, in this chapter, the enhancement in acoustic streaming along the (0, 22, 0) direction and increase in device sensitivity along (0, 22, 90) direction is investigated, through the use of mutually interacting F-IDTs and U-IDTs in the respective directions. The simulations account for second order effects arising from the interaction of the IDTs.

7.3.1 Device Displacements and Device Sensitivity

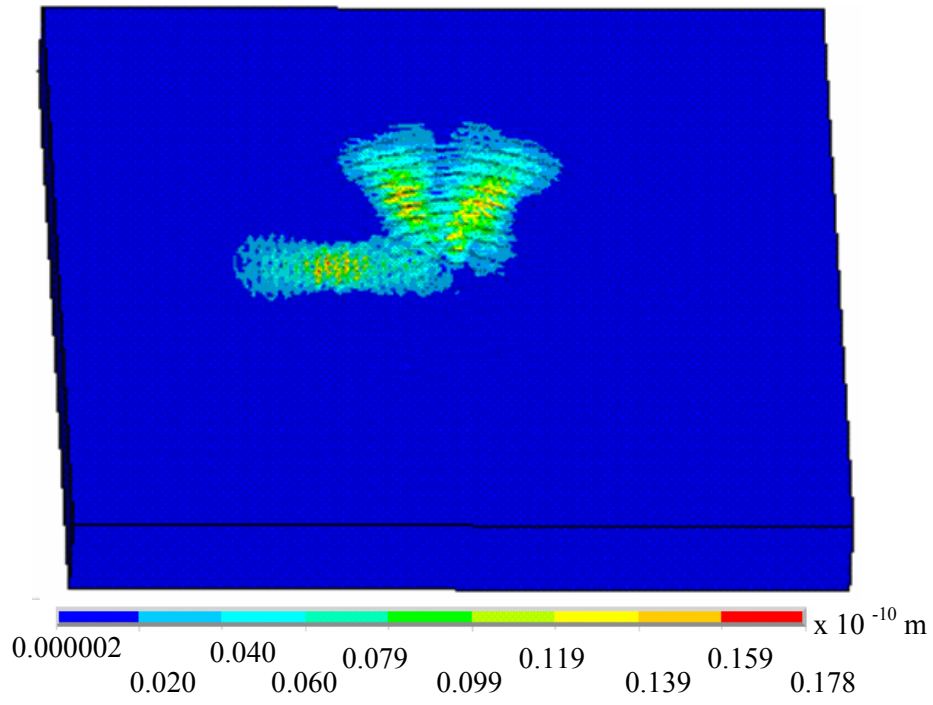
The current simulations indicate that the use of mutually interacting U-IDTs/F-IDTs leads to the focusing of waves along the (0, 22, 0) direction lead (Fig. 7.2) thereby maximizing the device displacements near the focal point. Further, the use of focused IDTs along (0, 22, 0) direction allows for amplification of the prominent surface normal component in the propagating

mixed mode wave as well as the focusing of the acoustic waves near the device focal point at the center of the delay path.

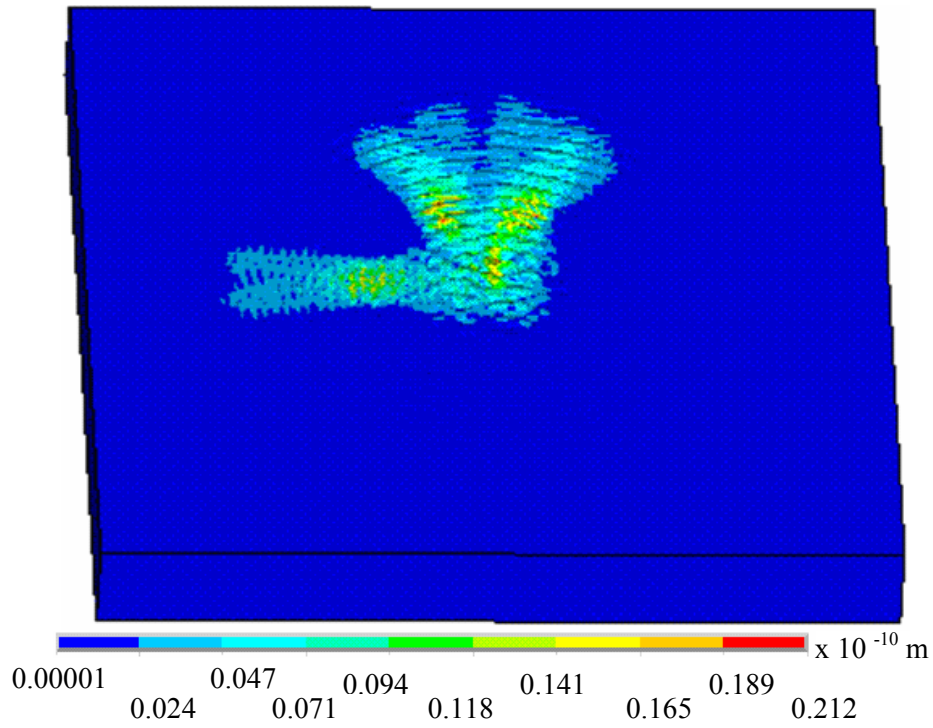


(a)

Figure 7.2: Displacement Contours at Various Time Instants on the Surface of the SAW Device With Mutually Interacting Orthogonally Oriented Uniform and Focused IDTs (a) 30 ns (b) 70 ns (c) 100 ns (d) 150 ns (e) 180 ns. Propagation direction (0, 22, 90) with uniform IDTs has a pure shear horizontal mode which would be used for biosensing. Orthogonally located focused IDTs along (0, 22, 0) direction allow for amplification of surface normal component leading to significantly higher streaming forces. Scale bar is in meters.

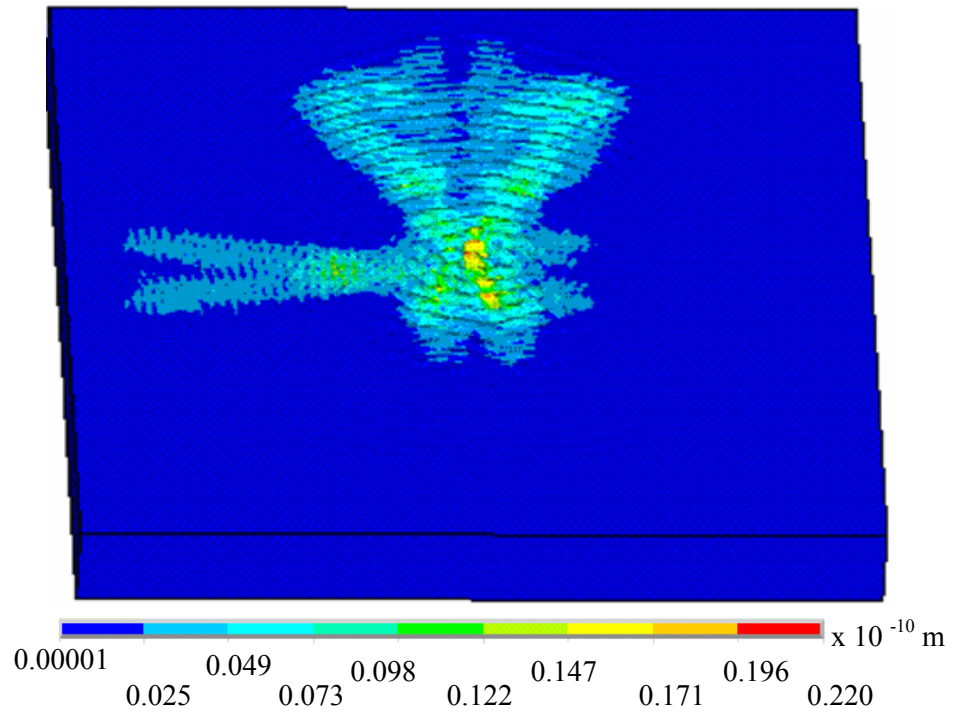


(b)

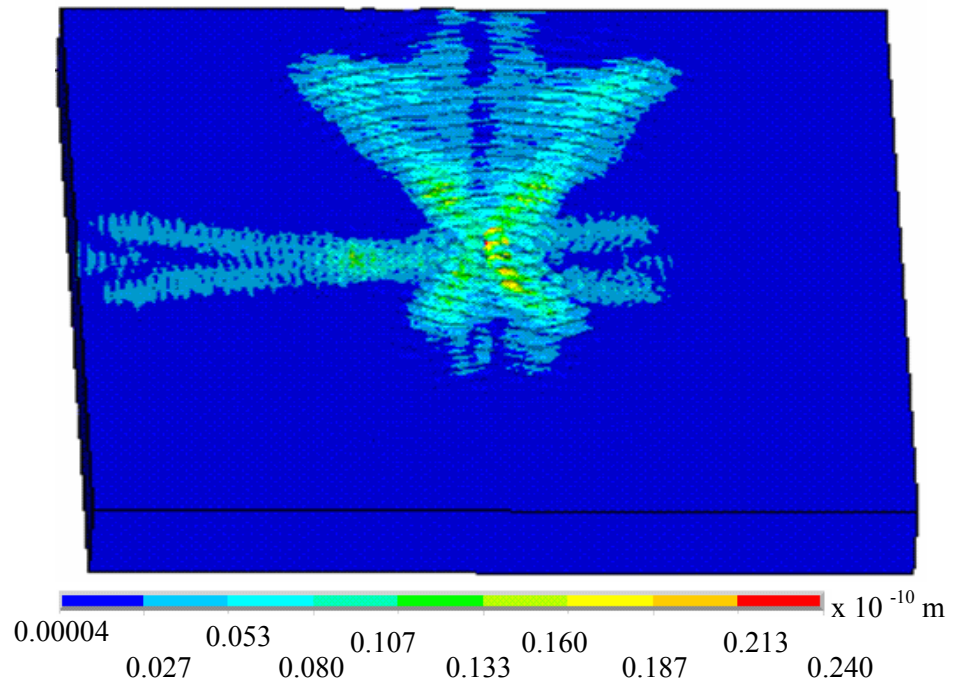


(c)

Figure 7.2: Continued.



(d)



(e)

Figure 7.2: Continued.

The device sensitivity was computed using the perturbation theory utilizing the mass sensitivity equation given by [143]:

$$S = -\frac{f_0 \omega^2}{4} \left(\frac{u_x^2 + u_y^2 + u_z^2}{U} \right) \quad (7-16)$$

f_0 , ω , U represent to mode center frequency, angular frequency, and average area density of wave energy, respectively. u_x , u_y , and u_z were derived from the finite element simulations.

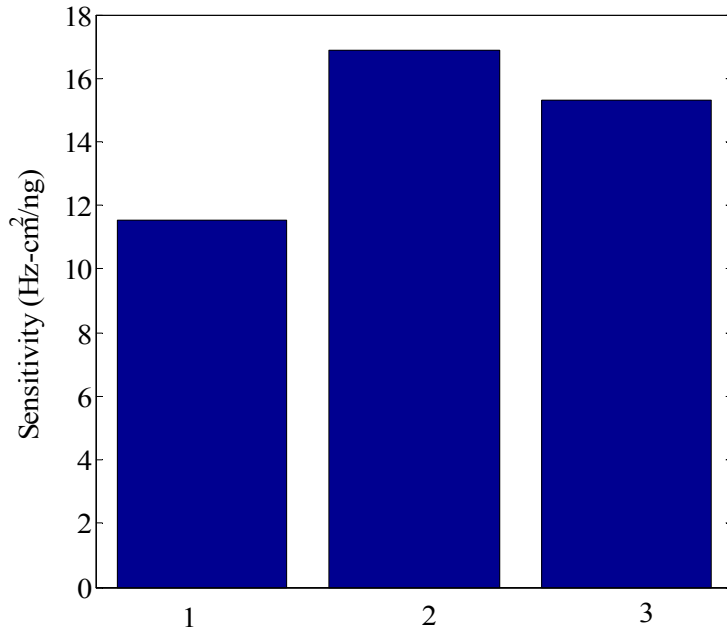


Figure 7.3: Biosensor Sensitivity on a Langasite Substrate Calculated Along the (0, 22, 90) Direction. Comparison of mass sensitivities for mutually interacting multidirectional (U-IDT/F-IDT) SAW with standard unidirectional SAW device and orthogonal SAW device with U-IDTs is shown. The term ‘conventional IDTs’ refers to single split uniform IDT configuration. (1) denotes standard unidirectional SAW device having U-IDTs along (0, 22, 90); (2) denotes orthogonal SAW device having mutually interacting U-IDTs along the (0, 22, 0) and (0, 22, 90) directions; (3) denotes orthogonal SAW device having mutually interacting U-IDTs along (0, 22, 90) and F-IDTs along (0, 22, 0) directions.

The sensitivity for the different device configurations is shown in Fig. 7.3. The constructive interference of propagating waves in the delay path leads to maximized energy entrapment and displacements on the device surface, thereby imparting 32.4% higher sensitivity to the device with U-IDTs/FIDTs ($15.3 \text{ Hz-cm}^2/\text{ng}$) compared to the standard unidirectional IDT design ($11.56 \text{ Hz-cm}^2/\text{ng}$) and almost comparable sensitivity in relation to the orthogonal SAW device with mutually interacting U-IDTs along the (0, 22, 90) and (0, 22, 0) Euler directions ($16.89 \text{ Hz-cm}^2/\text{ng}$) (Fig. 7.3).

7.3.2 Fluid Velocities and Streaming Forces

Since biosensing typically occurs in liquid media such as blood or urine placed in contact with the piezoelectric device, the acoustic energy focusing in the device would lead to the same effect in the velocity of the fluid in contact with the piezoelectric device, thereby focusing and enhancing the fluid velocity near the device focal point. This is evident from Fig. 7.4, which shows the focusing effect of the F-IDTs such that the peak fluid velocity occurs near the device focal point in the center of the delay path of the device with combined F-IDTs and U-IDTs. This convergence of fluid velocities leads to the development of high shear stress gradients near the focal point, which combined with the high shear stresses in the region can help in detaching and knocking off the NSB proteins from the device surface. Further, the focusing and enhancement of acoustic energy leads to an increase in the acoustic streaming force (Fig. 7-5) which plays a key role in detaching the NSB proteins from the device surface. Also, an enhancement in the fluid velocities resulting from the use of F-IDTs leads to an increase in the fluid induced hydrodynamic removal forces such as drag and lift, which facilitate NSB removal.

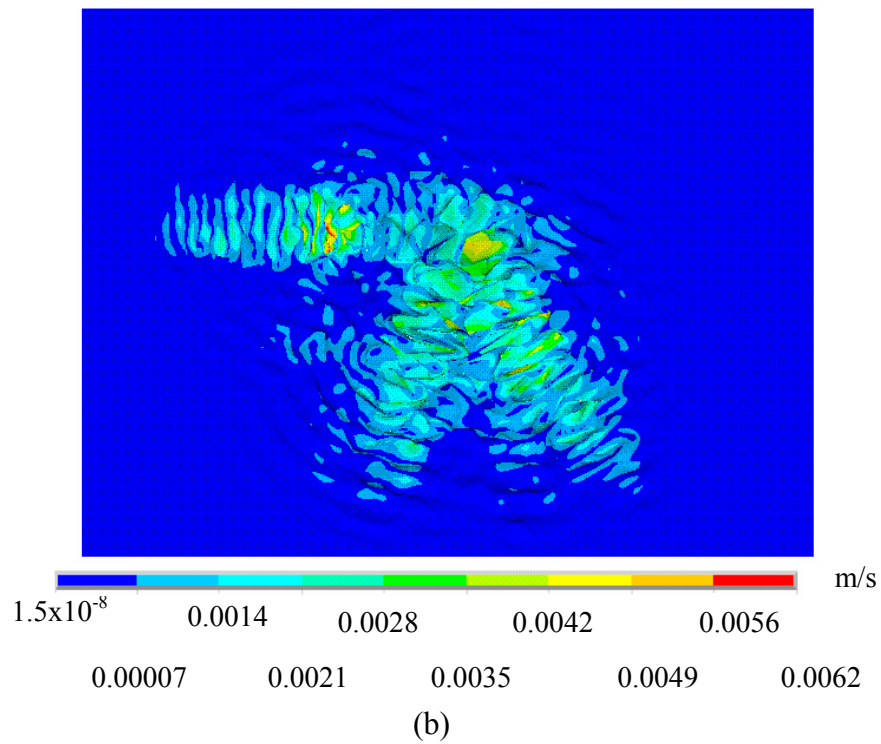
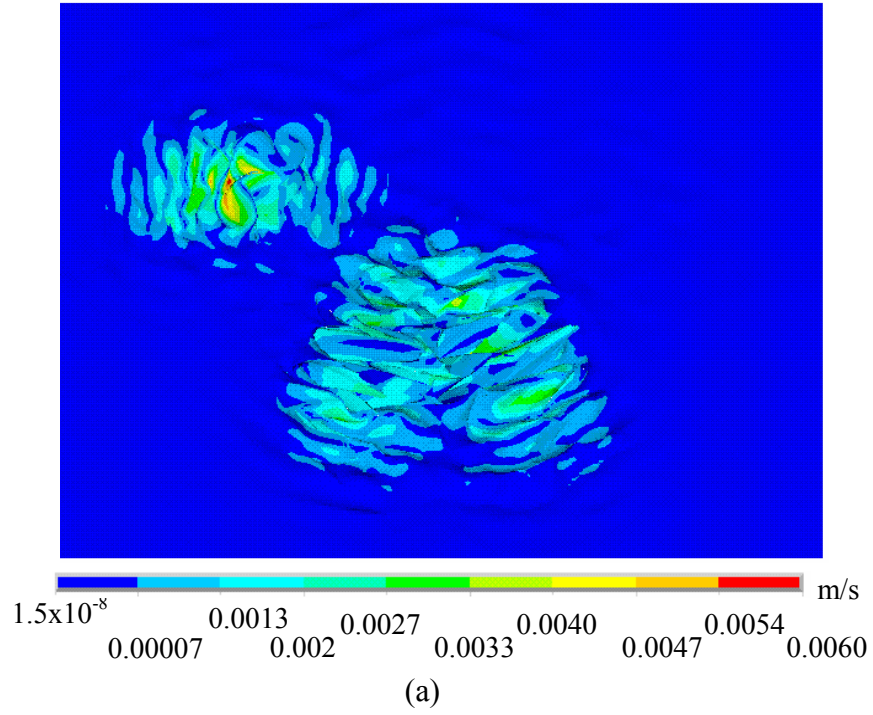


Figure 7.4: Velocity Profiles of the Fluid in Contact With the Surface of the SAW Device at Various Time Instants (a) 30 ns (b) 70 ns (c) 100 ns (d) 150 ns (e) 180 ns. The fluid-structure interface is shown here. Scale bar is in m/s.

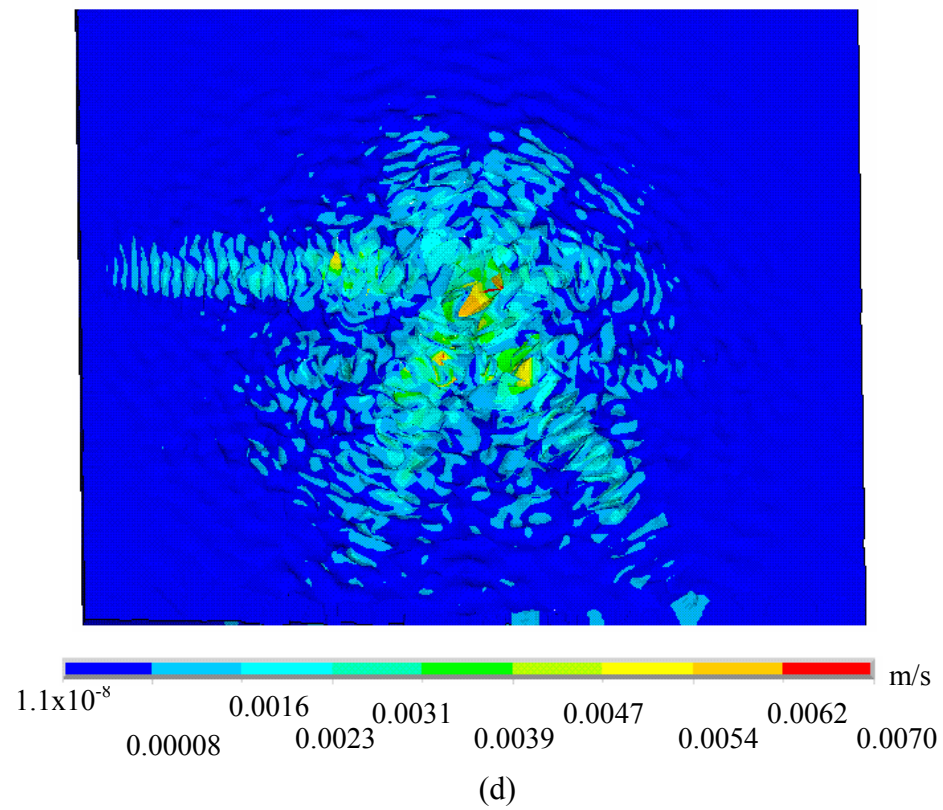
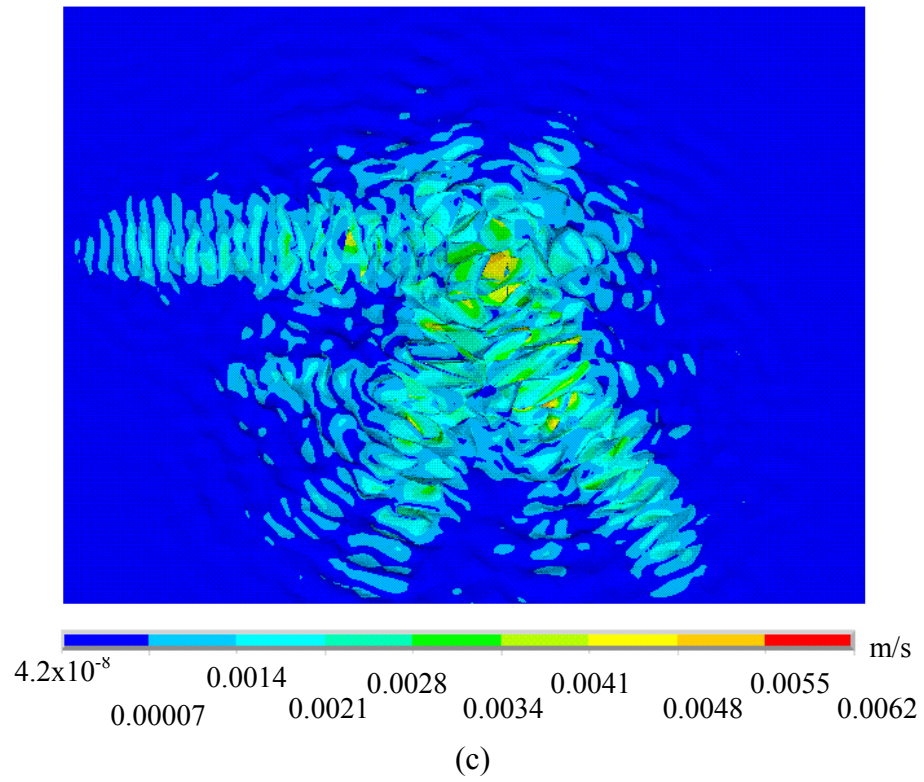
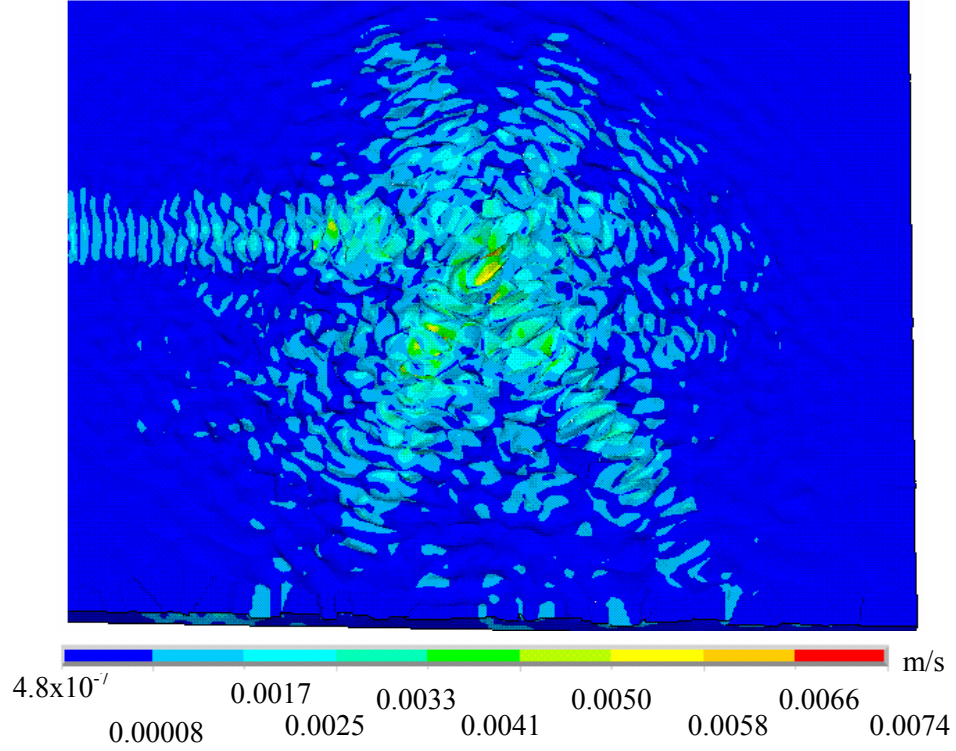


Figure 7.4: Continued.



(e)

Figure 7.4: Continued.

Bio-fouling elimination in the simulated SAW devices due to mixed mode waves propagating along $(0, 22, 0)$ Euler direction is dependent on the magnitude of the induced acoustic streaming forces computed as [124, 142]:

$$F = -\rho (1 + \alpha^2)^{3/2} A^2 \omega^2 \alpha k_i \exp 2(k_i x + \alpha k_i z) \quad (7-17)$$

Here, α and k_i refer to the attenuation constant and leaky SAW wave number, respectively, and are obtained using a perturbation approach [102, 103], ω refers to the angular frequency and A refers to the acoustic wave displacement, which are obtained using FE simulations.

In the presence of mutually interacting IDTs, such as the case in point, interference between the waves propagating in different Euler directions determine the nature of wave interaction [140, 159, 160]. Analysis of the phase difference between the wave propagating along

(0, 22, 0) and (0, 22, 90) directions in the mutually interacting transducer configuration reveals constructive interference between the them, thereby leading to an amplification of the device displacement amplitudes compared to a conventional device with U-IDTs.

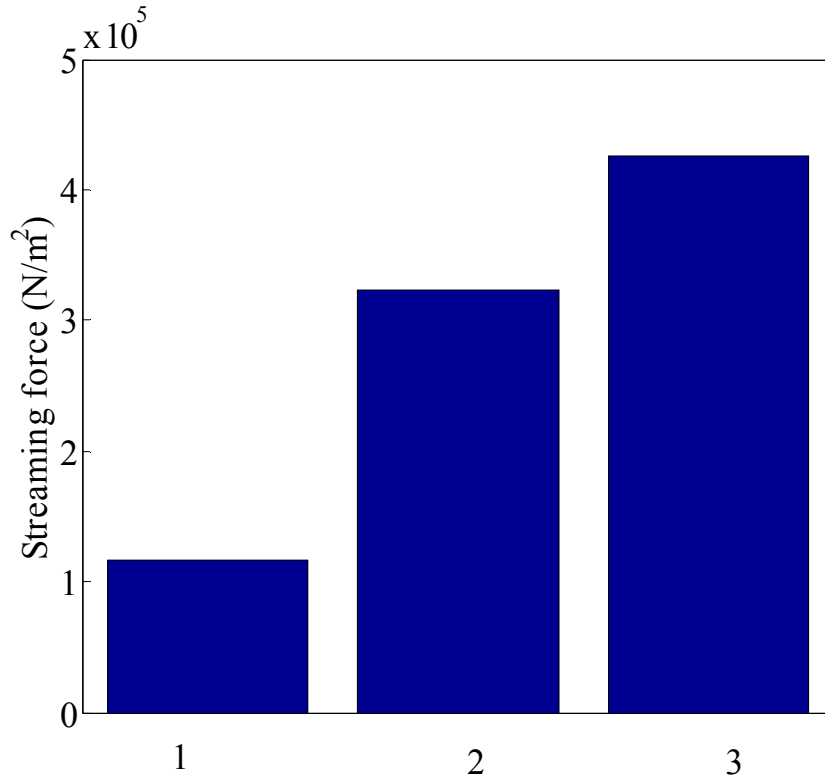


Figure 7.5: Streaming Forces on a Langasite Substrate Calculated Along the (0, 22, 0) Direction. These forces act to eliminate biofouling proteins from the device surface. Comparison of induced streaming forces for mutually interacting multidirectional (U-IDT/F-IDT) SAW with standard unidirectional SAW and orthogonal SAW with U-IDTs is shown. The term ‘uniform IDTs’ refers to single split uniform IDT configuration. (1) denotes standard unidirectional SAW device having U-IDTs along (0, 22, 0); (2) denotes orthogonal SAW device having mutually interacting U-IDTs along the (0, 22, 0) and (0, 22, 90) directions; (3) denotes orthogonal SAW device having mutually interacting U-IDTs along (0, 22, 90) and F-IDTs along (0, 22, 0) directions.

The amplification of the surface normal component, brought about by constructive wave interference, leads to a 266% and 31.7% increase in the amplitude of streaming force (4.2×10^5 N/m² for device with U-IDTs/F-IDTs design vs. 1.2×10^5 N/m² for device with standard unidirectional uniform IDTs vs. 3.2×10^5 N/m² for orthogonal SAW device with mutually interacting uniform IDTs) compared to a conventional device with unidirectional U-IDTs and an orthogonal SAW device with mutually interacting uniform IDTs, respectively as seen in Fig. 7.5. Thus, the simulation results indicate that the use of mutually interacting U-IDTs/F-IDTs on a Langasite substrate leads to an efficient sensor with increased device sensitivity and intensity of acoustic streaming compared to a device with uniform unidirectional IDTs.

7.4 Conclusion

To summarize, a Langasite based biosensor with mutually interacting F-IDT/U-IDT configuration is investigated for its applicability in biosensing applications while simultaneously cleaning the biofouling proteins. Mutually interacting U-IDTs/F-IDTs on a Langasite substrate are utilized to enhance device performance in biosensing applications by increasing the intensity of acoustic streaming forces for efficient biofouling removal and amplify the displacement/surface acoustic energy for increased device sensitivity. F-IDTs are used along (0, 22, 0) direction while U-IDTs are employed along the (0, 22, 90) direction in Langasite. The investigated device reflects a 32.4% higher sensitivity and 266% increase in the amplitude of streaming force compared to a device with unidirectional U-IDTs. The device also reflects almost comparable sensitivity and a 31.7% enhancement in the intensity of acoustic streaming compared to an orthogonal SAW device with uniform mutually interacting IDTs. Thus, the simulation results from the present work indicate that the use of mutually interacting U-IDTs/F-IDTs on a Langasite substrate leads to an efficient biosensor compared to a device with uniform unidirectional IDTs.

Chapter 8

Conclusions and Future Work

This dissertation focuses on the development of efficient SAW devices that allow for the integration of multiple functionalities on a single device and improved biosensing performance, *via* the use of novel transducer configurations and surface modifications such as micro-cavities. The main objective, in the context of this dissertation, is the development of a device that is capable of transducing nanogram to picogram/ml levels of target biomarker species, such as biomarkers for ovarian cancer, while simultaneously eliminating the NSB biofouling proteins that interfere with the sensing phenomenon, thereby enhancing the device sensitivity, selectivity, and speed of response. Novel transducer and device surface modifications are designed and employed in this work, to enhance the biosensor device performance in terms of sensitivity and acoustic streaming induced NSB protein removal. The current approach towards achieving the aforementioned goal is based on exploiting the capability of the piezoelectric crystal to launch waves of different characteristics in different crystallographic orientations owing to crystal anisotropy, which can be put to the multiple uses including but not limited to sensing and biofouling elimination on the same device, utilizing the shear horizontal waves and Rayleigh waves, respectively. The main contributions of this dissertation, to the scientific community, are summarized below. The findings of the present work have widespread and immediate use for enhancing sensor sensitivity and analyte discrimination capabilities as well as biofouling removal in medical diagnostic applications of SAW sensors. It has a broader impact on the sensing of multiple biomarkers in medical applications as well as chemical and environmental species

detection. The models developed and the simulation techniques used in the present work can be extended to a range of other applications of acoustic wave devices such as lab-on-a-chip systems involving microfluidic actuation and microvolume separation processes.

8.1 Contributions

The first part of this dissertation focuses on the development of a coupled three dimensional FSI FE model of SAW devices, to investigate wave propagation and fluid dynamics in SAW devices when in contact with a liquid loading, for typical microfluidic applications such as biosensing in bodily fluids. A three dimensional FE FSI model of a LiNbO₃ based SAW device in contact with fluid loading, is developed for the first time in this work, to study the acoustic wave interaction with the fluid media and gain insights into the acoustic streaming phenomenon. Analysis of the device displacement and fluid velocity profiles obtained from the developed FSI model indicates that the fluid domain couples strongly with the piezoelectric substrate, which leads to a leakage of acoustic energy into the fluid domain. This sound wave attenuation leads to the propagation of longitudinal waves in the fluid medium which, in turn, generate an acoustically driven phenomenon known as acoustic streaming. Fluid streaming velocities, computed as the time average of instantaneous fluid velocities over a time period, indicate fluid recirculation and are typically in the range of mm/s. Thus, the streaming velocity computed using the developed model is in accordance with the experimental values. Based on the device displacements and the streaming velocity profiles, various removal forces, namely the SAW streaming and hydrodynamic forces were computed to gain insights into the NSB biofouling proteins from the device surface. The developed three dimensional FSI FE model, of a SAW device with liquid loading, has broad applicability in understanding fluid motion and flow fields while accurately taking into account the structural dynamics of the piezoelectric substrate, in SAW applications involving their interaction with the fluid domain. The developed FSI FE model is extended

further, to investigate transducer configurations and device surface modifications that can enhance device sensitivity and microfluidic actuation capabilities.

In the next part of this dissertation, the suitability of langasite substrate for use in biosensing applications involving a fluid domain was analyzed using the three dimensional FE structural and FSI models. A novel design approach employing an orthogonal IDT configuration was explored to realize enhancements in device sensitivity and biofouling elimination capability. Specifically, the capability of langasite based SAW device to allow for the integration of dual functionality of biosensing and biofouling elimination on a single device was investigated by employing the devised orthogonal transducer configuration, using the developed FE structural and FSI models. Precise knowledge of the wave propagation characteristics and induced streaming phenomenon due to the developing flow fields, arising from the transient fluid-piezoelectric interaction, is provided by the developed 3-D models. The directions suitable for biosensing and biofouling elimination were identified by analyzing the wave propagation characteristics along different crystallographic orientations in langasite. Computations on langasite based orthogonal SAW device indicates different characteristics of waves propagating along various Euler directions. Whereas a pure shear horizontal wave was found to propagate along the (0, 22, 90) direction, rendering it suitable for biosensing, mixed modes with prominent surface normal component was found to propagate along the (0, 22, 0) direction making it suitable for potential application in removal of NSB proteins through acoustic streaming. Streaming velocity profiles were computed using the instantaneous fluid velocities for propagation along (0, 22, 0) direction. Mechanistic insights into biofouling elimination are deduced from the model, by comparing the van der Waal's adhesive force with the fluid induced hydrodynamic and the device induced SAW streaming removal forces on the non-specific protein particles. The computational modeling results on the orthogonal LGS based SAW device indicate the feasibility of incorporation of multiple functionalities on the same device, which can lead to

enhancement in device performance and have implications in improving device design, development of lab-on-chip systems, understanding biosensing mechanisms, and microfluidic actuation mechanisms in SAW devices.

The orthogonal transducer configurations were combined with delay path modifications on a langasite based SAW device to obtain enhanced biosensor performance and biofouling elimination capabilities. Using the developed three dimensional structural and FSI FE models, wave propagation, complex acoustic wave interactions, and fluid dynamics were investigated in a novel langasite based SAW biosensor with integrated mutually interacting multi-directional inter-digital transducers (IDT) and delay path modifications. Finite element simulations reveal that significant enhancements to sensor performance are realized from a combination of mutually interacting inter-digital transducers and micro-cavities of square cross-sections in the center of surface acoustic wave delay path. These enhancements are significantly larger than those realized by utilizing guiding layers and operating in the Love wave mode which represents the most commonly accepted method of enhancement. Current results indicate constructive interference between the propagating waves in mutually interacting, multidirectional IDT configuration on langasite leading to decreased power loss. The integration of surface modifications, such as polystyrene filled micro-cavities in the sensor delay path, with the mutually interacting orthogonal IDTs provides a synergistic effect owing to acoustic energy entrapment at the surface resulting in a further reduction in power consumption. Thus, integration of multidirectional mutually interacting IDT configuration with micro-cavities in the delay path enhances device biosensing performance *via* increased device sensitivity and reduced power loss as compared to a standard langasite based SAW device having unidirectional IDTs, while simultaneously allowing for non-specifically bound protein removal *via* acoustic streaming. The results lead us to believe that practical devices realized using these finite element results will yield superior surface acoustic wave sensors which consume less power and afford higher sensitivity than alternative

designs and also allow for simultaneous biofouling elimination. The results are of tremendous significance for not only improving the device design, but also for understanding biosensing mechanisms in multi-directional acoustic wave devices as well as actuation mechanisms in potential microfluidic applications of these devices.

Enhancements in acoustic streaming induced biofouling elimination were realized through the use of F-IDTs, employing the three dimensional FSI FE models developed in this work. The FSI simulation derived functional parameters such as device displacement amplitude, fluid velocity fields, and streaming forces for the F-SAW device are compared with those for the conventional SAW. Both, qualitative and quantitative differences in the aforementioned quantities are observed between the F-SAW and conventional SAW device. Using a representative example of streaming induced biofouling elimination in acoustic wave biosensor, it is shown that the acoustic energy focusing and streaming enhancement brought about by F-SAW device results in a significantly improved micro-transport which translates into higher biofouling removal efficiency of F-SAW compared to the conventional SAW device, thereby providing enhanced device sensitivity, selectivity and device re-usability. The results of this study have significant implications in biosensing and microfluidic applications like micro-dispensing to pico-dispensing. In a broader context, the results of the present study demonstrate a technique of enhancing streaming induced flows, which is of great importance to contemporary problems involving microfluidic and sensing applications of piezoelectric devices.

The ability of the F-SAW device to enhance acoustic streaming is exploited to design an efficient biosensor capable of simultaneous biosensing and NSB protein elimination via microfluidic actuation, on langasite substrate. Combined with the fact that the (0, 22, 0) direction in langasite allows for mixed mode propagation having surface normal component, the F-IDTs are used along this direction while conventional IDTs with uniform finger spacing are utilized along (0, 22, 90) Euler direction. The mutually interacting U-IDTs/F-IDTs transducer configuration is

found to enhance device biosensing performance by amplifying the displacement/surface acoustic energy for increased device sensitivity while simultaneously increasing the intensity of acoustic streaming forces for efficient biofouling removal. The amplification of device surface displacements is attributed to the constructive interference between the orthogonally propagating waves while the enhancement in biofouling elimination efficiency arises from the acoustic streaming enhancement owing to the focusing effect of the F-IDTs. The results from the finite element modes indicate a significant increase in device sensitivity and streaming induced biofouling elimination efficiency, compared to a device with U-IDTs.

To summarize, the current work has focused on the development of FSI FE models of SAW devices which provide a strong platform to understand the interaction of the fluid domain with the sensor surface in liquid sensing applications and also optimize sensor design for these applications. Significant improvements in the sensor performance are realized from the new multidirectional transducer configurations and sensor surface modifications in the form of micro-cavities, introduced in the present work, as demonstrated in biosensing applications within the scope of this project. The results are broadly applicable to various SAW applications requiring device operation in liquid media, such as microfluidic actuation or lab-on-chip systems.

8.2 Future Work

The models developed in the current work and understanding gained into the underlying physics of SAW device interaction with the fluid domain builds the framework for future work, especially in the area of microfluidic actuation using SAW devices. Using the groundwork laid down in this dissertation, improvements in the device designs can be made for various microfluidic applications of SAW devices. Some of the areas that merit investigation are discussed in this section.

8.2.1 Newtonian vs. Non-Newtonian Fluid Loading

Biosensing occurs in bodily fluids such as urine and blood. The acoustic streaming phenomenon depends on the fluid dynamical properties, namely the density and viscosity [161]. Newtonian fluids show a linear relationship between stress and strain, the slope of the curve being the fluid viscosity which is a constant. However, a Non-Newtonian fluid exhibits a shear rate dependent fluid viscosity and therefore a non-linear stress-strain relationship. Blood consists of multiple components namely red blood cells, platelets and white blood cells suspended in plasma consisting of proteins and water [162]. While blood plasma is Newtonian in nature, the red blood cells tend to form aggregates at low shear rates [163]. At high shear rates, these red blood cells lose their viscoelasticity [164], become ‘fluid like’, align themselves with the flow and tend to slide over the plasma layers. Thus, blood is a mixture of Newtonian plasma and non-Newtonian hematocrits, exhibiting shear thinning and viscoelastic behavior at low shear rates [165-167] owing to the changes in microstructure resulting from the aggregation, deformation, and alignment of the hematocrits. This behavior of blood is evident from the experimental viscosity measurements carried out at a wide range of shear rates [161]. In microfluidic channels, the non-Newtonian behavior of blood can be particularly important owing to the small dimensions to which it is confined, generating velocity profiles more characteristic of complex fluids. Therefore, in microfluidic applications, the rheological behavior of blood can be expressed using a non-Newtonian constitutive relation. A number of studies have utilized [168-170] the Carreau model to characterize blood rheology, given by [171]

$$\mu = \mu_{\infty} + (\mu_0 - \mu_{\infty}) \left[1 + \lambda D^2 \right]^{(n-1)/2} \quad (8-1)$$

μ_0 and μ_{∞} represent viscosities at zero and infinite shear rate, D denotes shear rate, λ is the time constant, and n represents power factor. The experimental data relating the viscosity of blood to the shear rate can be used to determine μ_0 , μ_{∞} , λ , and n.

Using the fluid-structure models developed in the current work, the influence of non-Newtonian behavior of blood on the acoustic streaming velocity fields can be investigated by comparison with results based on the assumption of Newtonian behavior of blood. The results from such a comparison will be beneficial for various applications that utilize acoustic streaming in blood, such as biomedical diagnostics and biosensing.

8.2.2 SAW Induced Ultrasonic Mixing and Micropumping

Mixing in very small fluid volumes is desirable in biomedical applications such as microarrays or lab on chip devices [172-177]. At the small length scales encountered in these microfluidic devices, the fluid flow is characterized by low Reynolds number which in turn renders the mixing process primarily diffusion controlled [178-182]. In recent years, efforts of the scientific community have been directed towards coupling microfluidic channels with SAWs to induce mixing in these channels [173, 183-185]. When a liquid droplet is placed in contact with a SAW device, acoustic streaming is induced. At small wave amplitudes, internal streaming takes place which can have a stirring effect and induce fluid mixing at the micro or nano scale. At larger wave amplitudes, bulk fluid actuation can take place, bringing about bulk transport leading to macro-mixing by advection. Such SAW based micropumps are of tremendous importance in various biological applications. One such example is DNA microarrays used in gene expression analysis. DNA hybridization assays, used for gene expression analysis, involve binding of fluorescently labeled sample molecules with probe spots of DNA in the arrays and an increase in the intensity of fluorescence of the spot is an indicator of successful hybridization. Such experiments typically utilize a very thin liquid film in which the flow is laminar and therefore molecule transport is primarily diffusion limited owing to the lack of convective transport. Thus, the accuracy of such processes is governed by microfluidic constraints and relies on reaction equilibrium at each DNA spot which might give misleading results if equilibrium is not reached.

Such processes can be accelerated considerably if advective transport of the molecules is achieved. SAW induced acoustic streaming, which induces fluid motion leading to the creation of a jet, can be used to achieve mixing within microfluidic channels. The fluid-structure interaction models developed in the current work can be readily extended to investigate velocity and pressure fields generated in microfluidic channels coupled with the SAW devices. The models can be used to gain insights into the translation of acoustic streaming into fluid velocity in such channels and design efficient microfluidic devices for various biomedical applications.

8.2.3 Droplet Generation

Liquid droplet based microfluidic systems are beginning to find extensive applicability in biological applications, such as carriers to target drug delivery to the intended diseased tissue, encapsulation agents for various biological entities, micro-reactors for rapid mixing and reaction of reagents, liquid reaction vessels for protein crystallization, biosensing, DNA analysis, sampling glucose concentrations in bodily fluids, to name a few [186-199]. In droplet based microfluidics, discrete droplets are created *via* the use of two immiscible phases in microchannels [200, 201]. All applications require a great control on droplet size, shape, and distribution; monodispersed droplets are typically required. Most of the microfluidic systems require manipulation of the externally applied pressure gradient to control particle size. SAW devices, with hydrophobically modified surfaces, can be utilized for efficient microfluidic control and droplet generation [202-205]. The Rayleigh wave generated in SAW devices impinges on the fluid medium and imparts momentum generating fluid motion known as acoustic streaming. The fluid induced shear force, in conjunction with the pressure difference can overcome the interfacial force, which leads to droplet detachment from the surface. The droplet size distribution depends on the velocity distribution in the SAW microfluidic system. Using the framework of the models developed in this dissertation, methods to design SAW microfluidic systems capable of providing

monodispersed droplets can be investigated. In this dissertation, we have discussed the role of micro-cavities in amplifying the device displacements and fluid velocities and its implications on biosensing. By extending the developed fluid-structure interaction models of SAW devices, the role of micro-cavities in SAW induced droplet generation and their size distribution merits investigation. Similarly, the use of focusing on droplet generation can be studied using the developed models.

8.2.4 Multilayered SAW devices Based on Nanocrystalline Diamond

The intensity of acoustic streaming in microfluidic applications of SAW devices depends on the device frequency, in addition to fluid properties. Researchers are constantly searching for new materials that can be used to enhance sensor performance. Nanocrystalline diamond films have gained tremendous importance in recent years owing to their wide applicability and attractive properties [206]. Although diamond by itself is not piezoelectric, diamond layers have also found increasing use in recent years as coating materials for SAW/MEMS devices. When used on SAW devices, diamond layers provide a dual advantage of improved transduction and device surface biofunctionalization [207, 208]. Diamond exhibits high Young's modulus, tensile strength, fracture strength, thermal conductivity, low coefficient of thermal expansion, good wear resistance, stability in extreme conditions, chemical inertness and a broad electrochemical range. Owing to its biocompatibility and stability in harsh environments, diamond can be used as an interface to biomolecules in biosensors [209-211]. In addition, diamond can be easily doped to enhance conductivity [212] and can be readily treated to render the surface hydrophobic or hydrophilic. The hydrophobicity of the device surface coated with diamond layer inhibits non-specific protein binding while the surface can still be photochemically treated to facilitate specific binding, thereby enhancing the biosensor selectivity and sensitivity. Furthermore, the high density of diamond allows for high acoustic wave propagation velocity and realizing high

frequency devices [213, 214] that can generate high SAW amplitudes and stronger acoustic streaming fields. Langasite, as a substrate for biosensing while allowing for simultaneous biofouling elimination *via* acoustic streaming, has already been investigated in this dissertation. The use of nanocrystalline diamond films on Langasite based SAW device is worthy of investigation and forms a part of the future work in the area of biosensors. The structural and three dimensional fluid-structure interaction finite element models of SAW devices developed herein can be extended to investigate multilayered diamond coated SAW devices based on Langasite, for evaluating the enhancement in device performance in terms of sensitivity, selectivity, and acoustic streaming intensity. Optimization of the diamond layer thickness can be carried using the finite element models.

The future work proposed in this section is expected to significantly advance the field of SAW microfluidics and lead to the development of improved SAW devices for various applications.

List of References

1. Franke, T., Abate, A.R., Weitz, D.A., and Wixforth, A., *Surface acoustic wave (SAW) directed droplet flow in microfluidics for pdms devices* Lab on a Chip, 2009. 10.1039/b906819h
2. Luo, J.K., Fu, Y.Q., Li, Y., Du, X.Y., Flewitt, A.J., Walton, A.J., and Milne, W.I., *Moving-part-free microfluidic systems for lab-on-a-chip* Journal of Micromechanics and Microengineering, 2009. 19: p. 054001/1-054001/14
3. Guttenberg, Z., Rathgeber, A., Keller, S., Raedler, J.O., Wixforth, A., Kostur, M., Schindler, M., and Talkner, P., *Flow profiling of a surface-acoustic-wave nanopump*. Physical Review E: Statistical, Nonlinear, and Soft Matter Physics, 2004. 70: p. 056311/1-056311/10.
4. Hadd, A.G., Raymond, D.E., Halliwell, J.W., Jacobson, S.C., and Ramsey, J.M., *Microchip device for performing enzyme assays*. Analytical Chemistry, 1997. 69: p. 3407-3412.
5. Hatch, A., Kamholz, A.E., Hawkins, K.R., Munson, M.S., Schilling, E.A., Weigl, B.H., and Yager, P., *A rapid diffusion immunoassay in a T-sensor*. Nature Biotechnology, 2001. 19: p. 461-465.
6. Länge, K., Blaess, G., Voigt, A., Rapp, M., Karlsruhe, F., Hansjosten, E., and Schyguilla, U., *Packaging of surface acoustic wave (SAW) based biosensors: An important issue for future biomedical applications*. Proceedings of the IEEE international Frequency Control Symposium and Exposition, 2004: p. 321-325.
7. Länge, K., Bender, F., Voigt, A., Gao, H., and Rapp, M., *A surface acoustic wave biosensor concept with low flow cell volumes for label free biodetection*. Analytical Chemistry, 2003. 75: p. 5561-5566.
8. Bennès, J., Alzuaga, S., Ballandras, S., Chérioux, F., Bastien, F., and Manceau, J.-F. *Droplet ejector using surface acoustic waves*. in *IEEE Ultrasonics symposium*. 2005. Rotterdam (Netherlands).

9. Alvarez, M., Friend, J., Yeo, L., and Arifin, D. *Microaerosol and nanoparticle synthesis for drug delivery via surface acoustic wave atomization*. in *16th Australian fluid mechanics conference*. 2007. Gold coast.
10. Fan, Z.H., S. Mangru, R. Granzow, P. Heaney, W. Ho, Dong, Q., and Kumar, R., *Dynamic DNA hybridization on a chip using paramagnetic beads*. *Analytical Chemistry*, 1999. 71: p. 4851-4859.
11. Galopin, E., Beaugeois, M., Pinchemel, B., Camart, J.-C., Bouazaoui, M., and Thomy, V., *Spr biosensing coupled to a digital microfluidic microstreaming system*. *Biosensors and Bioelectronics*, 2007. 23: p. 746-750.
12. Li, H., Friend, J.R., and Yeo, L.Y., *Microfluidic colloidal island formation and erasure induced by surface acoustic wave radiation*. *Physical Review Letters*, 2008. 101: p. 084502/1-084502/4.
13. Bennès, J., Alzuaga, S., Chabé, P., Morain, G., Chérioux, F., Manceau, J.-F., and Bastien, F., *Action of low frequency vibration on liquid droplets and particles*. *Ultrasonics*, 2006. 44: p. e497-e502
14. Sankaranarayanan, S.K.R.S. and Bhethanabolta, V.R., *Design of efficient focused surface acoustic wave devices for potential microfluidic applications*. *Journal of Applied Physics*, 2008. 103: p. 064518/1-064518/17.
15. Sankaranarayanan, S.K.R.S. and Bhethanabolta, V.R., *Finite-element modeling of a hexagonal surface acoustic wave device based on LiNbO₃ substrate*. *IEEE Sensors Journal*, 2009. 9: p. 329-339.
16. Sato, M., Moroishi, K., and Ishigami, S. *Filter and resonator using Langasite*. in *IEEE Frequency Control Symposium*. 1996. Honolulu, HI.
17. Silvestrova, I.M., Bezdekin, V.V., and Pisarevsky, Y.V., *New piezoelectric materials*. *Proceedings of the 1993 IEEE International Frequency Control Symposium 1993*: p. 351-352.
18. Silvestrova, I.M., Bezdelkin, V.V., Senyushenkov, P.A., and Pisarevsky, Y.V., *Present stage of La₃Ga₅SiO₁₄-research*. *Proceedings of the 1993 IEEE International Frequency Control Symposium, 1993*: p. 348-350.

19. Sakharov, S.A., Buzanov, N.A., Medvedev, A.V., Kondratiev, S.N., Girardet, E., and Thorvaldsson, T. *The analysis of non homogeneity of SAW velocity in Langasite*. in *IEEE International Frequency Control Symposium and PDA Exhibition*. 2001.
20. da Cunha, M.P., Malocha, D.C., Puccio, D.W., and Thiele, J., *LGX pure shear horizontal SAW for liquid sensor applications*. *Proceedings of IEEE Sensors*, 2002. 2: p. 1165-1170.
21. Kondratiev, S.N. and Thorvaldsson, T., *Influence of bulk wave excitation on performance of impedance element SAW filters realised on 36" And 42"- LiTaO₃ substrates*. *Proceedings of 1999 IEEE Ultrasonics Symposium*, 1999. 1: p. 317-320.
22. Hornsteiner, J., Born, E., Fischerauer, G., and Riha, E., *Surface acoustic wave sensors for high temperature applications*. *Proceedings of the 1998 IEEE International Frequency Control Symposium*, 1998: p. 615-620.
23. Mill, B.V. and Pisarevsky, Y.V., *Langasite-type materials: From discovery to present state*. *Proceedings of the 2000 IEEE/EIA International Frequency Control Symposium and Exhibition*, 2000. 1: p. 133–140.
24. da Cunha, M.P. and Fagundes, S.A., *Investigation on recent quartz-like materials for SAW applications*. *IEEE Transactions on Ultrasonics, Ferroelectrics, and Frequency Control*, 1999. 46: p. 1583–1590.
25. Thiele, J.A. and da Cunha, P.M., *High temperature LGS SAW gas sensor*. *Sensors and Actuators B: Chemical*, 2006. 113: p. 816-822
26. Krempl, P., Reiter, C., Wallnofer, W., and Neubig, J., *Temperature sensors based on GaPO₄*. *Proceedings of 2002 IEEE Ultrasonics Symposium*, 2002. 1: p. 949–952.
27. Honal, M., Fachberger, R., Holzheu, T., Riha, E., Born, E., Pongratz, P., and Bausewein, A., *Langasite surface acoustic wave sensors for high temperatures*. *Proceedings of the 2000 IEEE/EIA International Frequency Control Symposium and Exhibition*, 2000: p. 113–118.
28. Fritze, H., Tuller, H.L., Borchardt, G., and Fukuda, T., *High temperature properties of langasite*. *Proceedings of the Materials Research Society Symposium*, 2000. 604: p. 65–70.
29. Thiele, J.A. and da Cunha, P.M., *High temperature surface acoustic wave devices: Fabrication and characterization*. *Electronics Letters*, 2003. 39: p. 818–819.

30. Wang, S., Harada, J., and Uda, S., *A wireless surface acoustic wave temperature sensor using langasite as substrate material for high-temperature applications*. Japanese Journal of Applied Physics, 2003. 42: p. 6124–6127.
31. Scholl, G., Schmidt, F., Ostertage, T., Reindl, L., Scherr, H., and Wolff, W., *Wireless passive SAW sensor systems for industrial and domestic application*. Proceedings of the 1998 IEEE International Frequency Control Symposium, 1998: p. 595-601.
32. Reindl, L. *Wireless passive SAW identification marks and sensors*. in *2nd International Symposium of Acoustic Wave Devices for Future Mobile Communication Systems*. 2004. Chiba University.
33. Polh, A., *A review of wireless SAW sensors*. IEEE Transactions on Ultrasonics, Ferroelectrics and Frequency Control, 2000. 47: p. 317 - 332.
34. Ballantine, D.S., Martin, S.J., Ricco, A.J., Frye, G.C., White, R.M., and Zellers, E.T., *Acoustic wave sensors: Theory, design, and physico-chemical applications*. Applications of modern acoustics, ed. R. Stern and M. Levy. 1997, San Diego: Academic Press.
35. Shiokawa, S. and Kondoh, J., *Surface acoustic wave sensors*. Japanese Journal of Applied Physics, Part 1: Regular Papers, Short Notes & Review Papers, 2004. 43: p. 2799-2802.
36. Wu, S., Ro, R., and Lin, Z.-X., *Rayleigh surface acoustic wave modes of (100) ZnO films on (111) diamond*. Applied Physics Letters, 2009. 94: p. 032908/1-032908/3.
37. Wu, S., Ro, R., Lin, Z.-X., and Lee, M.-S., *Rayleigh surface acoustic wave modes of interdigital transducer/(100) AlN/(111) diamond*. Journal of Applied Physics, 2008. 104: p. 064919/1-064919/4.
38. Kosachev, V.V. and Gandurin, Y.N., *Rayleigh wave dispersion and attenuation on a statistically rough free surface of a hexagonal crystal*. Physics of the Solid State, 2003. 45: p. 391-399.
39. Calabrese, G.S., Wohltjen, H., and Roy, M.K., *Surface acoustic wave devices as chemical sensors in liquids. Evidence disputing the importance of Rayleigh wave propagation..* Analytical Chemistry, 1987. 59: p. 833-837.
40. Cheeke, J.D.N. and Morisseau, P., *Attenuation of Rayleigh waves on a lithium niobate(V) crystal in contact with a liquid helium-4 bath*. Journal of Low Temperature Physics, 1982. 46: p. 319-330.

41. Kondoh, J., Okiyama, Y., Mikuni, S., Matsui, Y., Nara, M., Mori, T., and Yatsuda, H., *Development of a shear horizontal surface acoustic wave sensor system for liquids with a floating electrode unidirectional transducer*. Japanese Journal of Applied Physics, 2008. 47: p. 4065-4069.
42. Shen, Y.-T., Huang, C.-L., Chen, R., and Wu, L., *A novel SH-SAW sensor system*. Sensors and Actuators B: Chemical, 2005. B107: p. 283-290.
43. Li, Z., Jones, Y., Hossenlopp, J., Cernosek, R., and Josse, F., *Analysis of liquid-phase chemical detection using guided shear horizontal-surface acoustic wave sensors*. Analytical Chemistry, 2005. 77: p. 4595-4603.
44. Hossenlopp, J., *Applications of acoustic wave devices for sensing in liquid environments*. Applied Spectroscopy Reviews, 2006. 41: p. 151-164.
45. Morita, T., Sugimoto, M., and Kondoh, J., *Measurements of standard-viscosity liquids using shear horizontal surface acoustic wave sensors*. Japanese Journal of Applied Physics 2009. 48: p. 07GG15/1-07GG15/4.
46. Gizeli, E., Lowe, C.R., Liley, M., and Vogel, H., *Detection of supported lipid layers with the acoustic love waveguide device: Application to biosensors*. Sensors and Actuators B 1996. 34: p. 295-300.
47. Josse, F., Bender, F., and Cernosek, R.W., *Guided shear horizontal surface acoustic wave sensors for chemical and biochemical detection in liquids*. Analytical Chemistry, 2001. 73: p. 5937-44.
48. Hoummady, M., Campitelli, A., and Wlodarski, W., *Acoustic wave sensors: Design, sensing mechanisms and applications*. Smart Materials and Structures, 1997. 6: p. 647-657.
49. Grate, J.W., Martin, S.J., and White, R.M., *Acoustic wave microsensors. Part I*. Analytical Chemistry, 1993. 65: p. 940A-948A.
50. Grate, J.W., Martin, S.J., and White, R.M., *Acoustic wave microsensors. Part II*. Analytical Chemistry, 1993. 65: p. 987A-996A.
51. Ballantine, D.S. and Wohltjen, H., *Surface acoustic wave devices for chemical analysis*. Analytical Chemistry, 1989. 61: p. 704A-15A.

52. Grate, J.W., Wenzel, S.W., and White, R.M., *Flexural plate wave devices for chemical analysis*. Analytical Chemistry, 1991. 63: p. 1552-61.
53. Fertier, L., Cretin, M., Rolland, M., Durand, J.O., Raehm, L., Desmet, R., Melnyk, O., Zimmermann, C., Déjous, C., and Rebière, D., *Love wave immunosensor for antibody recognition using an innovative semicarbazide surface functionalization* Sensors and Actuators B: Chemical, 2009. 140: p. 616-622.
54. Josse, F., Bender, F., Cernosek, R.W., and Zinszer, K., *Guided SH-SAW sensors for liquid-phase detection*. Proceedings of the 2001 IEEE International Frequency Control Symposium and PDA Exhibition 2001: p. 454 – 461.
55. Wessa, T., Rapp, M., and Ache, H.J., *New immobilization method for SAW-biosensors: Covalent attachment of antibodies via CNBr* Biosensors and Bioelectronics, 1999. 14: p. 93-98.
56. Barié, N. and M., R., *Covalent bound sensing layers on surface acoustic wave (SAW) biosensors*. Biosensors and Bioelectronics, 2001. 16: p. 979-987.
57. Kondoh, J., Matsui, Y., Shiokawa, S., and Wlodarski, W., *Enzyme immobilized SH-SAW biosensor*. Sensors and Actuators B: Chemical, 1994. 20: p. 199–203.
58. Barié, N., Rapp, M., and Ache, H.J., *UV crosslinked polysiloxanes as new coating materials for SAW devices with high long-term stability*. Sensors and Actuators B: Chemical, 1998. 46: p. 77-103.
59. Mitsakakis, K., Tserepi, A., and Gizeli, E., *Integration of microfluidics with a love sensor for the fabrication of a multisample analytical microdevice*. Journal of Microelectromechanical Systems, 2008. 17: p. 1010-1019.
60. Delamarche, E., Juncker, D., and Schmid, H., *Microfluidics for processing surfaces and miniaturizing biological assays*. Advanced Materials, 2005. 17: p. 2911–2933.
61. Länge, K., Blaess, G., Voigt, A., Götzen, R., and Rapp, M., *Integration of a surface acoustic wave biosensor in a microfluidic polymer chip*. Biosensors and Bioelectronics, 2006. 22: p. 227–232.
62. Situma, C., Hashimoto, M., and Soper, S.A., *Merging microfluidics with microarray-based bioassays*. Biomolecular Engineering, 2006. 23: p. 213–231.

63. Guttenberg, Z., Muller, H., Habermuller, H., Geisbauer, A., Pipper, J., Felbel, J., Kielpinski, M., Scriba, J., and Wixforth, A., *Planar chip device for PCR and hybridization with surface acoustic wave*. Lab on a Chip, 2005. 5: p. 308–317.
64. Nyborg, W.L., *Acoustic streaming near a boundary*. Journal of Acoustical Society of America, 1953. 30: p. 329–339.
65. Rayleigh, L., *On the circulation of air observed in Kundt's tubes*. Philosophical Transactions of the Royal Society of London, 1884. A175: p. 1–21.
66. Nyborg, W.L., *Acoustic streaming due to attenuated plane waves*. Journal of Acoustical Society of America, 1953. 25: p. 68–75.
67. Qi, Q., Johnson, R.E., and Harris, J.G., *Boundary layer attenuation and acoustic streaming accompanying plane-wave propagation in a tube*. Journal of Acoustical Society of America, 1995. 97: p. 1499–1509.
68. Milton, A.J. and Ingard, U., *Acoustic streaming at high reynolds numbers*. Journal of Acoustical Society of America, 1953. 25: p. 928-933.
69. Kogai, T. and Yatsuda, H. *Liquid sensor using SAW and SH-SAW on quartz*. in *IEEE Ultrasonics Symposium*. 2006.
70. Gerhard, L., *Sensors and actuators based on surface acoustic waves propagating along solid-liquid interfaces*. Journal of Physics D: Applied Physics, 2008. 41: p. 123002/1-123002/13.
71. Bertoni, H.L. and Tamir, T., *Unified theory of Rayleigh-angle phenomena for acoustic beams at liquid-solid interfaces* Applied Physics A: Materials Science and Processing, 1973. 2: p. 157-172.
72. Frampton, K.D., Minor, K., and Martin, S.E., *Acoustic streaming in micro-scale cylindrical channels*. Applied Acoustics, 2004. 11: p. 1121-1129
73. Lighthill, J., *Acoustic streaming*. Journal of Sound and Vibration, 1978. 61: p. 391-418.
74. Byoung-Gook, L., Dong-Ryul, L., and Kwon, K., *Acoustic streaming pattern induced by longitudinal ultrasonic vibration in an open channel using particle imaging velocimetry*. Applied physics letters, 2006. 89: p. 183505.

75. Chono, K., Shimuzu, N., Matsui, Y., Kondoh, J., and Shiokawa, S., *Development of novel atomization system based on SAW streaming*. Japanese Journal of Applied Physics, 2004. 43: p. 2987-2991.
76. Zhang, G.-J., Hashimoto, K.-y., and Yamaguchi, M., *Liquid streaming by high frequency ultrasonic waves*. Japanese Journal of Applied Physics, 1996. 35: p. 3248-3250.
77. Tseng, W., Lin, J., Sung, W., Chen, S., and Lee, G., *Active micro-mixers using surface acoustic waves on Y-cut 128° LiNbO₃*. Journal of Micromechanics and Microengineering, 2006. 16 p. 539-548.
78. Francis, L.A., Friedt, J.M., Zhou, C., and Bertrand, P., *In situ evaluation of density, viscosity, and thickness of adsorbed soft layers by combined surface acoustic wave and surface plasmon resonance*. Analytical Chemistry, 2006. 78: p. 4200–4209.
79. Squires, T.M. and Quake, S.R., *Microfluidics: Fluid physics at the nanoliter scale*. Reviews of Modern Physics, 2005. 77: p. 977 - 1026
80. Wixforth, A., *Acoustically driven planar microfluidics*. Superlattices and Microstructures, 2003. 33: p. 389-396
81. Kurosawa, M., Watanabe, T., Futami, A., and Higuchi, T., *Surface acoustic wave atomizer*. Sensors and Actuators A: Physical, 1995. 50: p. 69-74.
82. Murochi, N., Sugimoto, M., Matsui, Y., and Kondoh, J., *Deposition of thin film using a surface acoustic wave device*. Japanese Journal of Applied Physics, 2007. 46: p. 4754-4759
83. Rife, J.C., Bella, M.I., Horwitz, J.S., Kablera, M.N., Auyeungb, R.C.Y., and Kimb, W.J., *Miniature valveless ultrasonic pumps and mixers*. Sensors and Actuators A: Physical, 2000. 86: p. 135-140.
84. Frampton, K.D., Martin, S.E., and Minor, K., *The scaling of acoustic streaming for application in micro-fluidic devices*. Applied Acoustics, 2003. 64: p. 681-692
85. Yang, Z., Goto, H., Matsumoto, M., and Maeda, R. *Ultrasonic micromixer for microfluidic systems*. in *Micro Electro Mechanical Systems*. 2000.

86. Chen-Yi, L., Yen-Heng, L., and Gwo-Bin, L., *A droplet -based microfluidic system capable of droplet formation and manipulation*. *Microfluidics and Nanofluidics*, 2009. 6: p. 599-610.
87. Beyssen, D., Brizoual, L.L., Elmazria, O., and Alnot, P., *Microfluidic device based on surface acoustic wave*. *Sensors and Actuators B: Chemical*, 2006. 118: p. 380-385
88. Bennès, J., Alzuaga, S., Chérioux, F., Ballandras, S., Vairac, P., Manceau, J.-F., and Bastien, F., *Detection and high-precision positioning of liquid droplets using SAW systems*. *IEEE Transactions on Ultrasonics, Ferroelectrics and Frequency Control*, 2007. 54: p. 2146 - 2151.
89. Tabeling, P., *A brief introduction to slippage, droplets and mixing in microfluidic systems*. *Lab on a Chip*, 2009. 9: p. 2428-2436.
90. Gregorya, C.M., Hatfielda, J.V., Higginsa, S., Iacovidesb, H., and Vadgamac, P.J., *A novel open flow microflow sensor for reduced fouling of chemical sensors in physiological sampling environments*. *Sensors and Actuators B: Chemical* 2000. 65: p. 305-309.
91. Steinitz, M., *Quantitaion of the blocking effect of tween 20 and bovine serum albumin in elisa microwells*. *Analytical Biochemistry*, 2000. 282: p. 232–238.
92. Chen, R.J., Bangsaruntip, S., Drouvalakis, K.A., Kam, N.W.S., Shim, M., Li, Y., Kim, W., Utz, P.J., and Dai, H., *Noncovalent functionalization of carbon nanotubes for highly specific electronic biosensors*. *Proceedings of the National Academy of Sciences*, 2003. 100: p. 4984–4989.
93. Kenna, J.G., Major, G.N., and Williams, R.S., *Methods for reducing non-specific antibody binding in enzyme-linked immunosorbent assays*. *Journal of Immunological Methods*, 1985. 85: p. 409–419.
94. Brogan, K.L., Shin, J.H., and Schoenfisch, M.H., *Influence of surfactants and antibody immobilization strategy on reducing nonspecific protein interactions molecular recognition force microscopy*. *Langmuir*, 2004. 20: p. 9729-9735.
95. Engvall, E. and Perlmann, P., *Enzyme-linked immunosorbent assay, ELISA III. Quantitation of specific antibodies by enzyme-labeled anti-immunoglobulin in antigen-coated tubes*. *Journal of Immunology*, 1972. 109: p. 129-135.

96. Wakayama, J., Sekiguch, H., Akanuma, S., Ohtani, T., and Sugiyama, S., *Methods for reducing nonspecific interaction in antibody–antigen assay via atomic force microscopy* Analytical Biochemistry, 2008. 380: p. 51-58
97. Kovacs, G., Vellekoop, M.J., Haueis, R., Lubking, G.W., and Venema, A., *A love wave sensor for (bio)chemical sensing in liquids.* . Sensors and Actuators A: Physical, 1994. 43: p. 38-43
98. Kovacs, G. and Venema, A., *Theoretical comparison of sensitivities of acoustic shear wave modes for (bio)chemical sensing in liquids.* Applied Physics Letters, 1992. 61: p. 639-641.
99. Cular, S., Branch, D.W., Bhethanabotla, V.R., Meyer, G.D., and Craighead, H.G., *Removal of nonspecific binding on microsensors using surface acoustic waves.* IEEE Sensors Journal 2008. 8: p. 314-320.
100. Cular, S., Branch, D.W., Bhethanabotla, V.R., Meyer, G.D., and Craighead, H.G., *Removal of nonspecific binding on microsensors using surface acoustic waves,* in *AICHE Annual Meeting.* . 2005: Cincinnati, OH.
101. Cular, S., Branch, D.W., Meyer, G.D., and Bhethanabotla, V.R., *Acoustic manipulation of biological samples for improved sensors.,* in *AICHE Annual Meeting.* 2005: Cincinnati, OH. p. 526c/1-526c/8.
102. Campbell, J.J. and Jones, W.R., *A method for estimating optimal crystal cuts and propagation directions for excitation of piezoelectric surface waves.* IEEE Transactions on Sonics and Ultrasonics, 1968. 15: p. 209-217.
103. Campbell, J.J. and Jones, W.R., *Propagation of surface waves at the boundary between a piezoelectric crystal and a fluid medium.* IEEE Transactions on Sonics and Ultrasonics, 1970. 17: p. 71-76.
104. Chono, K., Shimizu, N., Matsui, Y., Kondoh, J., and Shiokawa, S., *Novel atomization method based on SAW streaming.* 2003 IEEE Symposium on Ultrasonics, 2003. 2: p. 1786-1789.
105. Uchida, T., Suzuki, T., and Shiokawa, S., *Investigation of acoustic streaming excited by surface acoustic waves.* Proceedings of 1995 IEEE Ultrasonics Symposium, 1995. 2: p. 1081-1084.

106. Xue, T., Lord, W., and Udpa, S., *Finite element simulation and visualization of leaky Rayleigh waves for ultrasonic NDE*. IEEE Transactions on Ultrasonics, Ferroelectrics and Frequency Control, 1997. 44: p. 557-564.
107. Olson, L.G., *Finite element model for ultrasonic cleaning*. Journal of Sound and Vibration, 1988. 126: p. 387-405.
108. Nguyen, N.T. and White, R.M., *Design and optimization of an ultrasonic flexural plate wave micropump using numerical simulation*. Sensors and Actuators A, 1999. 77: p. 229-236.
109. Furukawat, S., Nomuraz, T., and Yasudaz, T., *Characteristic features of leaky surface acoustic waves propagating on liquid/piezoelectric film/glass structures*. Journal of Physics D: Applied Physics, 1991. 24: p. 706713.
110. Sankaranarayanan, S.K.R.S., Cular, S., Bhethanabotla, V.R., and Joseph, B., *Flow induced by acoustic streaming on surface-acoustic-wave devices and its application in biofouling removal: A computational study and comparisons to experiment*. Physical Review E, 2008. 77: p. 066308/1-19.
111. Hughes, T.J.R., *The finite element method: Linear static and dynamic finite element analysis*. 1987, New Jersey: Prentice Hall, Inc.
112. Allik, H. and Hughes, T.J.R., *Finite element for piezoelectric vibration*. International Journal Numerical Methods of Engineering, 1970. 2: p. 151-157.
113. Shiokawa, S., Matsui, Y., and Moriizumi, T., *Experimental study on liquid streaming by SAW*. Japanese Journal of Applied Physics, 1989. 28: p. 126-128.
114. Olson, L.G., Journal of of Sound and Vibration 1988. 126: p. 387-405.
115. Nguyen, N.T. and White, R.M., *Acoustic streaming in micro-machined flexural plate wave devices: Numerical simulation and experimental verification*. IEEE Transactions on Ultrasonics, Ferroelectrics, and Frequency control 2000. 47: p. 1463-1471.
116. *Ansi/ieee standard on piezoelectricity (IEEE standard)*. 1988, New York: The Institute of Electrical and Electronics Engineers. 1-66.

117. Ippolito, S.J., Kalantar-Zadeh, K., Powell, D.A., and Wlodarski, W. *A 3-dimensional finite element approach for simulating acoustic wave propagation in layered SAW devices*. . in *Ultrasonics, IEEE Symposium*, . 5-8 Oct. 2003.
118. Ippolito, S.J., Kalantar-zadeh, K., Powell, D.A., and Wlodarski, W. *A finite element approach for 3-dimensional simulation of layered acoustic wave transducers*. in *Optoelectronic and Microelectronic Materials and Devices*. 11-13 Dec. 2002.
119. Ippolito, S.J., Kalantar-zadeh, K., Wlodarski, W., and Matthews, G.I. *The study of ZnO/XY LiNbO₃/sub 3/ layered SAW devices for sensing applications*. . in *IEEE Sensors*. 22-24th Oct, 2003.
120. Hughes, T.J.R., Liu, W.K., and Zimmermann, T.K., *Lagrangian-Eulerian finite element formulation for incompressible viscous flows*. *Computer Methods in Applied Mechanics and Engineering*, 1981. 29: p. 329-349.
121. Donea, J., Giuliani, S., and Halleux, J.P., *An arbitrary Lagrangian Eulerian finite element method for transient dynamic fluid structure analysis*. . *Computer Methods in Applied Mechanics*, 1982. 33: p. 689-723.
122. Nyborg, W., *Acoustic streaming* 1965, New York: Academic Press.
123. Aktas, M.K. and Farouka, B., *Numerical simulation of acoustic streaming generated by finite-amplitude resonant oscillations in an enclosure*. *Journal of Acoustical Society of America*, 2004. 116: p. 2822 -2831.
124. Shiokawa, S., Matsui, Y., and Ueda, T., *Study on SAW streaming and its application to fluid devices*. *Japanese Journal of Applied Physics*, 1990. 29: p. 137-139.
125. Moroney, R., *Ph.D. Thesis: Ultrasonic microtransport* University of California, Berkeley. 1995, Berkeley: University of California.
126. Moroney, R.M., White, R.M., and Howe, R.T., *Fluid motion produced by ultrasonic lamb waves*. *Proceedings of IEEE 1990 Ultrasonics symposium*, 1990. 1: p. 355-358.
127. Moroney, R.M., White, R.M., and Howe, R.T., *Microtransport induced by ultrasonic lamb waves*. *Applied Physics Letters*, 1991. 59: p. 774-776.

128. Singh, R., Sankaranarayanan, S.K.R.S., and Bhethanabotla, V.R., *Fluid-structure interaction model of surface acoustic wave biosensor.*, in *AICHE Annual Meeting*. 2008: Philadelphia, PA.
129. Singh, R., Sankaranarayanan, S.K.R.S., and Bhethanabotla, V.R., *Three dimensional fluid-structure interaction finite element model of wave propagation in SAW device: Application to bio-fouling removal*, in *AICHE Annual Meeting*. 2008: Philadelphia, PA.
130. Singh, R., Sankaranarayanan, S.K.R.S., and Bhethanabotla, V.R., *A novel three dimensional fluid-structure interaction finite element model of wave propagation in SAW device: Application to biosensing & microfluidics.*, in *IEEE Sensors Conference*. 2009: Christchurch, New Zealand.
131. Mitchell, P., *A perspective on protein microarrays*. *Nature Biotechnology*, 2002. 20: p. 225-229.
132. Ogi, H., Nakamura, N., Sato, K., Hirao, M., and Uda, S., *Elastic, anelastic, and piezoelectric coefficients of Langasite: Resonance ultrasound spectroscopy with laser doppler interferometry*. *IEEE Transactions on Ultrasonics Ferroelectrics and Frequency Control*, 2003. 50: p. 553-560.
133. *Ansys user manual, v11.0, ansys inc, Canonsburg, PA.*
134. Cular, S., Sankaranarayanan, S.K.R.S., and Bhethanabotla, V.R., *Enhancing effects of microcavities on shear horizontal surface acoustic wave sensors: A finite element simulation study*. *Applied Physics Letters*, 2008. 92: p. 244104/1 - 244104/3.
135. Singh, R. and Bhethanabotla, V.R., *Orthogonal SAW device based on langasite for simultaneous biosensing and biofouling removal: A fluid structure interaction study.*, in *AICHE Annual Meeting*. 2009: Nashville, TN
136. McHale, G., Newton, M., and Martin, F., *Theoretical mass sensitivity of love wave and layer guided acoustic plate mode sensors* *Journal of Applied Physics*, 2002. 91: p. 9701-9710.
137. Morgan, D.P., *Surface-wave devices for signal processing*. 1991, New York: Elsevier.
138. da Cunha, M.P., Malocha, D.C., Puccio, D.R., Thiele, J., and Pollard, T.B., *LGX pure shear horizontal SAW for liquid sensor applications*. *IEEE Sensors Journal*, 2003. 3: p. 554-561.

139. Singh, R., Sankaranarayanan, S.K.R.S., and Bhethanabotla, V.R., *Orthogonal surface acoustic wave device based on Langasite for simultaneous biosensing and bio-fouling removal*. Applied Physics Letters, 2009. 94: p. 263503/1-263503/3.
140. Singh, R., Sankaranarayanan, S.K.R.S., and Bhethanabotla, V.R., *Enhanced surface acoustic wave biosensor performance via delay path modifications in mutually interacting multidirectional transducer configuration: A computational study*. Applied Physics Letters, 2009. 95: p. 034101/1-034101/3.
141. Singh, R., Sankaranarayanan, S.K.R.S., and Bhethanabotla, V.R., *Micro-cavity induced acoustic streaming enhancement in a surface acoustic wave device based on Langasite.*, in *AICHE Annual Meeting*. 2009: Nashville, TN.
142. Kondoh, J., Shimizu, N., Matsui, Y., and Shiokawa, S., *Liquid heating effects by SAW streaming on the piezoelectric substrate*. IEEE transactions on ultrasonics, ferroelectrics, and frequency control, 2005. 52: p. 1881-1883.
143. Abdollahi, A., Zhongwei, J., and Arabshahi, S.A., *Evaluation on mass sensitivity of SAW sensors for different piezoelectric materials using finite-element analysis*. IEEE Transactions on Ultrasonics, Ferroelectrics and Frequency Control, 2007. 54: p. 2446-2455.
144. Mitsakakis, K., Tserepi, A., and Gizeli, E., *SAW device integrated with microfluidics for array-type biosensing*. Microelectronic Engineering, 2009. 86: p. 1416-1418.
145. Yaralioglu, G.G., Wygant, I.O., Marentis, T.C., and Khuri-Yakub, B.T., *Ultrasonic mixing in microfluidic channels using integrated transducers*. Analytical Chemistry, 2004. 76: p. 3694-3698.
146. Gregory, C.M., Hatfielda, J.V., Higginsa, S., Iacovidesb, H., and Vadgamac, P.J., *A novel open flow microflow sensor for reduced fouling of chemical sensors in physiological sampling environments*. Sensors and Actuators B: Chemical 2000. 65: p. 305-309.
147. Sankaranarayanan, S.K.R.S., Cular, S., and Bhethanabotla, V.R., *Predicting the mechanism of removal of nonspecifically bound proteins in a surface acoustic wave biosensor: A fluid-solid interaction study*. 2008 IEEE Sensors, 2008: p. 1456-1459.
148. Cohen, M.G., *Optical study of ultrasonic diffraction and focusing in anisotropic media*. Journal of Applied Physics, 1967. 38: p. 3821.

149. de Lima, J.M.M., Alsina, F., Seidel, W., and Santo, P.V., *Focusing of surface-acoustic-wave fields on (100) GaAs surfaces*. Journal of Applied Physics., 2003. 94: p. 7848-7856.
150. Kharusi, M.S. and Farnell, G.W., *On diffraction and focusing in anisotropic crystals*. Proceedings of the IEEE 1972. 60: p. 945-956.
151. Marynowski, T.J., *Focusing transducer for SAW beamwidth compression on YZ Lithium Niobate*. 1982 IEEE Ultrasonics Symposium, 1982 p. 160–165.
152. Wu, T.-T., Tang, H.-T., and Chen, Y.-Y., *Frequency response of a focused SAW device based on concentric wave surfaces: Simulation and experiment*. Journal of Physics D: Applied Physics, 2005. 38: p. 2986.
153. Qi, Q. and Brereton, G.J., *Mechanisms of removal of micron-sized particles by high frequency ultrasonic waves*. IEEE Transactions on Ultrasonics, Ferroelectrics and Frequency Control. , 1995. 42: p. 619-629.
154. Israelachvili, J., *Intermolecular and surface forces*. 1992, London: Academic Press Inc.
155. King, L.V., *On the acoustic radiation pressure on spheres*. Proceedings of Royal Society of London, Series A, 1934. 147: p. 212.
156. Singh, R., Sankaranarayanan, S.K.R.S., and Bhethanabotla, V.R., *Enhancement of acoustic streaming induced flow on a focused SAW device: Implications for biosensing and microfluidics.*, in *AICHE Annual Meeting*. 2008: Philadelphia, PA.
157. Singh, R., Sankaranarayanan, S.K.R.S., and Bhethanabotla, V.R., *Enhancement in ultrasonic micro-transport using focused inter-digital transducers in a surface acoustic wave device: Fluid-structure interaction study.*, in *IEEE Sensors Conference*. 2009: Christchurch, New Zealand.
158. *Ansys user manual, v12.0*, Ansys Inc, Canonsburg, PA.
159. Singh, R., Sankaranarayanan, S.K.R.S., and Bhethanabotla, V.R., *Integrated focused and conventional transducer configuration on a single piezoelectric device for simultaneous biosensing and biofouling removal.*, in *AICHE Annual Meeting*. 2009: Nashville, TN.
160. Singh, R. and Bhethanabotla, V.R., *Design of mutually interacting multi-directional transducer configurations on a surface acoustic wave device for enhanced biosensing.*, in *IEEE Sensors Conference*. 2009: Christchurch, New Zealand.

161. Shi, X., Martin, R.W., Vaezy, S., and Crum, L.A., *Quantitative investigation of acoustic streaming in blood*. Journal of Acoustical Society of America, 2002. 111: p. 1110-1121.
162. Anand, M. and Rajagopal, K.R., *A shear-thinning viscoelastic fluid model for describing the flow of blood*. International Journal of Cardiovascular Medicine and Science, 2004. 4: p. 59-68.
163. Chien, S., Usami, S., Dellenback, R.J., and Gregersen, M.I., *Blood viscosity: Influence of erythrocyte aggregation*. Science, 1967. 157: p. 829-831.
164. Chien, S., Usami, S., Dellenback, R.J., and Gregersen, M.I., *Blood viscosity: Influence of erythrocyte deformation*. Science, 1967. 157: p. 827-829.
165. Thurston, G.B., *Viscoelasticity of human blood*. Biophysics Journal, 1972. 12: p. 1205-121.
166. Thurston, G.B., *Rheological parameters for the viscosity, viscoelasticity, and thixotropy of blood*. Biorheology, 1979. 16: p. 149-162.
167. Thurston, G.B., *Frequency and shear rate dependence of viscoelasticity of human blood*. Biorheology, 1973. 10: p. 375-38.
168. Chen, J. and Lu, X.-Y., *Numerical investigation of the non-Newtonian pulsatile blood flow in a bifurcation model with a non-planar branch*. Journal of Biomechanics, 2006. 39: p. 818-832.
169. Gijssen, F.J.H., van de Vosse, F.N., and Janssen, J.D., *The influence of the non-Newtonian properties of blood on the flow in large arteries: Steady flow in a carotid bifurcation model*. Journal of Biomechanics, 1999. 32: p. 601-608.
170. Gijssen, F.J.H., van de Vosse, F.N., and Janssen, J.D., *The influence of the non-Newtonian properties of blood on the flow in large arteries: Unsteady flow in a 90° curved tube*. Journal of Biomechanics, 1999. 32: p. 705-713.
171. Carreau, P.J., Chhabra, R.P., and De Kee, D.C.R., *Rheology of polymeric systems: Principles and applications*. 1997, Cincinnati, OH: Hanser-Garner Publications.
172. Yuen, P.K., Li, G., Bao, Y., and Muller, U.R., *Microfluidic devices for fluidic circulation and mixing improve hybridization signal intensity on DNA arrays*. Lab on a Chip, 2003. 3: p. 46-50.

173. Du, X.Y., Swanwick, M.E., Fu, Y.Q., Luo, J.K., Flewitt, A.J., Lee, D.S., Maeng, S., and Milne, W.I., *Surface acoustic wave induced streaming and pumping in 128° y-cut LiNbO₃ for microfluidic applications*. Journal of Micromechanics and Microengineering, 2009. 19: p. 035016/1-035016/10.
174. Liu, R.H., Dill, K., Fuji, H.S., and Andy, M., *Integrated microfluidic biochips for DNA microarray analysis*. Expert Review of Molecular Diagnostics, 2006. 6: p. 253-261.
175. Pfeil, S.H., Wickersham, C.E., Hoffmann, A., and Lipman, E.A., *A microfluidic mixing system for single-molecule measurements*. Review of Scientific Instruments 2009. 80: p. 055105/1-055105/9.
176. ane, A.S., Hoffmann, A., Baumgartel, P., Seckler, R., Reichardt, G., Horsley, D.A., Schuler, B., and Bakajin, O.M., *Microfluidic mixers for the investigation of rapid protein folding kinetics using synchrotron radiation circular dichroism spectroscopy*. Analytical Chemistry, 2008. 80: p. 9534-9541.
177. Cretich, M., G.C., D., Giudici, C., Pokoj, S., Lauer, I., Scheurer, S., and Chiari, M., *Detection of allergen specific immunoglobulins by microarrays coupled to microfluidics*. Proteomics, 2009. 9: p. 2098-2107.
178. Locascio, L.E., *Microfluidic mixing*. Analytical and Bioanalytical Chemistry 2004. 379: p. 325-327.
179. Sritharan, K., Strobl, C.J., Schneider, M.F., and Wixforth, A., *Acoustic mixing at low Reynold's numbers*. Applied Physics Letters, 2006. 88: p. 054102/1-054102/3.
180. Glasgow, I. and Aubry, N., *Enhancement of microfluidic mixing using time pulsing*. Lab on a Chip, 2003. 3: p. 114-120.
181. Oberti, S., Neild, A., and Ng, T.W., *Microfluidic mixing under low frequency vibration*. Lab on a Chip, 2009. 9: p. 1435-1438.
182. Wang, S.S., Jiao, Z.J., Huang, X.Y., Yang, C., and Nguyen, N.T., *Acoustically induced bubbles in a microfluidic channel for mixing enhancement*. Microfluidics and Nanofluidics, 2009. 6: p. 847-852.
183. Shilton, R., Tan, M.K., Yeo, L.Y., and Friend, J.R., *Particle concentration and mixing in microdrops driven by focused surface acoustic waves*. Journal of Applied Physics, 2008. 104: p. 014910/1-014910/9.

184. Haeberle, S. and Zengerle, R., *Microfluidic platforms for lab-on-a-chip applications*. Lab on a Chip 2007. 7: p. 1094-1110.
185. Frommelt, T., Kostur, M., Wenzel-Schafer, M., Talkner, P., Hanggi, P., and Wixforth, A., *Microfluidic mixing via acoustically driven chaotic advection*. Physical Review Letters, 2008. 100: p. 034502/1-034502/4.
186. Mazutis, L., Araghi, A.F., Miller, O.J., Baret, J.-C., Frenz, L., Janoshazi, A., Taly, V., Miller, B.J., Hutchison, J.B., Link, D., Griffiths, A.D., and Ryckelynck, M., *Droplet-based microfluidic systems for high-throughput single DNA molecule isothermal amplification and analysis*. Analytical Chemistry, 2009. 81: p. 4813-4821.
187. Teh, S.Y., Lin, R., Hung, L.H., and Lee, A.P., *Droplet microfluidics*. Lab on a Chip, 2008. 8: p. 198 - 220.
188. Fair, R.B., *Digital microfluidics: Is a true lab-on-a-chip possible?* . Microfluidics and Nanofluidics, 2007. 3: p. 245-281.
189. Tan, M.K., Friend, J.R., and Yeo, L.Y., *Microparticle collection and concentration via a miniature surface acoustic wave device*. Lab on a Chip, 2007. 7: p. 618-625.
190. Joensson, H.N., Samuels, M.L., Brouzes, E.R., Medkova, M., Uhlen, M., Link, D.R., and Andersson-Svahn, H., *Detection and analysis of low-abundance cell-surface biomarkers using enzymatic amplification in microfluidic droplets*. Angewandte Chemie International Edition, 2009. 48: p. 2518-2521.
191. Hufnagel, H., Huebner, A., Guelch, C., Guese, K., Abell, C., and Hollfelder, F., *An integrated cell culture lab on a chip: Modular microdevices for cultivation of mammalian cells and delivery into microfluidic microdroplets*. Lab on a Chip, 2009. 9: p. 1576-1582.
192. Wang, W., Yang, C., and Li, C.M., *Efficient on-demand compound droplet formation: From microfluidics to microdroplets as miniaturized laboratories*. Small, 2009. 5: p. 1149-1152.
193. Huang, K.-S., Lu, K., Yeh, C.-S., Chung, S.-R., Lin, C.-H., Yang, C.-H., and Dong, Y.-S., *Microfluidic controlling monodisperse microdroplet for 5-fluorouracil loaded genipin-gelatin microcapsules*. Journal of Controlled Release, 2009. 137: p. 15-19.
194. Samuels, M.L., Leamon, J., Rothberg, J., Godiska, R., Schoenfeld, T., and Mead, D., *New paradigms in droplet-based microfluidics and DNA amplification*. Automation in Proteomics and Genomics 2009: p. 221-249.

195. Huebner, A., Srisa-Art, M., Holt, D., Abell, C., Hollfelder, F., de Mello, A.J., and Edel, J.B., *Quantitative detection of protein expression in single cells using droplet microfluidics*. Chemical Communications, 2007. 12: p. 1218-1220.
196. Srisa-Art, M., Dyson, E.C., de Mello, A.J., and Edel, J.B., *Monitoring of real-time streptavidin-biotin binding kinetics using droplet microfluidics*. Analytical Chemistry, 2008. 80: p. 7063-7067.
197. Yoon, J.-Y., *Detection of avian influenza type a H3N2 virus antigens in microchannel and droplet microfluidics*. Biological Engineering 2008. 1: p. 323-333.
198. Shah, G.J. and Kim, C.-J., *Fluidic conduits for highly efficient purification of target species in EWOD-driven droplet microfluidics*. Lab on a Chip, 2009. 9: p. 2402-2405.
199. Shah, G.J., Ohta, A.T., Chiou, E.P.-Y., Wu, M.C., and Kim, C.-J., *EWOD-driven droplet microfluidic device integrated with optoelectronic tweezers as an automated platform for cellular isolation and analysis*. Lab on a Chip, 2009. 9: p. 1732-1739.
200. Utada, A.S., Lorenceau, E., Link, D.R., Kaplan, P.D., Stone, H.A., and Weitz, D.A., *Monodisperse double emulsions generated from a microcapillary device*. Science, 2005. 308: p. 537 - 541.
201. Christopher, G.F. and Anna, S.L., *Microfluidic methods for generating continuous droplet streams*. Journal of Physics D: Applied Physics, 2007. 40: p. R319-R336.
202. Shiokawa, S. and Kondoh, J., *Surface acoustic wave sensor for liquid-phase application*. Proceedings of 1999 IEEE Ultrasonics Symposium, 1999. 1: p. 445-452.
203. Shiokawa, S., Matsui, Y., and Ueda, T., *Liquid streaming and droplet formation caused by leaky Rayleigh waves*. Proceedings of IEEE 1989 Ultrasonics Symposium 1989. 1: p. 643-646.
204. Bennès, J., Ballandras, S., and Chérioux, F., *Easy and versatile functionalization of Lithium Niobate wafers by hydrophobic trichlorosilanes*. Applied Surface Science, 2008. 255: p. 1796-1800.
205. Yeo, L.Y. and Friend, J.R., *Ultrafast microfluidics using surface acoustic waves*. Biomicrofluidics, 2009. 3: p. 012002/1-012002/23.

206. Luo, J.K., Fu, Y.Q., Le, H.R., Williams, J.A., Spearing, S.M., and Milne, W.I., *Diamond and diamond-like carbon MEMS*. Journal of Micromechanics and Microengineering 2007. 17: p. S147–S163
207. Huang, T.S., Tzeng, Y., Liu, Y.K., Chen, Y.C., Walker, K.R., Guntupalli, R., and Liu, C., *Immobilization of antibodies and bacterial binding on nanodiamond and carbon nanotubes for biosensor applications*. Diamond and Related Materials, 2004. 13: p. 1098-1102.
208. Matrab, T., Chehimi, M.M., Boudou, J.P., Benedic, F., Wang, J., Naguib, N.N., and Carlisle, J.A., *Surface functionalization of ultrananocrystalline diamond using atom transfer radical polymerization (ATRP) initiated by electro-grafted aryldiazonium*. Diamond and Related Materials, 2006. 15: p. 639-644.
209. Hartl, A., Schmich, E., Garrido, J.A., Hernando, J., Catharino, S.C.R., Walter, S., Feulner, P., Kromka, A., Steinmuller, D., and Stutzmann, M., *Protein-modified nanocrystalline diamond thin films for biosensor applications*. Nature Materials, 2004. 3: p. 735-742.
210. Hartl, A., S. Nowy, J. Hernando, J.A. Garrido, and M. Stutzmann, *Bio-interfacing of diamond films for sensor applications*. 2005 IEEE Sensors, 2005: p. 496-499.
211. Siew, P.S., Loh, K.P., Poh, W.C., and Zhang, H., *Biosensing properties of nanocrystalline diamond electrodes*. Diamond and Related Materials, 2005. 14: p. 426-431.
212. Birrell, J., Gerbi, J.E., Auciello, O., and Gibson, J.M., *Bonding structure in nitrogen doped ultrananocrystalline diamond*. Journal of Applied Physics, 2003. 93: p. 5606-5612.
213. Bia, B., Huang, W.-S., Asmussen, J., and Golding, B., *Surface acoustic waves on nanocrystalline diamond*. Diamond and Related Materials, 2002. 11: p. 677–680.
214. Hakikia, M.E., Elmazriaa, O., Bénédict, F., Nicolaya, P., Monégerb, D., and Azouanib, R., *Diamond film on Langasite substrate for surface acoustic wave devices operating in high frequency and high temperature*. Diamond and Related Materials, 2007. 16: p. 966-969

About the Author

Reetu Singh was born in Kanpur, India. She obtained her Bachelor's degree in Chemical and Bio Engineering in 1999 from National Institute of Technology, Jalandhar, India where she was awarded the gold medal for excellence in the college of Engineering. She worked as a Senior Process Engineer at Whirlpool of India Ltd, Pune, India from 1999-2000. She was awarded a Master's degree in Chemical Engineering in 2002 from the prestigious Indian Institute of Science, Bangalore, India where she worked on the modeling of nanoparticle formation via the liquid-liquid dispersion route. She began pursuing doctoral degree in Chemical and Biomedical Engineering at the University of South Florida (USF) in Summer 2004. During the course of her study at USF, she presented her research at many international conferences and published several papers.